

AN INVESTIGATION OF SYSTEM IDENTIFICATION AND DAMAGE
ESTIMATION USING MODAL PLOTS, COUNT PLOTS AND A
DAMAGE INDICATOR

by

Tarık TUFAN

B.S., Civil Engineering, Boğaziçi University, 2005

M.S., Civil Engineering, Boğaziçi University, 2008

Submitted to the Institute for Graduate Studies in
Science and Engineering in partial fulfillment of
the requirements for the degree of
Doctor of Philosophy

Graduate Program in Civil Engineering
Boğaziçi University

2019

ACKNOWLEDGEMENTS

Praise my Lord!

I am approaching the end of a challenging marathon and to the beginning of the many others. I hope to be able to meet them as an engineer and overcome them with the attitude of an academician. In this thesis, I did not leave the truth and honesty.

I am grateful to Prof. Hilmi Luş, who provided all kinds of support during my studies and who took advantage of his vast experience and comments, who explained the free vibration solution, provided the O3KID code I used in my studies and made corrections by reviewing my articles.

I would like to thank Assoc. Prof. Fuat ARAS, who has supported me in my studies, who has participated in my progress and thesis juries, and shared me data of 116M254 coded TÜBİTAK project which is entitled as "Investigation of the effects of structural damages on structural dynamic properties of reinforced concrete structures and vibration analysis and damage determination".

I would like to thank Prof. Cem YALÇIN, Assoc. Prof. Serdar SOYÖZ and Assoc. Prof. Ufuk YAZGAN, who share their vast experience and comments.

I also owe thanks to my colleague Fatih COŞKUN, Selim PARLAKYİĞİT, Mustafa COŞKUN, Selahattin AKALP, Oğuz ŞENKARDEŞLER and other friends in Medeniyet and Boğaziçi University who have always been helping me during my doctoral studies. I hope each of you will be as successful as Prof. Aziz SANCAR.

I would like to thank my parents for their support and encouragement throughout my life.

And my dear wife Zeynep, my daughters Ayşe Sena & Hümeysra and my son Yahya... I attribute this work to you. So glad you exist.

ABSTRACT

AN INVESTIGATION OF SYSTEM IDENTIFICATION AND DAMAGE ESTIMATION USING MODAL PLOTS, COUNT PLOTS AND A DAMAGE INDICATOR

Structural Health Monitoring (SHM) aims to detect slow and/or sudden changes in a structure, and the possible damage associated with such changes, using system identification and damage detection methodologies. It eventually also aims to provide an estimate for the remaining useful life of a structure and to provide guidance to structural design.

In this thesis, new approaches are presented for system identification, damage detection and sensor deployment under operational loads. In the introduction chapter, the importance of the subject, four crucial questions for SHM system design, and a short literature review are discussed.

In the second chapter of the thesis, a sensitivity based damage detection algorithm is developed. The performance of the proposed system identification and damage detection methods are investigated numerically. The numerical demonstration of the proposed damage detection method is investigated for the full measurement and restricted measurement cases at the end of the chapter. The proposed method is tested on a numerical six-story structure model for damage at one story and multiple story scenarios in the fifth chapter.

In the third chapter which deals with system identification, a new interpretation and a new algorithm called the ‘modal plot’ are provided for ‘stabilization diagrams’; it is shown that, it is possible to automatically identify the natural frequencies and the mode shapes of a system by converting its modal plot to a ‘count plot’. The count plot approach could be viewed as an alternative to power spectrum analysis. A case study is given at the end of the chapter and the proposed method is used to investigate natural frequency changes due to damage for data taken from a real structure in Chapter 6.

Chapter 4 presents detailed discussions on the performance of the proposed methods via three numerical examples, which show that using the proposed methodology, it is possible to detect damage using the first three modes. In the experimental study, it is proposed that modal zones are sensitive to presence of the damage and the damage indicator is used to estimate the damage location.

In the concluding chapter, a general discussion of the methods proposed in this thesis is provided.

ÖZET

MOD PLANI, SAYIM PLANI VE HASAR BELİRTECİ KULLANILARAK SİSTEM TANILAMA VE HASAR TAHMİNİ ÜZERİNE BİR İNCELEME

Yapı Sağlığı İzleme Sistemleri (YSİ), sistem tanılama ve hasar tespit yöntemleri ile yapıda yavaş yavaş ya da aniden oluşabilecek değişiklikleri ve bu değişikliklerle ilintisi muhtemel hasarı belirlemeyi amaçlar. İleri hedefleri ise yapının kalan ömrünü tahmin etmek ve yapı tasarımına yön vermektir.

Bu tezde, işletim yükleri altında sistem tanılama, hasar tespiti ve sensör konumlandırma için yeni yöntemler aktarılmaktadır. Giriş bölümünde, konunun önemi, YSİ sistem tasarımı için dört önemli soru ve kısa bir yazın taraması tartışılmaktadır.

Çalışmanın ikinci bölümü olan hasar tespit kısmında ise hassaslık temelli bir yöntem geliştirilmiştir. Önerilen parametre ve yöntemin performansı sayısal olarak incelenmiş, bölümün sonundaki sayısal örneklerde tam ölçüm ve kısıtlı ölçüm durumları ele alınmıştır. Önerilen yöntem, beşinci bölümde altı katlı bir yapı modelinde bir kat hasar ve çok kat hasar senaryoları için test edilmiştir.

Tezin üçüncü bölümü olan sistem tanılama kısmında, ‘kararlılık şeması’ olarak adlandırılan yaklaşım ‘mod planı’ olarak isimlendirilen yeni bir yorum ve algoritma ile ele alınmıştır. Mod planları, ‘sayım planlarına’ dönüştürülerek sistemin özfrekanslarını ve mod şekillerini otomatik olarak belirlemekte kullanılmıştır. Sayım planı yaklaşımı güç tayf yoğunluğu yöntemine alternatif bir yöntem olarak düşünülebilir. Bölüm sonunda bir vaka çalışması verilmiş ve önerilen yöntem Bölüm 6’da gerçek bir yapıdan alınan ölçümler için hasar nedeniyle doğal frekans değişimlerini araştırmak için kullanılmıştır.

Vaka analiz çalışmasında (Bölüm 4), üç sayısal örnek tartışılmış ve önerilen yöntem ile ilk üç mod kullanılarak ve sistemin iki durumu değerlendirilerek hasar konumunun tespit edilebileceği gösterilmiştir. Deneysel çalışmalarda ise modal bölgelerin hasarın varlığına hassas olduğu gösterilmiş ve hasar belirteci ile hasarın konumu tespit edilmiştir.

Kapanış bölümünde ise, tezde önerilen yöntemlerin genel değerlendirmesi verilmiştir.

TABLE OF CONTENTS

ACKNOWLEDGEMENTS	iii
ABSTRACT	iv
ÖZET	vi
TABLE OF CONTENTS	viii
LIST OF FIGURES	xi
LIST OF TABLES	xx
LIST OF SYMBOLS	xxii
LIST OF ABBREVIATIONS	xxiii
1. INTRODUCTION	1
1.1. Modal Analysis	5
1.2. Methods from Different Disciplines	7
1.3. SHM in Bridge Monitoring	9
1.4. Thesis Outline and Main Contributions	16
2. DAMAGE DETECTION	19
2.1. Classification of Damage:	19
2.2. Determination of Damage Sensitive Parameters	20
2.3. Sensitivity Based Damage Identification Methods	20

2.4.	Method Proposal	24
2.4.1.	Initial Enhancements	24
2.4.2.	Comparison of the Initial Proposal with Yuen's Proposal.	25
2.4.3.	Further Enhancements	29
2.5.	Case Studies	32
2.5.1.	A Numerical Demonstration of the Proposed Fault Identification Method	32
2.5.2.	A Numerical Demonstration of the Proposed Fault Identification Method under Limited Measurement Locations	35
3.	SYSTEM IDENTIFICATION	38
3.1.	Stabilization Diagrams	39
3.2.	The Modal Plot	41
3.3.	The Count Plot.	46
3.4.	A Case Study.	47
3.5.	Effect of Damping Ratio on Modal Plot and Count Plot	58
4.	NUMERICAL AND EXPERIMENTAL CASE STUDIES	64
4.1.	Fault Identification with Noise-Free Ambient Vibration Data:.	64
4.2.	Fault Identification for Noise-Free Data with Limited Measurement Locations	68
4.3.	Fault Identification for Noisy Data	70

4.4. Level 0 Damage Detection on a Beam with Hinges Using Modal Zones .	80
4.5. Level 1 Damage Identification of a Beam with Hinges Using the Damage Indicator	88
5. APPLICABILITY OF THE PROPOSED DAMAGE INDICATOR TO BUILDINGS	93
5.1. The Model Building and Damage Scenarios Considered.	93
5.2. Results Obtained via the Single Mode Damage Indicator with the First Mode	98
5.3. Results Obtained via the Single Mode Damage Indicator with the Second and Third Modes	109
5.4. Results Obtained via the Multi-Mode Damage Indicator with the First Three Modes	114
6. ESTIMATION OF MODAL PARAMETERS FROM REAL DATA	117
7. CONCLUSIONS	124
REFERENCES	126

LIST OF FIGURES

Figure 1.1.	SHM utilization for maintenance activities as presented by Alampalli et al. (2005).	11
Figure 2.1.	Cantilever model (a) finite element model with element and node numbers. (b) cross-section of the beam (all dimensions in mm).	25
Figure 2.2.	Yuen's (1985) damage indicators for damage located on element 10.	26
Figure 2.3.	Proposed damage Indicators for damage located on element 10.	27
Figure 2.4.	Proposed translational damage indicator for different damage locations.	27
Figure 2.5.	Proposed rotational damage indicator for different damage locations.	28
Figure 2.6.	Proposed translational damage indicator for varying degrees of damage on element 5	28
Figure 2.7.	Proposed rotational damage indicator for varying levels of damage on element 5	29
Figure 2.8.	100 DOF spring – mass chain systems: (a) the 'cantilever' system, (b) the 'simply supported' system.	32
Figure 2.9.	Damage Indicator values calculated via the first mode and the first three modes in the case of a 5% stiffness reduction in the 1st, 30th, 51th and 90th springs.	33

Figure 2.10.	A summary representation of the largest and smallest values that the damage indicator takes at the undamaged positions for the cantilever system (for a 5% reduction in spring stiffness).	34
Figure 2.11.	A summary representation of the largest and smallest values of the damage indicator in undamaged positions for a simply supported chain system (for a 5% reduction in spring stiffness)..	35
Figure 2.12.	Summary view of the first mode and the first three modes undamaged indicator.	36
Figure 2.13.	Damage Indicator for the first mode and for the sum of first three modes (Few Measurements and Multiple Damage Location)	37
Figure 3.1.	A representative PSD and stabilization diagram as given by (De Roeck et al., 2000)	40
Figure 3.2.	A representative modal plot	46
Figure 3.3.	The mass-spring ‘cantilever’ system used	48
Figure 3.4.	Power spectral density estimate of the ambient input applied on the 15th DOF.	48
Figure 3.5.	Power spectral density estimates for the 1st, 5th, 9th, and 13th DOFs	49
Figure 3.6.	Modal plots for various DOFs, including actual modal points (circles) and modal zones.	50
Figure 3.7.	Modal plot tolerance limits.	51
Figure 3.8.	Count plot for 0.1% tolerance limit.	51
Figure 3.9.	Accumulation of estimates in Modal Parameters for DOF 4.	52

Figure 3.10.	The first 4 mode shapes: Lines: exact mode shapes calculated via the eigenvalue problem; markers: estimated values using the count plot.	53
Figure 3.11.	Modal plot: 1% tolerance limit.	53
Figure 3.12.	Count Plot for different tolerance limits for 1st DOF.. . . .	54
Figure 3.13.	Count Plot for different tolerance limits for 4th DOF.	55
Figure 3.14.	Count Plot for different tolerance limits for 7th DOF.	55
Figure 3.15.	Count Plot for different tolerance limits for 14th DOF.	56
Figure 3.16.	Error limits in modal parameters for tolerance limit 0.001.	56
Figure 3.17.	Error limits in modal parameters for tolerance limit 0.01.	57
Figure 3.18.	Error limits in modal parameters for tolerance limit 0.05.	57
Figure 3.19.	Histogram using frequency estimates and its comparison with the count plot.	58
Figure 3.20.	Change in a modal plot for increasing damping for the 1 st DOF.	58
Figure 3.21.	Mode shape estimates for the tolerance limit 0.004 and 0.01 for CDR 0.2%	60
Figure 3.22.	Mode shape estimates for the tolerance limit 0.004 and 0.01 for CDR 1%	61
Figure 3.23.	Mode shape estimates identified for the system with CDR 5% using threshold phase angle values of $\pi/4$ and $\pi/10$	62
Figure 3.24.	Mode shape estimates identified for the system with CDR 10% using threshold phase angle values of $\pi/4$ and $\pi/10$	62

Figure 3.25.	Mode shape estimates identified for the system with CDR 5% using higher model orders and threshold phase angle values of $\pi/4$ and $\pi/10$	63
Figure 3.26.	Mode shape estimates identified for the system with CDR 10% using higher model orders and threshold phase angle values of $\pi/4$ and $\pi/10$	63
Figure 4.1.	PSD estimates for the three data sets obtained from acceleration data ‘measured’ at the first DOF.	65
Figure 4.2.	Count Plots for the 4th and the 7th DOFs for the three data sets.	67
Figure 4.3.	Damage indicator values for Damage Cases 1 and 2 for the 10 DOF system.	68
Figure 4.4.	100 DOF damped ‘cantilever’ system.	69
Figure 4.5.	Damage indicator values for Damage Cases 1 and 2 for the 100 DOF system with limited measurements.	70
Figure 4.6.	PSD estimates obtained using the noisy acceleration data measured from the 1st DOF for the damage cases considered (0-8 Hz).	71
Figure 4.7.	PSD estimates obtained using noisy and noise free data measured from the 1st DOF for the undamaged system (0-8 Hz)	72
Figure 4.8.	Count plots for the 4th and the 7th DOFs for the three cases.	74
Figure 4.9.	Effects of noise on mode shapes	74
Figure 4.10.	Single mode damage indicator calculated using the 1st mode: (a) comparing Damage Case 1 with the Undamaged Case, (b) comparing Damage Case 2 with the Undamaged Case.	75

Figure 4.11.	Single mode damage indicator calculated using the 2nd mode: (a) comparing Damage Case 1 with the Undamaged Case, (b) comparing Damage Case 2 with the Undamaged Case.	75
Figure 4.12.	Single mode damage indicator calculated using the 3rd mode: (a) comparing Damage Case 1 with the Undamaged Case, (b) comparing Damage Case 2 with the Undamaged Case.	76
Figure 4.13.	Deployment of sensors for the cantilever and simply supported system	78
Figure 4.14.	Schematic representation of the steel beam showing segment numbers and the locations of the accelerometers.	81
Figure 4.15.	Experimental setup and the black box marks the damage position . . .	82
Figure 4.16.	Accelerometer orientation	82
Figure 4.17.	Modal plots for the undamaged and the damaged steel beam (accelerometers on the 7th and the 8th segments)	84
Figure 4.18.	Count plots for the experimental beam (tolerance limit 0.004).	84
Figure 4.19.	Modal plots for damaged and undamaged systems (accelerometers on 6th and 8th segments).	85
Figure 4.20.	Modal plots for damaged and undamaged systems (accelerometers on 5th and 8th segments).	86
Figure 4.21.	Modal plots for damaged and undamaged systems (accelerometers on 4th and 8th segments).	86
Figure 4.22.	Modal plots for damaged and undamaged systems (accelerometers on 3rd and 8th segments).	87

Figure 4.23.	Modal plots for damaged and undamaged systems (accelerometers on 2nd and 8th segments)	87
Figure 4.24.	Modal plots for damaged and undamaged systems (accelerometers on 1st and 8th segments)	88
Figure 4.25.	Unscaled Damage Indicator using Equation 2.15.	90
Figure 4.26.	Scaled Damage Indicator using Equation 2.17	90
Figure 4.27.	Mode Shape for two states of the system	92
Figure 4.28.	Location of damage using Translational Damage Indicator for the experimental study.	92
Figure 5.1.	Typical floor plan.	94
Figure 5.2.	Elevation of the six story building.	94
Figure 5.3.	Single Column Damaged on the first story.	98
Figure 5.4.	Single column damaged on the second story.	99
Figure 5.5.	Single column damaged on the third story.	100
Figure 5.6.	Single column damaged on the fourth story.	100
Figure 5.7.	Single column damaged on the fifth story.	101
Figure 5.8.	Single column damaged on the sixth story	101
Figure 5.9.	Nine columns damaged on the first story	102
Figure 5.10.	Nine columns damaged on the second story	103
Figure 5.11.	Nine columns damaged on the third story.	103

Figure 5.12.	Nine columns damaged on the fourth story.	104
Figure 5.13.	Nine columns damaged on the fifth story	104
Figure 5.14.	Nine columns damaged on the sixth story	105
Figure 5.15.	All columns severely damaged on a single floor.. . . .	106
Figure 5.16.	All columns mildly damaged on a single floor.	106
Figure 5.17.	All columns severely damaged on two different stories.. . . .	107
Figure 5.18.	All columns severely damaged on two or three different stories.	107
Figure 5.19.	All columns severely damaged on three or four different stories.. . . .	108
Figure 5.20.	All columns severely damaged on four or five different stories.. . . .	108
Figure 5.21.	All columns severely damaged on five or six different stories.	109
Figure 5.22.	Damage detection for scenarios in which a single column is damaged on a single floor via the single mode damage indicator using the second mode.	110
Figure 5.23.	Damage detection for scenarios in which nine columns are damaged on a single floor via the single mode damage indicator using the second mode.. . . .	110
Figure 5.24.	Damage detection for scenarios in which all columns are damaged on a single floor via the single mode damage indicator using the second mode.. . . .	111
Figure 5.25.	Damage detection for scenarios in which a single column is damaged on a single floor via the single mode damage indicator using the third mode.	111

Figure 5.26.	Damage detection for scenarios in which nine columns are damaged on a single floor via the single mode damage indicator using the third mode.	112
Figure 5.27.	Damage detection for scenarios in which all columns are damaged on a single floor via the single mode damage indicator using the third mode.	113
Figure 5.28.	Damage detection for scenarios in which all columns are damaged on a single floor via the single mode damage indicator using the second and the third modes.	113
Figure 5.29.	Damage detection for scenarios in which a single column is damaged on a single floor via the multi-mode damage indicator using the first three modes.	114
Figure 5.30.	Damage detection for scenarios in which nine columns are damaged on a single floor via the multi-mode damage indicator using the first three modes.	115
Figure 5.31.	Damage detection for scenarios in which all columns are damaged on a single floor via the multi-mode damage indicator using the first three modes.	115
Figure 5.32.	Damage detection for scenarios in which all columns are damaged on mutiple floors via the multi-mode damage indicator using the first three modes.	116
Figure 6.1.	The reinforced concrete building investigated and the structural elements removed to induce damage.	118
Figure 6.2.	Accelerometer locations on a floor, plan view.	118

Figure 6.3.	PSD estimates for the eight data sets obtained from acceleration data measured during the Undamaged State..	120
Figure 6.4.	PSD estimates for the eight data sets obtained from acceleration data measured during the Damaged State.	120
Figure 6.5.	Count plot estimates for the eight data sets obtained from acceleration data measured during the Undamaged State using a tolerance limit of ± 0.01	121
Figure 6.6.	Count plot estimates for the eight data sets obtained from acceleration data measured during the Undamaged State using a tolerance limit of ± 0.004	121
Figure 6.7.	Count plot estimates for the eight data sets obtained from acceleration data measured during the Damaged State using a tolerance limit of ± 0.01	122
Figure 6.8.	Count plot estimates for the eight data sets obtained from acceleration data measured during the Damaged State using a tolerance limit of ± 0.004	122

LIST OF TABLES

Table 3.1.	Numerical Analysis Specifications	48
Table 4.1.	Estimated frequency ranges for the first three modes:	66
Table 4.2.	The natural frequencies determined by O3KID / ERA and the count plots.	66
Table 4.3.	The mode shapes determined by O3KID / ERA and the count plots . .	66
Table 4.4.	Natural-frequencies determined by O3KID / ERA and count plot . . .	69
Table 4.5.	Mode shapes determined by O3KID / ERA and count plots	69
Table 4.6.	Natural frequencies determined by O3KID / ERA and count plots . . .	72
Table 4.7.	Mode Shapes determined by O3KID / ERA and count plots for the Undamaged Case	72
Table 4.8.	Mode Shapes determined by O3KID / ERA and count plots for the Damaged Case 1	73
Table 4.9.	Mode Shapes determined by O3KID / ERA and count plots for the Damaged Case 2	73
Table 4.10.	Numbers of the springs overlapping with the saddle points of the first three modes of the 10 DOF system	77
Table 4.11.	Relative Stiffness Matrix for Damage Case 1 as percentage	80
Table 4.12.	Relative Stiffness Matrix for Damage Case 2 as percentage	80
Table 4.13.	Norms of signals measured by the reference.	83

Table 4.14.	Estimated Modal Parameters for the first mode	91
Table 5.1.	Damage scenarios for Category I (single column damage on a single story).	96
Table 5.2.	Damage scenarios for Category II (nine neighboring columns damaged on a single story).	96
Table 5.3.	Damage scenarios for Category III (all columns damaged on a single story).	96
Table 5-4	Damage scenarios for Category VI (all columns damaged on a multiple stories).	97
Table 6.1.	Estimated natural frequency for the first mode:	123
Table 6.2.	Estimated natural frequency for the second mode:	123
Table 6.3.	Estimated natural frequency for the third mode:	123

LIST OF SYMBOLS

Φ	Translational modeshape
θ	Rotational modeshape
Δ	Difference operator
A	State transition matrix of the first order model
C	Output matrix of the first order model
K	Observer gain
\mathcal{H}	Hankel Matrix
\mathbb{O}	Observability Matrix
\mathbb{C}	Controllability Matrix
$\hat{\Gamma}$	Markov parameters in the bar form
Ψ	Markov parameters
ε	Output residuals of the Kalman Filter
S	Singular values
U	The left singular vector
V	The right singular vector
n	System Order
q	Number of Channel
p	Model Order
v, w	White noise sequences
x	State vector
y	Measurement vector

LIST OF ABBREVIATIONS

ANN	Artificial Neural Network
DOF	Degrees of Freedom
ERA	Eigensystem Realization Algorithm
FCM	Fuzzy C-Means
FFT	Fast Fourier Transform
FRF	Frequency Response Function
LAE	Large Area Electronics
MAC	Modal Assurance Criteria
O3KID	Output Only Observer Kalman Filter Identification
OKID	Observer Kalman Filter Identification
OMA	Operational Modal Analysis
PSD	Power Spectral Density
SHM	Structural Health Monitoring
SSI	Stochastic Subspace Identification

1. INTRODUCTION

There is no unique definition, but depending on the user and the aim in monitoring, structural health monitoring (SHM) can be defined by employing various perspectives: From the perspective of damage detection, SHM is one of the important tools for engineers dealing with mechanics in monitoring the *existence, location, and type* of the *extending* defects in order to take proper precautions *before* the growths in defects reach one or more of the following critical levels: (i) disturbing the operational state of a structure, (ii) disrupting the “health” of a structure, (iii) endangering the surrounding living and nonliving environment. The critical levels are strictly different for target performance levels in the design as well as for the type of structure such as nuclear plants, aircraft, bridges, dams.

From the perspective of the design of materials and structures, SHM is a tool for designers (i) to understand the behavior, type and frequency of forces acting on existing structures as well as the response of the material and the structure to these acting forces, (ii) to design a future structure depending on the frequency content of the forces acting on the construction site (as there can be certain dominant frequency ranges identified in long-term collected data from winds, water or underground actions) so that vibration modes of the structure do not coincide with the dominant frequencies of the input forces, (iii) to reduce the factors of safety in design and possibly decrease the amount of material (Derriso et al., 2009) required in a similar future structure (lighter design), (iv) to compare the results of numerical models, the experimental results obtained from scaled models and the measurements from the real structure, (v) to improve available modeling techniques (vi) to develop smart materials based on frequency content of the design.

By considering these two perspectives together, it can be said that SHM eventually aims to ensure that necessary measures are taken in a timely manner against events threatening the structure and to provide guidance to structural design. According to researches, many bridges in the US have completed their useful life (Aktan et al., 1996), and Japan will face the same situation in a few years (Fujino et al., 2013). In addition, wear and

damage caused by unpredictable rare events such as severe earthquakes, severe winds, and floods will reduce the useful life of buildings (Shepherd et al., 1995). Therefore, it would be an important precaution to monitor and control important structures with SHM systems. In many countries such as Japan (Sumitro et al., 2005) and Australia (Chan et al., 2011) SHM systems are widely used in critical structures and the necessary software and hardware components are developed by these countries. This issue is taken into consideration and its popularity is increasing day by day also in Istanbul (Soyoz et al., 2017; Çaktı et al., 2019) and in the world (Chen et al., 2017; Li et al., 2015; Abe et al., 2017; Hester et al., 2017; Compán et al., 2017; Lorenzo et al., 2015; Juul et al., 2019; Kirschneck et al., 2015; Nord et al., 2017)

Along with critical and special structures, it is also possible to use SHM systems in ordinary structures (Satake et al., 2003) for control purposes. In the design process, calculations are made according to the theoretical period of the structure. Although it is possible to make these computations precisely, differences between the measured vibration periods of the building and the calculated periods of the numerical model are common within certain limits. This difference may mean that the calculations are conservative, thereby remaining on the safe (non-conservative) side, meaning a possible increased level of risk. After a building is constructed, dynamic investigations with small-scale SHM systems may give an effective opportunity to identify significant differences and to assess the safety of the building (Astroza et al., 2016).

One of the successful examples for the utilization of SHM in control is the work done by Sumitro et al. (2001). This study compares the results of numerical data, which is related to design codes, with experimental data related to the wind tunnel tests and also with real data measured on the Akashi Kaikyo Bridge during a typhoon event. In comparison, the girder displacements are used. It is found that transversal displacements in the typhoon event have good agreement with guidelines. Moreover, the guidelines and wind tunnel test results are on the safe side for the vibration amplitudes.

In SHM systems, different types of sensors are utilized: accelerometers, strain gauges, load transducers, and GPS based displacement measurement systems are some of the

frequently used devices (technical details of sensors and their uses are described in (Meehan, 2011)). The effects of the location and the sampling frequency of sensors on the measurements are investigated by Grimmelsman et al. (2007) wherein the authors report the results of ambient vibration tests conducted over a period of one month on a long-span steel arch bridge to observe uncertainties in the measurements. The consistency of the identified parameters is examined through statistical analyses, and the effects of bandwidth and stationarity on the identified parameters are discussed. The results indicate that unavoidable electric and environmental noise produce spurious spikes in measurements. Selection of sensor locations, sampling frequency, and data duration may cause spatial and frequency aliasing. Uncertainties in stationarity of the measurement data and variability due to traffic flow and changes in ambient temperature do not affect the identified natural frequencies significantly. Sampling with a rate more than that which covers the target frequency range has no pronounced effect on the identified frequencies. The authors suggest selecting a sampling rate depending on the frequency range of concern, the amount of stored data, and the time required for the analyses.

The SHM systems are desired to be able to eliminate the effects of environmental factors on their components (software and hardware) because environmental factors affecting the structural response constantly change during the operation. The changes in the ambient temperature, air pressure, and humidity can alter material properties; hence, the system properties are likely to change. In most cases, the source of the change in the structural response related to environmental effects is not directly associated with structural health, but generally these effects can't be differentiated and the structural changes tend to be attributed to structural damage. The three studies briefly mentioned in the following paragraphs show that changes induced on the natural frequencies by operational conditions may surpass those caused by serious levels damage.

Jiménez-Roa et al. (2016) observe that environmental conditions conceal the effect of earthquake damage on natural frequencies. They use the Natural Excitation Technique (NExT) with the Eigensystem Realization Algorithm (ERA) and the Stochastic Subspace Identification (SSI) methods in order to estimate the modal parameters of Building 350 at Del Valle University under ambient vibrations and under six critical events. For the effects

of earthquake damages on natural frequencies, they conclude that the existence of damage cannot be detected by investigating only the changes in the natural frequencies since such changes would lay in the expected range of variations in operational and environmental conditions.

Toksoy et al. (1994) formulate a modal flexibility based condition index for a three-span reinforced-concrete highway bridge. Polyreference frequency and time domain parameter estimation methods are used in the analysis of forced vibration test data. The bridge is tested in its undamaged condition and also after shear failure of one of its spans under high loads, and a 1.44% drop in the first natural frequency is identified, with almost no discernable changes in the mode-shapes. Aktan et al. (1997) also investigate the same structure using forced and impact vibration tests. They report that microstrain responses due to temperature variations in long term monitoring are higher than the bridge microstrain responses due to overloaded truck traffic.

Because the effects of operational and environmental conditions on natural frequency changes are not negligible, researchers have developed methods of normalizing the signals in order to detect the existence of damage.

In this context Magalhães et al. (2012) develop a method detecting damage from changes in natural frequencies. They used two-year monitoring data obtained on the Infante D. Henrique bridge data to identify its natural frequencies while they aim to minimize the effects of environmental and operational factors on natural frequency shifts. Static and dynamic regression models are developed and dynamic regression models are found to fit the operational conditions successfully. Furthermore, PCA analysis is used to improve the regression models. Control charts using the outputs of the PCA are constructed, and it is shown that resultant control charts are effective indicators in detecting very small natural frequency changes due to damage.

Langone et al. (2017) propose a process that unifies data normalization and damage detection steps using the proposed algorithm called adaptive kernel spectral clustering (AKSC) algorithm. With user intervention in model selection, the algorithm is calibrated in the undamaged state of the structure in order to detect early damages and to minimize the

number of false alarms. The method merges clusters or defines new clusters according to changes in the data. Two damage sensitive features are introduced (kernel bandwidth, the number of clusters) in order to detect critical changes in the data. The method is tested with simulated data and real data from the Z24 concrete bridge.

In fact, environmental conditions may change the capacity of the structure (i.e. change in modulus of elasticity of the material due to temperature change, corrosion of steel rebar due to permeation of chloride), and therefore the normalization process should also take into account possible changes in the capacity of the structure due to variations in environmental conditions. In this thesis, a unique identifier for the damage existence problem is proposed, which is dependent on both frequency and mode shape estimates, as well as an enhanced indicator to locate damage in discrete and continuous systems. Data normalization for environmental changes are not considered. One of the properties of the damage sensitive parameter proposed in Chapter 2 (modal zone) and Chapter 3 (damage indicator for the damage location) is its sensitivity to changes in the capacity of the system, which is dependent on material and the geometry of the structure, and non-sensitive to changes in demand, which is reflected in the response and depends on the amplitude of the input forces. Some of the sensitivity based studies previously published are introduced in Chapter 2.

1.1. Modal Analysis

In theory, modal analysis is a process used in defining the inherent dynamic characteristics of an object, depending on its material and geometry, in terms of its resonant frequencies, mode shapes, damping factors and modal scaling factors without the need of a disturbing force. The modal data are used to construct a (mathematical) modal model of the object with the aim of replicating its observed dynamic behavior (Fu et al., 2001). In practice, for a real structure, observing and/or identifying its modes require that those modes should be activated by ‘forces’. Depending on the type of the inputs, modal analysis is generally classified under three main headings: experimental, operational and combined modal analysis.

Experimental modal analysis (EMA) is a conventional tool for SHM which requires vibration tests using controlled excitations (known input forces) (Tcherniak et al., 2012). The methods used in EMA require measurements of both input forces and responses. Under rare events such as earthquakes and strong winds, EMA methods are appropriate if the input forces are measured properly. Although it is theoretically possible to apply prescribed forces to any structure, the size of the required actuators and the social and/or economic costs due to closures for the testing make EMA methods inefficient for large scale civil engineering structures. Moreover, in practice, there are certain challenges such as the limited amount of response measurement stations and difficulties in measuring the external forces during operational conditions. Vibration-based system identification studies often rely on the white noise assumption where the operational external forces are modeled as a noise exciting ‘uniformly’ all the frequency components (Yang, 1975, Peeters, 2000, Ren et al., 2004). The white noise assumption facilitates identifying the parameters related to the dynamic behavior of the structure under daily (operational) loads. In the literature, such approaches which are based only on the system response are called Operational (or Output only) Modal Analysis (OMA) (Peeters et al., 2001a). Today, some of the EMA methods are converted to OMA counterparts (see one of the examples in Chapter 2.2). OMA methods suit well to civil engineering structures, although there are problems related to scaling in the mode shape estimation and narrow-banded frequency content of the input forces (Reynders, 2009). To address these problems, researchers have developed methods based on the combined experimental and operational modal analysis called Operational Modal Analysis with eXogenous inputs (OMAX) (Reynders et al., 2010; Cauberghe et al., 2003).

In this thesis, a well-known OMA method is used to estimate the modal parameters to be used in the damage existence problem (see Chapter 2). Moreover, a unique damage indicator is used to locate the damage (see Chapter 3). While alternative methods are not considered in detail in this thesis, studies using methods from other disciplines for damage detection and data normalization are briefly mentioned in Section 1.2. Moreover, in Section 1.3, some articles related to bridge monitoring are also included in the literature review. These two sections are not the main focus of this thesis, yet due to their significance in SHM, they are included.

1.2. Methods from Different Disciplines

The term “*discipline*” is defined as a specific body of teachable knowledge with its own background of education, training, procedures, methods and content areas (Gozzer, 1982). Not so long ago, engineering disciplines were classified into four primary branches: Civil, Mechanical, Electrical, and Chemical Engineering. Recently, the number of disciplines increased to as much as forty (Steinmann et al., 2014). As the knowledge in the disciplines grows, new clusters (disciplines) may be born or a mature discipline may branch into two ‘separate’ disciplines. As interdisciplinary studies provide different points of view, they may also lead to the birth of new disciplines.

SHM has started to slowly separate from the dynamics multi-discipline and become a new engineering discipline. Researchers have started to use learning algorithms such as artificial neural networks (ANN) and deep learning since 1992 and 2014 respectively. A drawback of these studies is that they are not appropriate for generic structures but rather they have to be tailored for a specific model or a structure. Critical infrastructure systems such as bridges and power plants may require significantly more care and for such structures more detailed model based methods may be required (Karbhari et al., 2009). There is also need to detect biological and chemical loads (Alampalli et al., 2005) in order to take proper precautions, for example, biosensors might be used to control the humidity level and to avoid insects (Creffield, 1996) and plants harming the structure. There is no study in the literature related to the utilization of biosensors in SHM and clearly an interdisciplinary teamwork is needed to accomplish this task. As this example demonstrates, SHM has become a significantly interdisciplinary subject and the following literature review aims to reflect this important feature. An important issue, as previously mentioned, is fitting a distribution to natural frequencies dependent on environmental factors such as ambient temperature, and recent studies draw heavily from the fuzzy clustering research which is one of the widely used methods for *image segmentation* in image processing and in noise removal. Some examples for this approach are provided below.

Chandrashekhar et al. (2009) use fuzzy clustering analysis for damage detection. They present a fuzzy logic system with a sliding window technique. Modal curvature vectors are

used for damage identification purposes. It is observed that the sliding window technique increases the success rate in damage detection and the fuzzy clustering may compensate for missing measurements. The proposed method is tested on a numeric cantilever beam and found to be capable of detecting small amounts of damage in the tip of the beam.

Lam et al. (2006) combine changes in Ritz vectors (i.e. due to damage) and the Bayesian ANN design method in order to detect the location and the extension of damage in the system. The method is applied to a numeric truss model and the results show that Ritz vectors are sensitive to damage and not sensitive to noise in the response or the modeling errors.

Abdeljaber et al. (2017) propose a method which is capable of automatically extracting optimal damage-sensitive features and of detecting damage from raw acceleration signals. The method uses adaptive implementation of 1D Convolutional Neural Networks for each measurement point. The results of both small and large-scale experiments demonstrate the superior ability of their approach to learn the extraction of optimal features.

Feng et al. (2017) compare conventional acceleration based methods with vision based displacement measurements which yield lower costs and are non-contact tools. For a simply supported beam structure it is shown that one camera is adequate to measure and calculate smoother mode shapes and to estimate the natural frequencies accurately. Moreover, one of the challenges related to physical dimensioning in vision-based measurements is the estimation of the scaling/calibration factor and it is showed that it can be accurately estimated. For real-time, distant measurements during the passing of a train on a bridge, the potential of vision-based displacement measurements are shown through field tests on the Manhattan Bridge.

Barthorpe et al. (2009) try to estimate the impact location on a plate representing the skin panel of an aircraft. Piezoceramics are used as strain sensors and ANN methods are applied in the estimation problem. Moreover, the number of sensors is reduced by using the ant colony method and the impact location is estimated with an error less than 2%.

1.3. SHM in Bridge Monitoring

There are several special topics in SHM based on the structure type: high rise structures, buildings, wind turbine, dams, power plants etc. One of the most important issues is apparently the subject of bridge monitoring as it can have implications on the national scale for countries. The bridges are life-lines of transportation networks. This section addresses some studies related to SHM of bridges with the aim of describing recent and general trends.

Pereira (2012) lists the reasons for the collapse of the suspension bridges as follows: problems related to scouring (i.e. Hintze Ribeiro Bridge), construction stage failures (Seongsu Bridge), corrosion (Silver Bridge), and resonance (Tacoma Narrows Bridge).

Taha et al. (2005) present a method based on wavelet-aided fuzzy set theory to quantify damage levels in a system. First of all, acceleration signals are converted to dynamic behavior patterns using a wavelet - neural network module. Secondly, in the damage clustering process, Jeffery's non-informative prior is used in a Bayesian updating scheme with a wavelet domain damage metric (which is a function of measured energy) and predicted signals. The proposed method is tested on the finite element model of a pre-stressed concrete bridge and the results indicate that the method can identify damage levels accurately.

Aktan et al. (1996) present an integrated experimental - analytical research plan for bridge condition assessment methodology. Some of the parameters related with limit state bridge conditions are illustrated as follows: mechanical, chemical characteristics of the materials; initial strains and stresses; initial forces acting on elements or acting on the structure globally; distortions and displacements; stiffness; mass or inertia; damping; natural frequencies and mode shapes. Important terms in condition monitoring such as damage, deterioration, defects, condition assessment, reliability and management concepts are defined. A novel condition assessment methodology is formulated using nondestructive and destructive testing and structural identification of a number of bridge test specimens.

Alampalli et al. (2005) illustrate the cost-benefit aspect of SHM systems in bridge maintenance and present a decision flowchart utilizing SHM techniques (reproduced in Figure 1.1). According to the ratio of maintenance periods with and without SHM systems and the element based costs in maintenance, the benefit of SHM as a function of time is calculated. Two important problems related with bridge monitoring are discussed: (i) corrosion of bridge deck surfaces due to chemicals and salty environments, and (ii) icy conditions on pavements. In order to control the corrosion level, passive chloride detection sensors are suggested to be used by embedding the sensors during the pouring of concrete. These sensors can detect the corrosion level depending on the chloride content. For detection and solution of icy conditions on pavements, use of temperature sensors is recommended in order to detect the wetness of the surface and the amount of chemicals required to thaw the ice in pavements.

Zhang et al. (1998) investigate modal flexibility and its derivative (uniform load surface) as a candidate damage sensitive parameter. Data taken from a cross - county bridge is used in the analysis. In contrast to modal flexibility, the uniform load surface approach does not require information from all degrees of freedom and it is found out to be more sensitive to damage than modal flexibility.

Wang et al. (2000) investigate some of the damage sensitive parameters through a numerical model of the Tsing Ma Bridge. Frequencies, mode shapes, and modal flexibilities are calculated for the intact state and for 10 different damage cases. It is found out that frequency is a less-sensitive parameter to the damage, while by using a few of the lowest frequency modes, modal flexibilities provide a successful indicator for damage locations.

Wong et al. (2000) compare design parameters with response monitoring results for the Tsing Ma Suspension Bridge and two cable stayed bridges using auto/cross-correlation/covariance functions and parameters for time domain, the Fast Fourier Transform (FFT) with level crossing and peak count algorithms for frequency domain, and Mean Square Value function and eight other functions for amplitude domain in the Wind and Structural Health Monitoring System (WASHMS) software. They show that under the critical event (Typhoon York), vertical movements at mid span, vertical accelerations of the

deck, tensile loads in suspenders, strains in the top and bottom cords of the cross - frame, the longitudinal truss and the rocker bearing were all within close proximity to the corresponding design values.

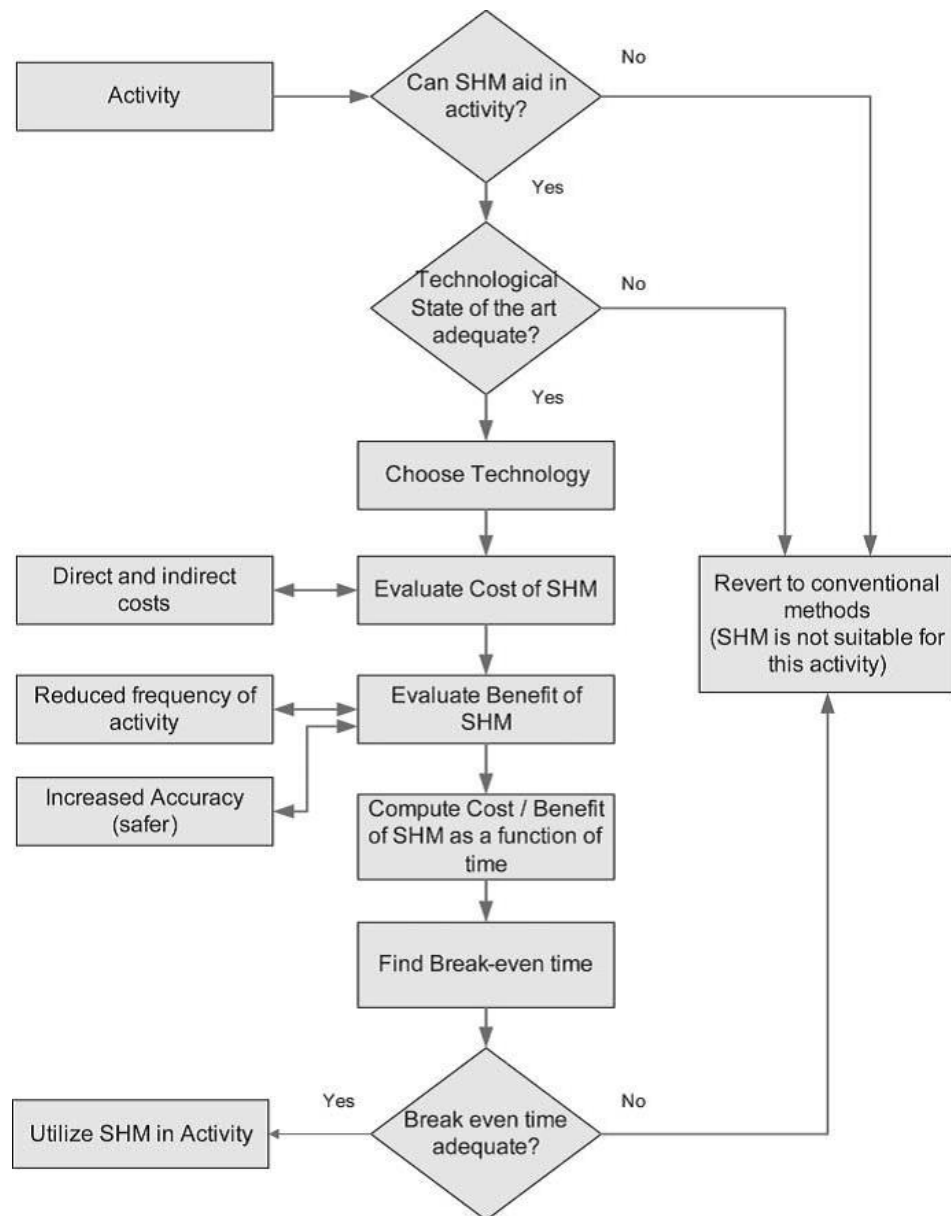


Figure 1.1. SHM utilization for maintenance activities as presented by Alampalli et al. (2005).

Peeters et al. (2001b) fit thermal dynamics included Auto-Regressive model with eXogenous input (ARX) to acceleration data from a healthy bridge and temperature data at one location in order to separate environmental effects from actual damage in the system.

The ARX model is used to calculate frequencies and to estimate confidence intervals. If the variations in frequencies are outside the estimated confidence intervals, it is considered probable that the variations are due to actual damage in the system. As a case study, real data from Z24 Bridge is used and damage is detected successfully under various damage scenarios.

Basseville et al. (2001) use some output only and covariance-driven subspace-based stochastic identification methods in order to detect defect data from multiple sensors and accomplish robustness with respect to different temperature and traffic conditions (non-stationary excitation under operating conditions). When the method is used on real data taken from the Z24 Bridge, results show that in stabilization diagrams spurious modes disappear and only true modes remain with less fluctuation and the damping of the true modes are more accurately estimated.

Verboven (2002) presents a novel frequency-domain maximum likelihood approach using stochastic mode validation criteria. The method is tested on Airbus A320 Slat Track and the I40 Bridge. The main aim of the study is to identify and track modal parameters including closely spaced and crossing modes under forced and ambient vibrations. A fuzzy clustering approach is used to separate physical and computational modes. It is showed that modes can be identified and tracked successfully even for the case where high variations occur in the modal parameters.

Kim et al. (2003) identify natural frequencies using the Potential Modal Ratio approach with a peak picking method. The main aim of the study is to relate frequency changes with mass changes due to traffic. In the case study, the Namhae Suspension Bridge under operating conditions is investigated and it is observed that mass change in normal traffic due to heavy vehicles is negligible compared to the normal operating conditions. For a simply supported bridge, the difference between the natural frequencies of the first vertical mode under heavy and light vehicle is about than 2%.

Nagayama et al. (2005) identify the vibration modes of a full - scale suspension bridge using NExT-ERA. The non - iterative structural inverse method is used to make an inverse analysis of structural properties for the finite element model. The results of the inverse

analysis show that the identified aerodynamic forces are similar to those expected from a wind tunnel experiment. It is also concluded that the damping at the end of the girder is related to the friction force of the bearing/expansion devices.

Siringoringo et al. (2008) analyze the ambient response of the Hakucho Suspension Bridge using Random Decrement combined with the Ibrahim Time Domain technique (RD-ITD) and also NExT-ERA. It is found out that RD-ITD is good for identification of lower and closely spaced modes and the NExT-ERA technique is efficient in dealing with voluminous data. However, the ERA method requires a threshold value. A positive correlation is observed with the wind speed with root mean square of the girder's vertical accelerations. The results show that for lower wind velocity speed, damping decreases and natural frequencies increase. On the other hand, for higher velocity speed and the case where the bearings are unstuck, the aforementioned behavior is reversed.

Moaveni et al. (2012) investigate the effects of ambient temperature on the natural frequencies of a footbridge. Modal parameters are extracted from measured vibration data using an automated data-driven stochastic subspace identification algorithm. The identified natural frequencies and mode shapes are then used for calibration/updating of an initial finite element model by using substructure updating factors. A static polynomial model (fourth-order polynomial regression model) is constructed to represent the relationship between natural frequencies and temperature.

Cross et al. (2013) investigate SSI methods and effects of ambient temperature, traffic loading and wind speed on the dynamic response of the upgraded Tamar Suspension Bridge. The results corresponding to the SSI methods show that the data-driven SSI is found to be more reliable than covariance-driven SSI in tracking the modal parameters. For the results related to the effects of environmental factors on frequency changes, it is found that the traffic load has an impact on the natural frequencies in the short term, while ambient temperature leads to more pronounced effects on long term variations. The effects of wind on the frequencies vary according to the wind speed and direction such that for wind speeds higher than 25 mph and for the bridge's side - on direction, the wind forces lead to significant effects on the natural frequencies.

An et al. (2015) propose a model-free, impulse hammer force vibration test method for damage identification in suspender cables. The normalized curvature difference and curvature difference probability of waveform are used as the damage indicator and it is calculated directly using cable acceleration data. For a numerical suspension bridge example, it is concluded that by using the proposed method, small damages and damages at multiple locations can be detected. It is also concluded that the noise in the response data can be eliminated by increasing pulse excitation magnitude.

Zhang et al. (2016) develop an automated modal analysis using both stabilization diagrams and the SSI algorithm using acceleration measurements from the deck and the towers, and strain and displacement measurements from the deck of the New Carquinez Suspension Bridge. Environmental parameters including ambient temperature, wind speed, and wind direction are investigated using the ridge regression and Gaussian Process Regression (GPR). The results show that GPR appropriately models the relationship between the modal frequencies and the environmental and operational conditions of the bridge.

McNeill et al. (2009) cover data collection, transfer and storage issues for wired sensors. In order to reduce stored data, a novelty index is proposed for utilization in the process. The Frequency Sensitive Competitive Learning technique uses the resulting spectrum obtained via the frequency domain transform of the response measured on the structure. The spectrum is used to calculate the novelty index which is a measure for the novelty of the current response and it may reduce the need for storage of the response data.

Malekjafarian et al. (2015) review indirect methods for bridge monitoring using the responses measured on a vehicle travelling on the bridge. The responses are used to identify the natural frequencies, mode shapes, and damping properties of the bridge. The eventual aim is stated as using these indirect measurement methods to detect the damage in a bridge of interest.

Prendergast et al. (2014) review scour event monitoring for bridges. Scour is defined as the excavation and removal of material from the bed and banks of streams as a result of the erosive action of flowing water, and it is classified in three groups as general, contraction and local scour. Some drawbacks of classical methods are expressed in two main articles as

a summary. The first one is that instruments used in classical methods are expensive, susceptible to damage under flood events, and should be placed close to the scour zone (local). The second drawback is that the interpretation of the results is time consuming and difficult. SHM methods are taken into consideration as a solution to these problems. Instruments of dynamic measurements are easy to install in SHM systems, the risk of flood damage is low, the maintenance cost is not restrictive, and such SHM systems can be used to observe the global properties of the structure. The authors claim that frequency shift sensitivities can be used to estimate the damage due to scouring (Prendergast et al., 2013).

Ahlborn et al. (2010) summarize modern in - situ techniques in which sensors such as accelerometers are used, on-site surveys in which the instruments such as the Ground Penetrating Radars (GPR) are used, and standoff remote sensing techniques in which sensors such as the Interferometric Synthetic Aperture Radars are used for bridge monitoring. Moreover, technical information for SHM used in real bridges is discussed under the case studies section.

Wang et al. (2009) review some of the model based, sensitivity based, and signal processing based methods for the first three levels of damage detection used in SHM of bridges. Condition assessment, feature extraction and some other methods for model updating are briefly summarized.

Darbani et al. (2007) review new directions in Bridge Management Systems (BMS). Importance of wearable technology and decision support systems for bridge inspectors are explained briefly. Benefits of integrating BMS globally with SHM systems are discussed. Instant alarm systems to detect anomalies and local detection with non-destructive evaluation systems through the help of health indices of the elements under consideration are mentioned as some of the benefits of such integrated systems. Moreover, other systems such as asset management, risk management and vehicle routing systems are mentioned. Benefits and drawbacks of using Markov chain forecasting models in prediction of structural condition based on visual inspection data and structural and environmental properties are discussed. Parameters used in the literature for the state of art models for optimization

problems are (i) maintenance, repair and rehabilitation cost, (ii) structural reliability, (iii) user cost, (iv) traffic control, and (v) work zone plans.

Soyoz et al. (2017) report an experimental study design to identify variations in the natural frequencies due to major changes in a bridge due to hanger replacement including a change in hanger orientation. Ambient vibration responses of the bridge are converted to frequency domain spectrums using the Frequency Domain Decomposition method which has proven to be powerful in identifying close modes in the modal parameter extraction process. The results indicate a variation of 9.6% in the first vertical asymmetric modal frequency of the deck and interestingly very small variations in the frequencies for dominant modes of the tower.

Fujino et al. (2013) compare the long - span bridge stock in the US with that in Japan. They note that the average construction date of the long-span bridges in Japan is approximately 10 years later than those in the US. An important conclusion of the study is that by 2020, the maintenance needs for the long span bridges are expected to be significant. The importance of health monitoring of bridges for Japan is emphasized.

Chan et al. (2006) test the effectiveness of Fiber Bragg Grating (FBG) sensors on hanger cables and compare the results with nearby resistive strain gauges located at rocker bearings and truss girders (of the supporting structure) of the Tsing Ma Bridge. Some of the FBG sensors are used as strain free sensors so as to compensate temperature effects in the measurements. Tsing Ma Bridge carries both railways and highways and the results show that passage of trains and high traffic load can be detected by the FBG sensors located at the hangers. Moreover, FBG sensors are shown to be in excellent agreement with conventional ones located at rocker bearings and truss girders.

1.4. Thesis Outline and Main Contributions

This thesis aims to develop and discuss a robust damage indicator which may be used reliably to identify the existence and location of damage in a structure. The particular structures for which the method is suitable are beams and beam-like structures such as

bridges and buildings. In so doing, the thesis also addresses system identification methods that may be used to analyze the data to evaluate the proposed indicator, and instrumentation schemes that will help reduce false positives or false negatives which may result from the particular approach developed.

In the first chapter, SHM systems, their aims and tools are introduced. Moreover, the existing literature on SHM is reviewed to some extent. The interdisciplinary side of the SHM is emphasized, and some studies related to bridge monitoring are summarized.

The second chapter deals with sensitivity-based damage identification. In this chapter, to motivate the chosen framework, some important studies related to sensitivity-based methods are reviewed. A baseline dependent parameter and a procedure to use this parameter for higher modes is introduced. The performance of the proposed system identification and damage detection methods are investigated numerically.

The third chapter is related to system identification. In this chapter, modal plots, count plots, modal points and modal zones are introduced. These concepts and methods are explained and their applicability to data analysis with the aim of providing the necessary parameters to the proposed damage indicator is discussed. The properties of modal plots, which may be used for both damage detection and system identification, are discussed in Section 3.4.

In the numerical part of the fourth chapter, three case studies comprising spring mass chain systems are investigated under varying damage scenarios. In Section 4.3, the saddle point criteria which has been identified in relation to the proposed the damage detection method is addressed by a sensor deployment suggestion. In the experimental part of the fourth chapter, a possibility of utilizing modal plots in the damage existence problem is identified through an experimental study (Section 4.4). The location of damage is detected for the closed system of Section 4.5 using the damage indicator proposed in Chapter 2.

In Chapter 5, a six-story building model is discussed in detail. A hundred and nineteen damage scenarios, out of which ninety are single damage locations, are considered. The

efficiency of the damage indicator, using both single modes and multiple modes as proposed in Chapter 2, is demonstrated through these damage scenarios.

In Chapter 6, data from a five-story real structure is investigated and the count plot is used to investigate the natural frequency changes between the undamaged state and a damaged state of the structure.

An evaluation of the proposed methods, related conclusions and possible directions for future research are discussed in Chapter 7.

2. DAMAGE DETECTION

2.1. Classification of Damage:

Damage is a word that encompasses many scales and severities. A unique definition generally requires the identification of certain thresholds which invariably depend on the specific application. It is generally agreed, however, that damage identification methods can be systematically categorized in the following order [see, e.g., (Rytter, 1993; Fassosi et al., 2009)]:

Level 0: (Fault Detection) Determining whether damage exists in the structure.

Level 1: (Fault Identification) Detection of the geometric location of the damage.

Level 2: (Magnitude Estimation) Quantification of the severity of the damage.

Level 3: Prediction of the remaining service life of the structure.

In addition to the aforementioned levels, some researchers (Ayres et al., 1998) place additional emphasis on the importance of discrimination of damage type. Some of the examples of damage types encountered in civil engineering structures are cracking, corrosion, plastification, loss of rigidity, material deterioration, and loosening of connections.

In the existing literature, studies related to the effect of damage on modal variables have revealed that for minor damage states, the resulting changes in natural-frequencies are linearly related to the severity of damage and are non-linearly related to its location (Gladwell, 2004). Therefore, when the extent of damage is small, if the location of the damage (Level 1) is identified properly, then the determination of the extent of damage (Level 2) becomes easier. Moreover, it is a trivial observation that the fault identification (Level 1) problem covers the fault detection (Level 0) problem. Therefore, the Level 1 problem has been the main focus in most of the studies (Doebbling et al. 1996). Conducting a proper Level 0 fault detection, however, is also vital for the subsequent levels. One of the

goals of this study is to show that Level 0 damage detection can be accomplished by using the first modal information (Yuen, 1985; Dong et al., 1994).

2.2. Determination of Damage Sensitive Parameters

Performing a robust evaluation of the structure and determining reliable damage indicators which are strongly associated with the system's *capacity* (damage sensitive features) are crucial factors in the condition assessment of a given structure. Furthermore, the external effects (input forces) in the surrounding environment must be elaborately investigated and comprehended. Upon identification of the capacity, it is required to evaluate the response (*demand*) under the operating condition of the system.

Vibration-based methods aim to use damage sensitive features that are simple, computationally not demanding, easily estimated, sensitive to changes in the capacity, and not sensitive to changes in demand. Some of the features used in the literature, simple to complex, are modal parameters (frequencies, mode shapes, (less frequently) damping, and modal scaling factors), signal parameters (e.g. cepstrum and electromyography signals), and model parameters (e.g. autoregressive model parameters). In this thesis, modal variables are used as damage indicators and some of the sensitivity based methods related to modal parameters are discussed in the next section.

2.3. Sensitivity Based Damage Identification Methods

Studies that relate changes in modal variables to damage are classified under sensitivity-based methods. In the first years of SHM studies, it was generally assumed that one formula or definition would be appropriate for all kinds of structures like offshore platforms, towers and buildings. Even the definition of damage levels expressed by Rytter (1993) is a reflection of this idea. This is one of the reasons why significant efforts were spent on sensitivity methods. On the other hand, data from experiments discourage hopes in the "one method for all systems" concept. In what follows some of the important studies on sensitivity based damage detection are discussed.

The initial studies on damage detection have addressed associations of changes in the natural-frequencies with the changes in the mass and/or stiffness matrices. Researchers have often employed natural frequencies as the damage indicating modal parameters, since these frequencies can be easily estimated with high confidence. Because natural-frequencies do not explicitly contain geometric information, their use often comes to the fore in Level 0 applications where the presence of the damage is to be detected. There are studies, however, that attempt to identify the location of damage using the first six or more natural-frequencies. In studies (Cawley et al.,1979; Hearn et al., 1991), a method is proposed to estimate the location and extent of damage using only natural frequencies, employing a numerical model of the structure to be investigated. Using the principle of conservation of energy and assuming damage stems from a change in stiffness while ignoring changes in the system mass, the following relation between member stiffness change and natural frequency change for a single member is derived

$$\Delta\omega_j^2 = \frac{\varepsilon_i^T(\Phi_j)\Delta k_i\varepsilon_i(\Phi_j)}{\Phi_j^T M \Phi_j} . \quad (2.1)$$

In this expression, ω_j and Φ_j are the frequency and the mode shape for the j th mode, Δ denotes the change in the quantity that it precedes, ε_i stands for a transformation matrix to convert the local stiffness matrix of the i th element to global coordinates. M and k_i are the global mass matrix of the system and the stiffness of the i th element. In order to estimate the damage location, all previously compiled damage scenarios (database of ‘characteristic’ modal values obtained via numerical simulations on a numerical model) are compared with the ‘observed’ damaged state [not necessarily limited to the scenarios included in the database]

$$E = \frac{1}{N} \sum_{j,n} \left[\left(\frac{\Delta\omega_j^2}{\Delta\omega_n^2} \right)_{i \text{ Observed}} - \left(\frac{\Delta\omega_j^2}{\Delta\omega_n^2} \right)_{i \text{ Characteristic}} \right]^2 . \quad (2.2)$$

In this expression, E stands for mean square error between observed (measured) and characteristic frequency change ratios, N stands for number of members, sub-indices j and n stand for mode numbers, and the sub-index i stands for member number. The performance

of the algorithm is tested through experiments performed on a welded steel frame and on a wire rope, and the results show that detecting damage location for one member is possible using natural frequency changes without using mode shapes. It is also discussed that for the transverse motion of the wire rope natural frequencies and mode shapes are insensitive to damage and that damping may be the only indication of distress. The main drawback of these approaches is that, a slight error in the natural-frequencies can lead to very significant errors in estimates of geometric location of damage.

In Level 1 applications, mode shapes and their derivatives are often used, and the second derivative of a mode shape is found to be sensitive to minor changes in the system. In the study (Pandey et al., 1991) curvatures of mass-normalized mode shapes are used as damage sensitive features and it is tested on finite element models of simply supported and cantilever beams in order to identify the existence of damage and its location. Mode shape curvatures are calculated using the central difference approximation given by

$$\Phi''_{j,i} = (\Phi_{j,i+1} - 2\Phi_{j,i} + \Phi_{j,i-1})/h^2, \quad (2.3)$$

where Φ stands for a mode shape, sub-indices j and i stand respectively for mode number and DOF counters, $\Phi''_{j,i}$ denotes the central difference estimate of the curvature of the j th mode shape at the i th node, and h stands for the spatial distance between two consecutive nodes. A damaged member is detected using the maximum absolute difference between damaged and undamaged member mode shape curvatures calculated via

$$\Delta\Phi'' = |(\Phi^d)'' - \Phi''|, \quad (2.4)$$

where the superscript d indicates that the mode shape belongs to damaged system. The results show that (i) mode shape curvature may localize the damage while mode shapes cannot, and (ii) natural frequencies can be used to detect presence of damage and the mode shape curvatures can be used to detect its location(s).

Wahab et al. (1999) use the damage indicator discussed above on the simulated data from the model of a simply supported beam and real data from the pre-stressed concrete bridge (referred to in the literature as the Z24 Bridge). It is concluded that for the simply

supported beam: (i) the lower modes are identified more accurately than higher modes; (ii) it is not possible to detect multiple damage locations using only a single mode information; (iii) as the number of measurements increases, the technique gives more accurate results. For the Z24 Bridge data, curve fitting is required before the calculation of mode shape curvatures, and the method proposed by Pandey et al. (1991) is found promising. Other researchers (see e.g. Teughels et al. (2002)), however, have claimed that “modal curvatures seem to be much more sensitive to small perturbations in the system than modal displacements. However, the drawback of this approach is that the estimation of the modal curvatures suffers from a large statistical uncertainty”. Therefore the second derivative of the mode shapes can only be detected with large uncertainties which make the use of this parameter ineffective.

Yazdanpanah et al. (2015) propose a new damage indicator which is a function of mode shapes, mode shape derivatives and mode shape curvatures. The proposed damage indicator is compared with the method proposed by Wahab et al. (1999) through a numerical example of simply supported one or two span beams with different numbers of elements of finite element models. The results show that the proposed method is slightly more sensitive to damage location than that of the done by Wahab et al. (1999).

Gandomi et al. (2008) review the articles on damage detection using either the mode shapes or mode shape derivatives so as to determine which of the two parameters is more sensitive in fault identification. As a result, they conclude that the parameters related to the mode shape changes are more precise.

One of the original and promising recommendations in this regard is developed by Yuen (1985) as the proposed damage indicator contains both natural frequencies and their corresponding mode shapes. In this study, a finite element model of a cantilever beam is examined. The damage in the cantilever is represented by the reduction of the modulus of elasticity. The following indicators are proposed to reflect well both the location and the size of the crack in the cantilever:

$$\Phi_{j,i}^* = \frac{\Phi_{j,i}^d}{(\omega_j^d)^2} - \frac{\Phi_{j,i}}{(\omega_j)^2} , \quad (2.5a)$$

$$\theta_{j,i}^* = \frac{\theta_{j,i}^d}{(\omega_j^d)^2} - \frac{\theta_{j,i}}{(\omega_j)^2} . \quad (2.5b)$$

In these expressions, Φ and θ are the mass normalized translational and rotational mode shapes, respectively; ω is the natural frequency; subindex j is the mode number; subindex i signifies the counter for the DOFs, superscript d shows that a parameter belongs to the damaged system. Although the mode number is indicated here by j , Equations 2.5 are proposed by Yuen (1985) only for the first modes. It should be noted that as in the study done by Pandey et al. (1991), the parameters proposed by Yuen (1985) are also dependent on baseline data.

In Yuen (1985), the method proposed by Yuen (1985) is applied to a beam with both its ends fixed by using data from a finite element model established in line with the fracture theory, as well as using an experimental data set. It is shown that damage may be detected but not as conveniently as in the cantilever beam example in Yuen (1985) and the efficiency of the method is increased by using the strain mode shapes.

2.4. Method Proposal

2.4.1. Initial Enhancements

As part of the present study, detailed analyses are carried out on the promising method developed by Yuen (1985). As a result of numerous numerical analyses, a new method is developed in which Yuen's method is simplified. In the proposed approach, mode shapes are not normalized by the mass matrix but rather they are normalized according to a reference DOF in Equation 2.5. With this simplification, the necessity to know (or calculate) the mass matrix is eliminated. In the preliminary analyses different powers of natural frequencies are tested on numerical examples, and the best difference is attained at power 1 (one). Therefore, instead of the eigenvalues (squares of natural-frequency values) in the denominator, the

values of the natural-frequencies themselves are used. Moreover, differences of the mode shapes between the nodes are used instead of the mode shapes. These steps and the proposed damage indicator can be summarized with the following equations

$$\phi_{j,i} = \frac{\Phi_{j,i}^a}{\Phi_{j,R}} , \quad (2.6)$$

$$\Delta\phi_{j,i} = \phi_{j,i} - \phi_{j,i-1} , \quad (2.7)$$

$$\phi_{j,i}^* = \frac{\Delta\phi_{j,i}^d}{\omega_j^d} - \frac{\Delta\phi_{j,i}}{\omega_j} . \quad (2.8)$$

In these expressions, $\Phi_{j,i}^a$ is the component of the arbitrarily scaled j th mode shape at the i th node, $\Phi_{j,R}$ is the value of the j th mode shape at the reference node, so that ϕ_j is scaled to have a unit value on the reference node.

Since the damage indicator defined by Equations (2.9) through (2.10) is claimed to improve Yuen's (1985) proposal, a comparative study is provided in the next section.

2.4.2. Comparison of the Initial Proposal with Yuen's Proposal

In this section, a Bernoulli-Euler cantilever beam with a uniform cross-section is used to generate relevant data. The section and model properties are given in Figure 2.1. For each element, rotational and translational DOFs are defined.

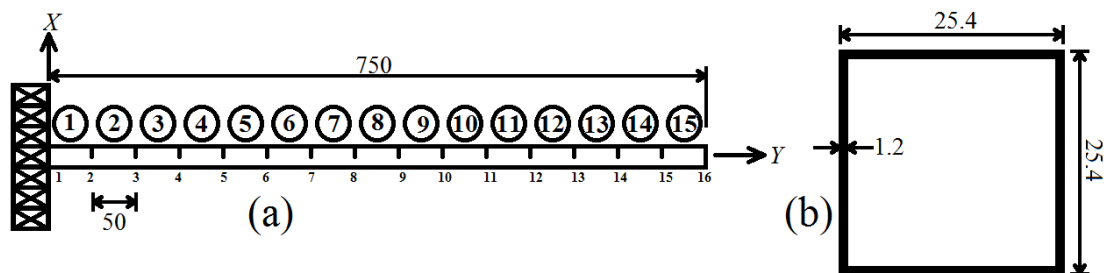


Figure 2.1. Cantilever model (a) finite element model with element and node numbers. (b) cross-section of the beam (all dimensions in mm).

Initially, modulus of elasticity is taken as $E = 208000 \text{ N/mm}^2$ and the mass density is $\rho = 7.8 \text{ kg/mm}^3$. Damage is defined as a decrease in the modulus of elasticity so that not

the inertia but stiffness matrix would change. The natural frequencies and mode shapes are calculated by solving the eigenvalue problem of the damaged and undamaged systems.

First, for all members, the elastic modulus is dropped to its half for each element one by one, and it is seen that both damage indicators in Yuen (1985) correctly indicate the damage location. The translational eigenparameter changes slope and the rotational damage indicator takes a step jump on damage element for each case. As an illustrative example, Figure 2.2 shows the damage indicators given in Equation 2.5 for damage located on element 10.

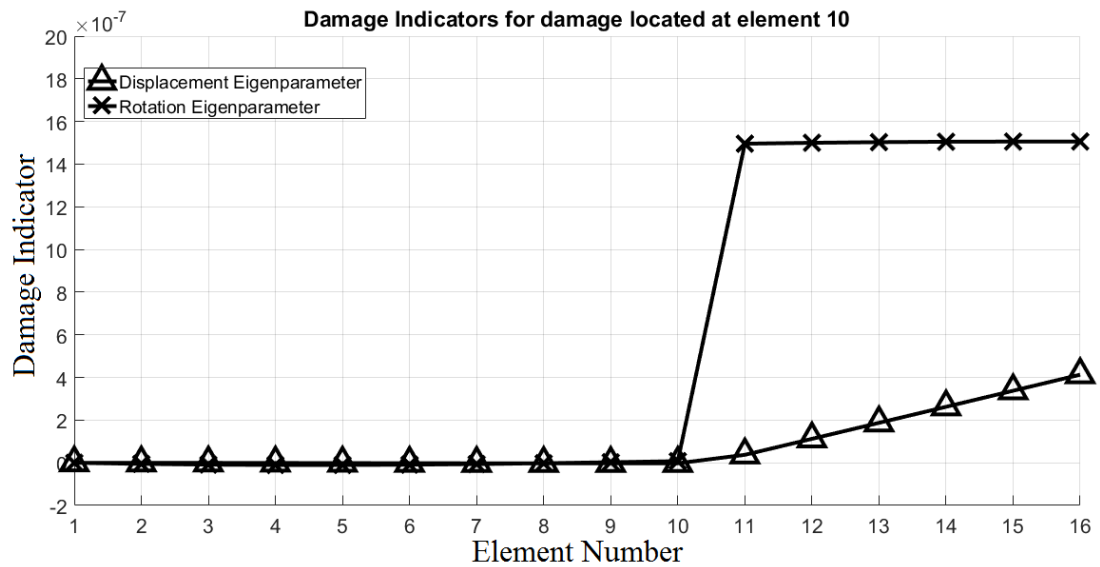


Figure 2.2. Yuen's (1985) damage indicators for damage located on element 10.

As far as the proposed damage indicator defined by Equation 2.8 is concerned, the damage indicator takes a positive value on the damages element while for other nodes it takes comparatively very small and sometimes even negative values as seen in Figure 2.3.-

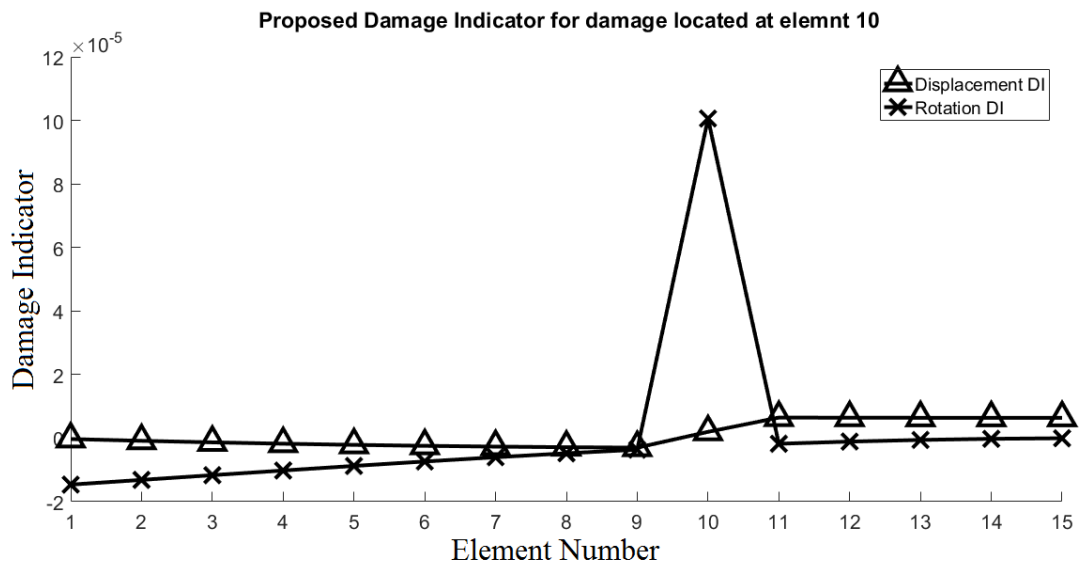


Figure 2.3. Proposed damage Indicators for damage located on element 10.

Figure 2.4 shows that the displacement eigenparameter changes slope between nodes where damage locates and the slope becomes steeper afterward and remains constant to the tip of the cantilever.

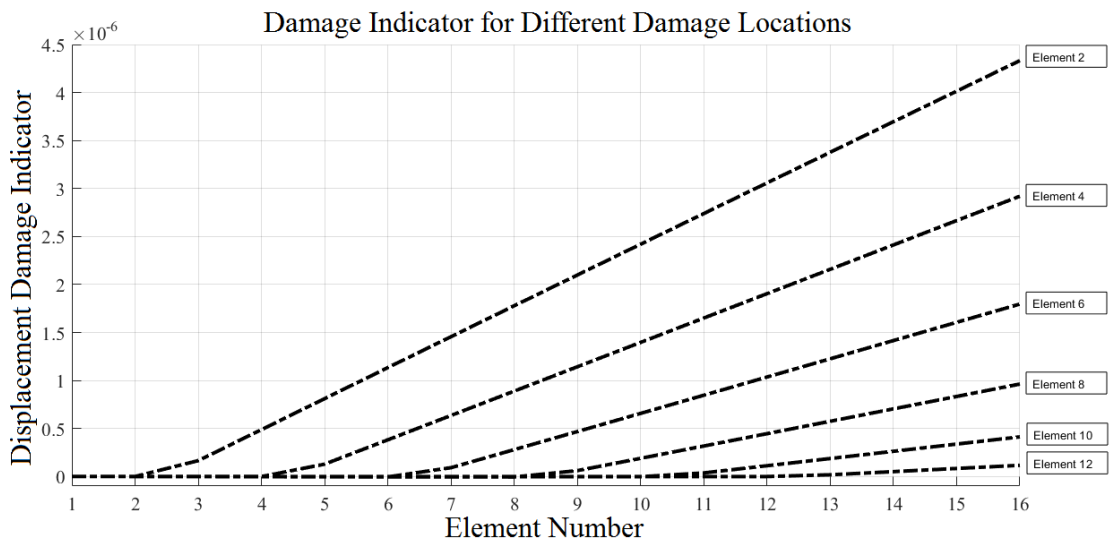


Figure 2.4. Proposed translational damage indicator for different damage locations.

The proposed rotational damage indicator takes a positive value between the nodes where damage is located while it is very small or negative on other elements as seen in Figure 2.5.

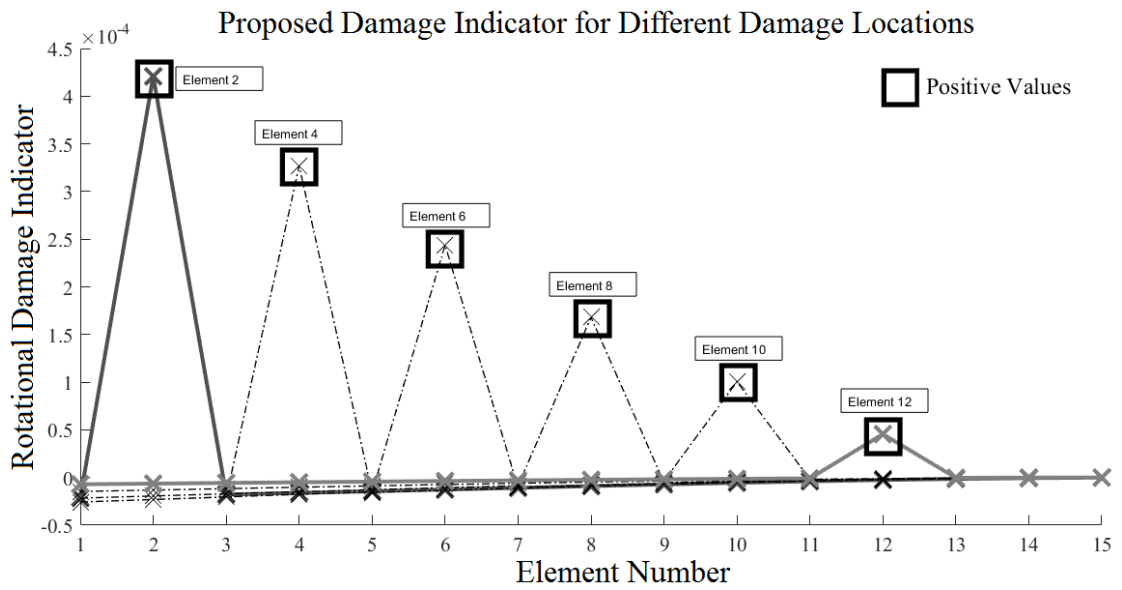


Figure 2.5. Proposed rotational damage indicator for different damage locations.

For varying levels of damage, the slope in the displacement eigenparameter increases and the damage extent can be identified from slope change (Figure 2.6). On the other hand, for the proposed rotational damage indicator, the amplitude of the damage parameter at the damage location increases with increasing damage (Figure 2.7).

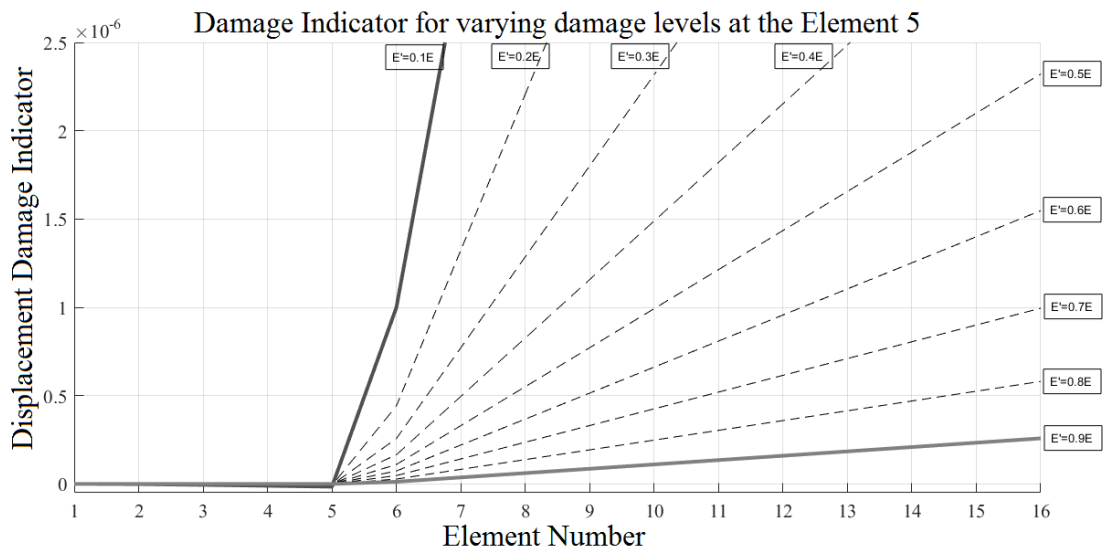


Figure 2.6. Proposed translational damage indicator for varying degrees of damage on element 5.

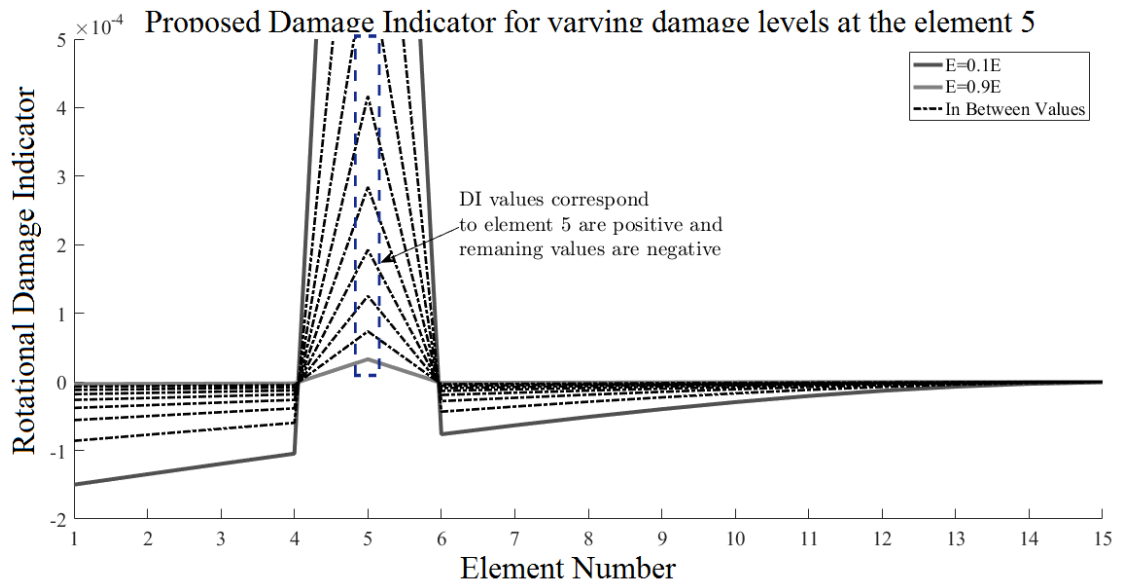


Figure 2.7. Proposed rotational damage indicator for varying levels of damage on element 5.

For this example, the damage indicators proposed by Yuen (1985) can detect damage; however, the proposed damage indicator after first improvements is still superior because there is no need to use mass normalized mode shapes in the proposed indicator,

Both the parameters used in Yuen (1985) (Equations 2.5) and the proposed first improvements (Equation 2.8) may only be used in detection of damage in a fix-free chain (sequential spring - mass) model with the first mode information since for the first mode of such a model, the differences between the mode shape components across the nodes keep the same sign (the first mode shape is monotonically increasing). In order to use the damage indicator for other modes and different boundary conditions, the second set of improvements as per discussed below are required.

2.4.3. Further Enhancements

With the second enhancement procedure, the damage indicator is modified and damage can be identified by using either an individual mode or a cumulative set of modes. Moreover, it is shown that the proposed method can be used for the mass-spring systems with different end conditions (See Section 2.5).

The damage indicator calculated by Equation 2.8 is not compatible with a mode shape containing ‘saddle points’ i.e. a region where the mode shape difference calculated via Equation 2.7 alters sign. In order to use the proposed approach in such cases, the mode shapes are first transformed into increasing functions and the same process is adapted. After this transformation, the damage indicator may be meaningfully calculated for any mode. Damage detection, however, is negatively affected if damage occurs on regions containing saddle points since there the difference calculated over the transformed modeshape change would be zero.

To calculate the proposed damage indicator using any mode, the following steps should be followed:

i. In order to convert the mode shape to an increasing function, the absolute value of the mode shape difference is used and these differences are summed

$$\Delta\Phi_{j,i} = |\Phi_{j,i} - \Phi_{j,i-1}|, \quad (2.11)$$

$$\tilde{\phi}_{j,i} = \sum_{k=1}^i \Delta\Phi_{j,k}. \quad (2.12)$$

ii. In order to apply the proposed method for damage identification via the calculated mode-shape like $\tilde{\phi}_j$ vector, the vector is normalized by its value $\tilde{\phi}_{j,R}$ at the reference DOF and the differences of the normalized vector relative to the DOFs are calculated

$$\check{\phi}_{j,i} = \frac{\tilde{\phi}_{j,i}}{\tilde{\phi}_{j,R}}, \quad (2.13)$$

$$\Delta\check{\phi}_{j,i} = \check{\phi}_{j,i} - \check{\phi}_{j,i-1}. \quad (2.14)$$

iii. Finally, the damage indicator is defined similarly to Equation 2.8 for any mode

$$\phi_{j,i}^* = \frac{\Delta\check{\phi}_{j,i}^d}{\omega_j^d} - \frac{\Delta\check{\phi}_{j,i}}{\omega_j}. \quad (2.15)$$

This damage indicator can be calculated separately for the first two or three modes, and it is also possible to evaluate two or three modes together. On the other hand, as the number of modes increases, the number of the saddle points also increases and such saddle points adversely affect damage detection, so the use of the first two or three modes is recommended. In order to take into account different modes simultaneously, the cumulative damage indicator ϕ_i^* is defined as

$$\phi_i^* = \sum_{j=1}^{n_m} \left(\frac{\Delta\check{\phi}_{j,i}^d}{\omega_j^d} - \frac{\Delta\check{\phi}_{j,i}}{\omega_j} \right), \quad (2.16)$$

where n_m denotes the number of modes that will be included in the calculations of the index. Both damage indicators may be normalized by their maximum values as

$$\bar{\phi}_{j,i} = \frac{\phi_{j,i}^*}{\max_i \phi_{j,i}^*} \quad \text{or} \quad \bar{\phi}_i = \frac{\phi_i^*}{\max_i \phi_i^*}. \quad (2.17)$$

For ease of reference, Equation (2. 18), or its scaled equivalent given as the first expression in Equation (2. 19), will be referred to as the ‘single-mode damage indicator’ whereas Equation (2. 20), or its scaled equivalent given as the second expression in Equation (2. 21), will be referred to as the ‘multi-mode damage indicator’. It should be noted that by the normalization step in Equation 2.15, information regarding the extent of damage is lost (see Section 4.5). Another important issue is that if rotations are explicitly defined as DOFs, a rotational modal shape may be used instead of translational mode shapes.

Since the proposed damage indicators are associated with how the mode shape changes across nodes, it is possible to say that the probable damage is between the detected measurement point and the previous measurement location. For the case where all DOFs are instrumented, damage between the nodes can be associated with the spring number in the chain model. If the number of measurements is less than the number of DOFs, it will still be possible to relate the location of the probable damage to a node since the damage indicator will indicate the first measurement point following the damaged spring(s).

2.5. Case Studies

2.5.1. A Numerical Demonstration of the Proposed Fault Identification Method

In this section, a case of the known damage states and a known system, where each variable can be accurately calculated, is considered. The main aim is to examine the effectiveness of the proposed damage detection method under a number of damage conditions for a 100-DOF spring-mass chain system shown in Figure 2.8. Two different boundary conditions are considered: (i) the "cantilever" system, in which only the spring at one end is attached to a stationary point, (ii) the "simply supported" system where the springs at both ends are attached to stationary points.

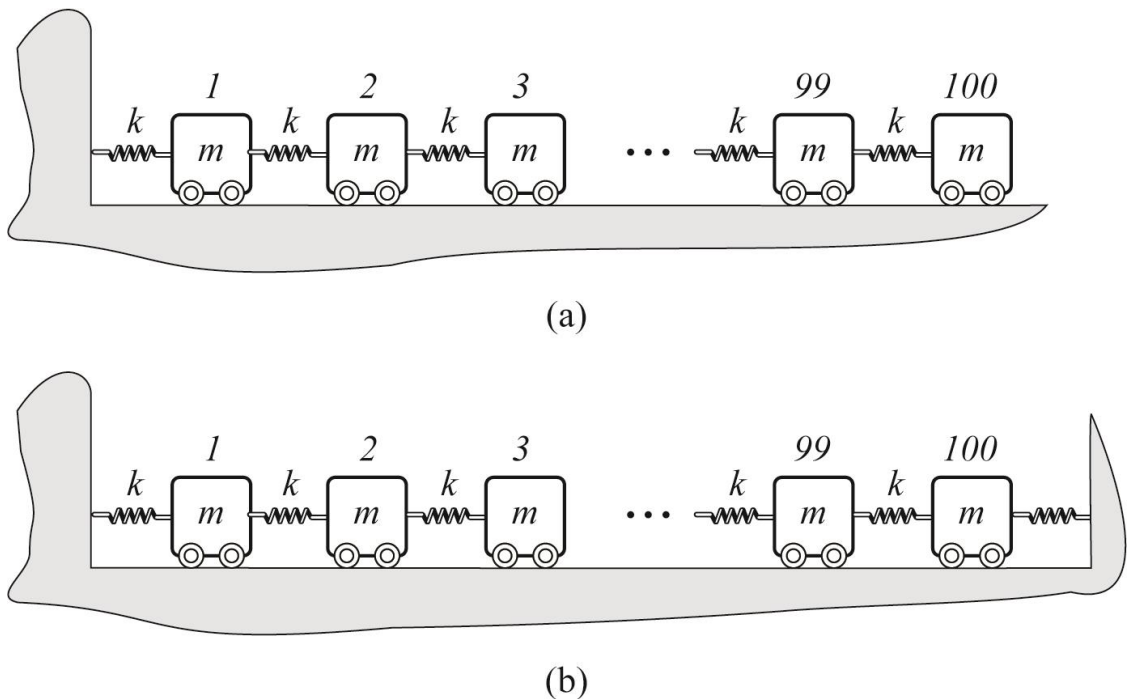


Figure 2.8. 100 DOF spring – mass chain systems: (a) the ‘cantilever’ system, (b) the ‘simply supported’ system.

In the undamaged system, all masses and spring constants are defined as m and k respectively. In the cantilever systems, the nodes (masses) are numbered starting from the fixed end and increasing toward the free end (springs are numbered similarly); in the simply supported systems, the numbering can be initiated from either end. In the numerical

demonstration, it is desired that all modal parameters are accurate and that possible errors due to the system identification step do not play a role. Therefore, natural frequencies and mode shapes are calculated by solving the eigenvalue problem of the related systems.

To demonstrate that the proposed method can locate damage at any location, for the first set of tests, springs are damaged one by one (one damaged spring per test) by inducing 5% reduction in the spring stiffness and the damage indicator of Equation 2.15 is calculated for each case. Figure 2.9 shows the values of the damage indicators calculated using Equation 2.15 for a 5% stiffness reduction in the 1st, 30th, 51st and 90th springs, respectively. For each case, $\bar{\phi}_{1,i}$ values to be obtained by using the first mode and $\bar{\phi}_i$ values obtained by using the first three modes are shown on the same figure.

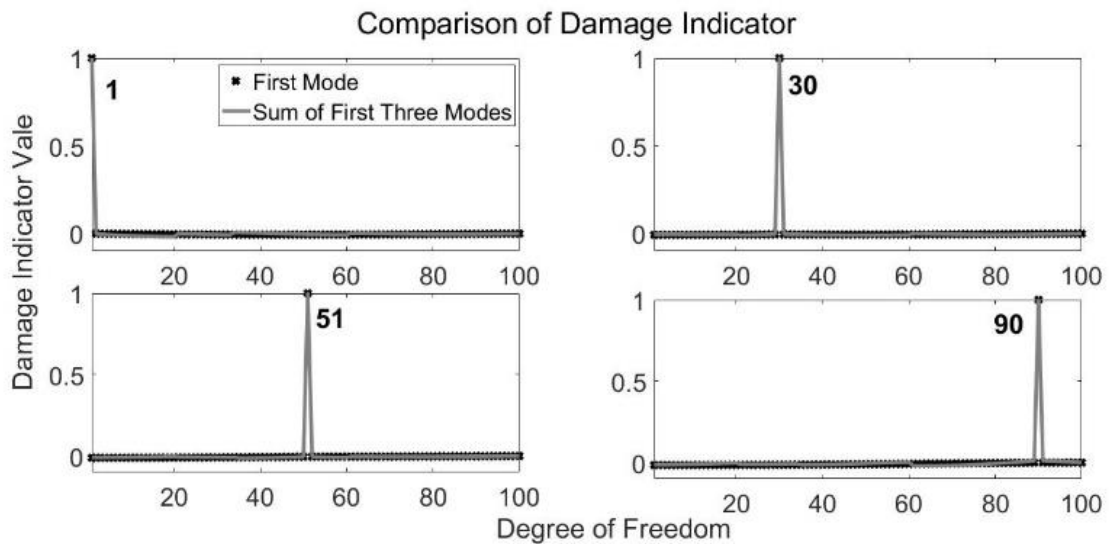


Figure 2.9. Damage Indicator values calculated via the first mode and the first three modes in the case of a 5% stiffness reduction in the 1st, 30th, 51th and 90th springs.

As can be seen in Figure 2.9 the proposed damage indicator takes on a value of 1 (one) at the node right after the damaged spring, and a value close to zero at all the other nodes. The observation that the magnitude of the value obtained at the damaged element is several times greater than the value obtained at the undamaged nodes enables the damage location to be easily identified (which in this case is the spring connecting the peak valued node to the previous one). The damage indicator value calculated using Equation 2.15 always takes

on a value of 1 at the critical node. For each damaged case in each of which only one spring is damaged, the largest and the smallest values of the damage indicator at all the other nodes are plotted in Figure 2.10 wherein the horizontal axis shows the number of the damaged spring and the vertical axes shows the largest and smallest values of the damage indicator calculated at all the nodes other than the critical one (of which there are 99 values). It is understood that the value of the damage indicator at the critical node, which is by definition equal to one, is approximately 50 to 100 times greater than its values observed all the other nodes, thereby indicating a significant difference that would help in clearly distinguishing the damage location.

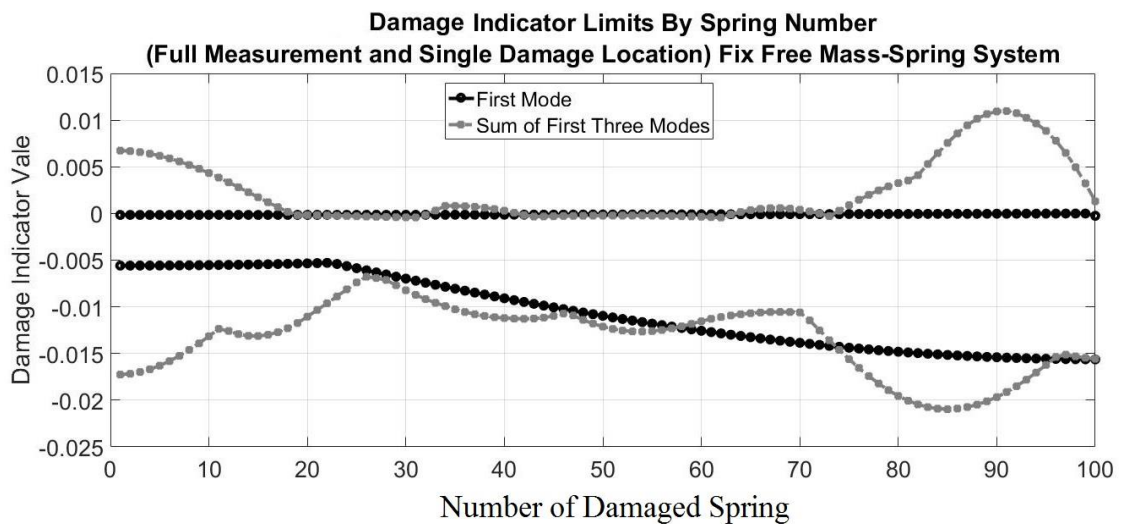


Figure 2.10. A summary representation of the largest and smallest values that the damage indicator takes at the undamaged positions for the cantilever system (for a 5% reduction in spring stiffness).

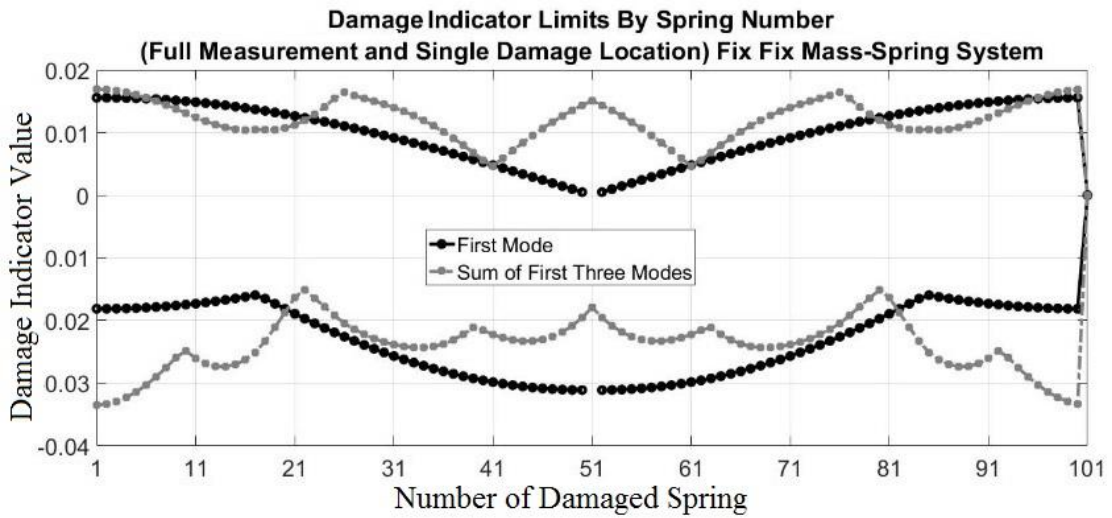


Figure 2.11. A summary representation of the largest and smallest values of the damage indicator in undamaged positions for a simply supported chain system (for a 5% reduction in spring stiffness).

A similar comparison is done for the simply supported system and plotted in Figure 2.11. Similarly, the value of the damage indicator at the critical node, is 50 to 100 times larger than its values observed at all the other nodes. In the case where the spring corresponding to the symmetry axis is damaged, the first mode natural-frequency and mode-shape of the damaged and undamaged systems are equal.

2.5.2. A Numerical Demonstration of the Proposed Fault Identification Method under Limited Measurement Locations

The number of measurement locations, which will henceforth be simply referred to as nodes, is almost always less than the number of DOFs in practice. Therefore, the case study reported in this section discusses the validity of the proposed method under limited number of measurements. The 100 DOF cantilever system used in Section 2.5.1 is investigated in this case study using few measurement points such that the mode shapes are assumed to be known (exactly) at every 10th DOF starting at the 10th DOF (10th, 20th, ... , 100th).

At first, the case of single damage location is investigated and the rigidity of each spring is reduced by 5% sequentially as was done in the previous section. The damage

indicator defined by Equation 2.15 will again take on a value of 1 at the critical node for each damage case and the largest and smallest values of the damage indicator at all the other nodes are plotted in Figure 2.12 wherein the horizontal axis shows the number of the damaged spring and the vertical axes shows the largest and smallest values of the damage indicator calculated at all the nodes other than critical one (of which there are now 9 values). Again a hundred number of cases exists for the single damage location case. Therefore, Figure 2.12 shows the limits of 9 values (other than indicated damaged zone i.e. 1st to 10th nodes) for 100 damage scenarios for the single-mode and the multi-mode damage indicators.

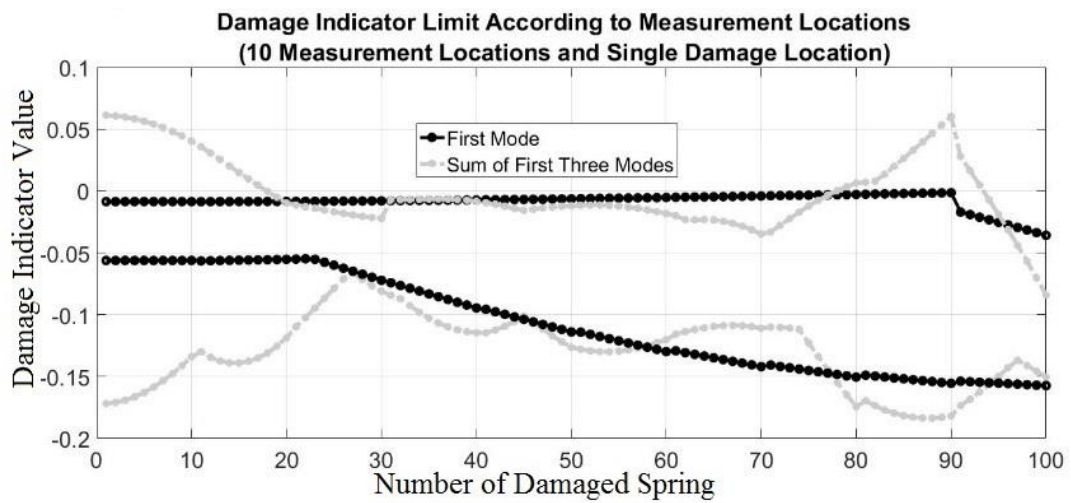


Figure 2.12. Summary view of the first mode and the first three modes undamaged indicator.

It is observed in Figure 2.12 that the single-mode damage indicator values calculated using the first mode has a negative value on the nodes away from the damage location. For the multi-mode damage indicator calculated using the first three modes, the ratio between its values calculated for the damaged and undamaged nodes is greater than 10.

As far as simultaneous damage at multiple locations is concerned, two different cases are next discussed: (i) reduced stiffness values for the 55th and the 67th springs and (ii) reduced stiffness values for the 23rd and the 78th springs. As shown in Figure 2.13, the proposed damage indicators clearly indicate that the damage is somewhere between the 50th and the 70th DOFs for the first scenario of the 55th and 67th springs damaged, and somewhere between the 20th and the 30th and between the 70th and the 80th DOFs for the

second damage scenario of the 23rd and 78th springs damaged. The numerical results demonstrate that even with limited measurement locations, it is possible to determine both single and multiple damage locations using the proposed damage indicators.

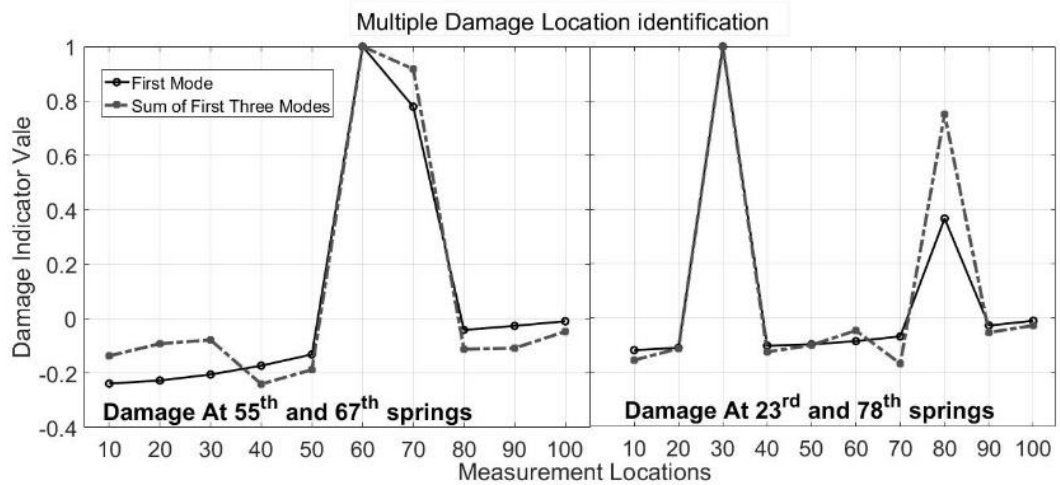


Figure 2.13. Damage Indicator for the first mode and for the sum of first three modes (Few Measurements and Multiple Damage Location).

3. SYSTEM IDENTIFICATION

In linear systems, modal analysis can be considered valid when the structure is vibrating under ambient inputs. In discrete systems, the number of natural frequencies and the mode shapes, in theory, is equal to number of the degrees of freedom of the structure. Often it is assumed that the number of sensors deployed on the structure does not limit the number of natural frequencies that can be identified via measured vibration data. Since, however, the higher modes do not generally contribute significantly to the global response, it may not be possible to determine these high modes from measurements. The determination of a mode shape, on the other hand, would certainly be limited by the number of sensors used.

In order to determine the dynamic variables such as natural frequencies, mode shapes, and damping ratios, many methods have been proposed in the literature. It is possible to classify these approaches under two main categories: Frequency domain methods and time domain methods. It is stated that the frequency domain methods are suitable for systems having modal damping ratios higher than 0.3% and that time domain methods are appropriate for systems with modal damping ratios less than 5% (Heylen et al., 1997). Civil engineering structures are generally within these limits.

The Fourier transform and frequency response functions (FRF) are frequently used in the frequency domain methods. The system is defined by its FRF, which is essentially a transfer function that contains the dynamic characteristics of the system. The FRF can be calculated as the ratio of the Fourier transform of the response to the Fourier transform of the input force. When the amplitude of the FRF, which is a complex function, is plotted, the frequency values corresponding to the peaks are considered to be the natural frequencies of the structure. The mode shapes can be determined by evaluating the ratio of the amplitudes of the peaks for each sensor, together with the angle of the FRF (Armstrong et al., 1995). If it is assumed that the PSD of the input force under operating loads is approximately equal in all frequency values (white noise assumption), the natural frequencies and the mode shapes

can be calculated directly via the Fourier transform of the response. If the input forces do not comply with the white noise assumption, the history of the input forces must be measured and should be taken into account. The two most important problems of frequency domain methods are the generation of new frequencies (spectral leakage) that are not related to the natural frequencies of the structure, and a noisy FRF from the noise-free data while converting from time-domain to frequency domain under operating loads (Schoukens et al., 2004).

Time domain methods are also frequently used in system identification. These methods generally construct a model based only on response measurements or both response and input time histories, and the identified model in turn is employed in calculating the modal variables. An important issue is to determine the model order correctly so that the model is consistent with the data (Schwarz, 1978). Although true modes are expected to be present in the model when proper order is chosen, in practice computational modes (that reduce the undesirable effects such as noise and leakage in the data (Zhang et al., 1987, 2010) and are thought to be irrelevant to the system characteristics) also creep into the model besides the actual, physical modes of the structure. As to be expected, the number of computational modes increase as the model order increases. Observability and controllability issues also lead to limiting the estimates to only a certain number of structural modes. For these reasons, the choice of the model order and the discrimination of physical and computational modes have been addressed by many researchers in the context of time domain methods (Schwarz, 1978; Akaike, 1974). There are various tools that are used to solve the aforementioned issues, and one of them is the stabilization diagram approach.

3.1. Stabilization Diagrams

In some of the time-domain methods, the model order must be ‘selected’ at one stage. Precise determination of the model order is a difficult step due to the deviations of modelling assumptions from the actual state of things as well as the presence of noise in the data. In addition to the Akaike (Akaike, 1974) and Bayes (Schwarz, 1978) Information Criteria, stabilization diagrams are frequently used to determine the ‘true’ model order with relatively

small errors. A stabilization diagram tries to detect and reflect the stability of selected modal variables as the model order is increased from a relatively small number to an excessively large value (De Roeck et al., 2000). The steps in constructing a stabilization diagram may be summarized in three steps:

1) A sufficiently high model order is selected and the values of the modal variables are calculated accordingly.

2) The model order is incremented and the modal variables are recalculated. The different sets of modal variables are compared and those modes that appear in differing model orders are detected. In determining this continuity, generally natural frequencies, damping ratios, and MAC (Modal Assurance Criteria) values are taken into account (Allemang, 2003).

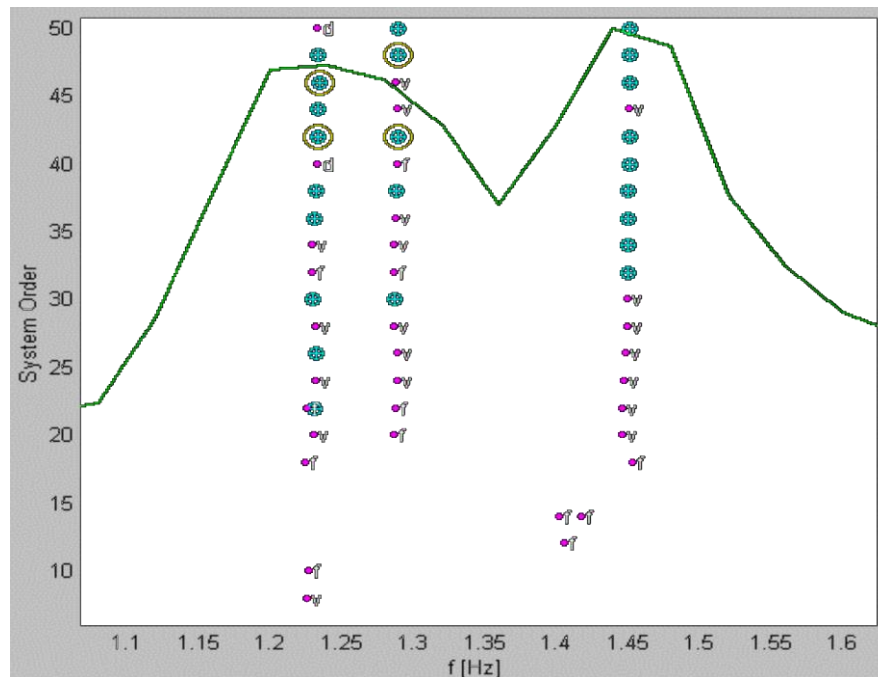


Figure 3.1. A representative PSD and stabilization diagram as given by (De Roeck et al., 2000).

3) Once a sufficient number of models are assessed, the modes that appear in most of the models are evaluated as stable and are considered to be structural modes (a representative stabilization diagram is given in Figure 3.1).

Although the stabilization diagram is a common utility, it contains many iterations and often requires user intervention. In the next section, the modal plot (Tufan et al., 2019) approach, which is a new method designed as an alternative to the stabilization diagram, is explained.

3.2. The Modal Plot

For a better understanding of the modal plot approach, it would be useful to mention the methods used for time domain system identification. In this study, Output Only Observer – Kalman filter IDentification (O3KID) (Vicario et al., 2015) followed by Eigensystem Realization Algorithm (ERA) (Juang et al., 1985) is used. This methodology allows establishing a first order dynamic model based on response (output) measurements.

The adaptation of the Observer – Kalman filter IDentification (OKID) method to environmental vibration analyzes is the result of many contributions. OKID, which requires both input force and output measurements, was initially used in the context of system diagnostics and control of spacecraft (Juang et al., 1993; Juang, 1994), and later it was applied to civil engineering structures (Luş et al., 1999, 2002). The noise used in the input and output calculations in the OKID method is reformulated in the O3KID method to accommodate the inputs, and thus it is adapted to the operational vibration analysis. The goal of the O3KID/ERA approach is to identify a first-order dynamic model for a structure based on the response time histories that can be expressed with the following equations for a discrete-time linear-time-invariant state-space model

$$x_{i+1} = Ax_i + w_i, \quad (3.1a)$$

$$y_i = Cx_i + v_i. \quad (3.1b)$$

In these expressions, sub index i is the time step, $y \in \mathbb{R}^{q \times 1}$ is the measurement vector with dimensions of the number of measurement points on the structure, x is the state vector with dimensions $n \times 1$ where n is the (initially unknown) size of the model. w and v are the input and output noise vectors (of dimensions $n \times 1$ and $q \times 1$ respectively) that are assumed to be white. The C matrix is the output matrix that maps the measured responses to the state

vector. The physical properties of the structure reside in the state transition matrix A , of dimensions $n \times n$, which dictates the time evolution of the state vector. In a mechanical system, the matrix A depends on mass, damping and rigidity distributions. For an underdamped system the eigenvalues of the matrix appear in complex conjugate pairs and they are related to the natural frequencies and damping ratios of the structure. The eigenvectors of the matrix are related to the mode-shapes of the structure through the output matrix. The model order of the system determines the dimensions of the state vector, the state transition matrix, and the output matrix, but it is unknown to begin with and must be determined from the data.

An optimal filter for the system in Equation 3.1 is

$$\hat{x}_{i+1} = A\hat{x}_i + K\varepsilon_i, \quad (3.2a)$$

$$\hat{y}_i = C\hat{x}_i, \quad (3.2b)$$

where \hat{x} and \hat{y} is the state and output estimates; K , of dimensions $n \times q$, is the observer gain, ε , of dimensions $q \times 1$, is the vector of output residuals of the Kalman Filter and can be defined as

$$\varepsilon_i = y_i - \hat{y}_i. \quad (3.3)$$

Plugging equations 3.3 and 3.2b into equation 3.2a, the observer state and output can be rewritten as to obtain an equivalent form

$$\hat{x}_{i+1} = A\hat{x}_i + Ky_i - KCx_i, \quad (3.4a)$$

$$y_i = C\hat{x}_i + \varepsilon_i, \quad (3.4b)$$

where $\bar{A} = A - KC$.

Via repeated substitution, if the current observer state, \hat{x}_i , is defined by its backward p steps state, \hat{x}_{i-p} , such that p (model order) is large enough ($p \gg n$) and \bar{A}^p becomes negligible and converges to zero, one obtains:

$$\hat{x}_i = T O_i, \quad (3.5)$$

where

$$O_i = [y_{i-1} \ y_{i-2} \ \dots \ y_{i-p}]^T, \quad (3.6a)$$

$$T = [\bar{A}^0 K \ \bar{A}^1 K \ \dots \ \bar{A}^{p-1} K]. \quad (3.6b)$$

Plugging equation 3.5 into equation 3.4b, the output is

$$y_i = C T O_i + \varepsilon_i. \quad (3.7)$$

Equation 3.7 can be written in matrix form for the time step $i = p, p + 1, \dots, l - p$ as follows:

$$Y = \Gamma V + E, \quad (3.8)$$

where

$$Y = [y_p \ y_{p+1} \ \dots \ y_{l-1}], \quad (3.9a)$$

$$\Gamma = [C\bar{A}^0 K \ C\bar{A}^1 K \ \dots \ C\bar{A}^{p-1} K], \quad (3.9b)$$

$$V = [O_p \ O_{p+1} \ \dots \ O_{l-1}], \quad (3.9c)$$

$$E = [\varepsilon_p \ \varepsilon_{p+1} \ \dots \ \varepsilon_{l-1}]. \quad (3.9d)$$

In the equation 3.8, the matrices $Y \in \mathbb{R}^{q \times (l-p)}$ and $V \in \mathbb{R}^{qp \times (l-p)}$ are known because they are constructed by known output, measurements. By having $l - p > qp$ (more equations than unknowns), the $\Gamma \in \mathbb{R}^{q \times qp}$ matrix can be estimated using Least Square solution given that the E matrix is the error term.

$$\hat{\Gamma} = YV^T(VV^T)^{-1}, \quad (3.10)$$

where $\hat{\Gamma}_i \in \mathbb{R}^{q \times q}$ is an estimate for i^{th} Markov parameter in the bar form $C\bar{A}^{i-1}K$.

To estimate the N many Markov parameters in innovation form, the following relation is used:

$$\Psi_i = \begin{cases} \hat{\Gamma}_i & i = 1, \\ \hat{\Gamma}_i + \sum_{h=1}^{i-1} \hat{\Gamma}_i \Psi_{i-h} & 1 < i \leq p, \\ \hat{\Gamma} [\Psi_{i-1} \ \Psi_{i-2} \ \dots \ \Psi_{i-p}]^T & i > p, \end{cases} \quad (3.11a)$$

$$\Psi_i = \begin{cases} \hat{\Gamma}_i + \sum_{h=1}^{i-1} \hat{\Gamma}_i \Psi_{i-h} & 1 < i \leq p, \end{cases} \quad (3.11b)$$

$$\Psi_i = \begin{cases} \hat{\Gamma} [\Psi_{i-1} \ \Psi_{i-2} \ \dots \ \Psi_{i-p}]^T & i > p, \end{cases} \quad (3.11c)$$

where $\Psi_i \in \mathbb{R}^{q \times q}$ is an estimate for i^{th} Markov parameter $CA^{i-1}K$.

The ERA method, using the Markov parameters, which are the outputs of the O3KID algorithm, aims to determine the model order of a system objectively according to the singular values of the Hankel matrix established with identified Markov parameters of the system. $\mathcal{H}_0 \in \mathbb{R}^{q^2 p \times (N-pq)q}$ and $\mathcal{H}_1 \in \mathbb{R}^{q^2 p \times (N-pq)q}$ Hankel Matrices are formed as follows

$$\mathcal{H}_r = \begin{bmatrix} CA^r K & CA^{r+1} K & \dots & CA^{N-pq-1+r} K \\ CA^{r+1} K & CA^{r+2} K & \dots & CA^{N-qp+r} K \\ \dots & \dots & \dots & \dots \\ CA^{qp+r-1} K & CA^{qp+r} K & \dots & CA^{N-2+r} K \end{bmatrix}. \quad (3.12)$$

According to the theory, a Hankel matrix of Markov parameters is the multiplication of the observability matrix, \mathbb{O} , and the controllability matrix, \mathbb{C} :

$$\mathcal{H}_0 = \mathbb{O} \mathbb{C}, \quad (3.13)$$

where

$$\mathbb{O} = \begin{bmatrix} C \\ CA \\ \dots \\ CA^{qp-1} \end{bmatrix}, \quad (3.14a)$$

$$\mathbb{C} = [K \quad AK \quad A^{N-pq-1}K]. \quad (3.14b)$$

From the control theory since $qp > n$ and $N - qp > n$, both \mathbb{O} , \mathbb{C} and \mathcal{H}_0 have rank n . Singular Values of \mathcal{H}_0 calculated by Singular Value Decomposition analysis is also n . Accordingly, a sudden decrease in the singular values of Hankel matrix indicates the real order of the system such that theoretically, the Hankel matrix should have as many non-zero singular values as the true order of the system with all other singular values being zero.

Although the determination of the model order is theoretically a very important stage, in practice there are no definite divergences due to various reasons, and the singular values generally show a close distribution. Therefore, for the case $qp < N - qp$ in Modal Plot method qp many singular values are calculated as follows:

$$\mathcal{H}_0 = U_1 [S_1 \quad 0] \begin{bmatrix} V_1^T \\ V_2^T \end{bmatrix}, \quad (3.15)$$

where $S_1 \in \mathbb{R}^{qp \times qp}$ are singular values, and U_1 and V_1^T comprise the left and the right singular vectors. The following relation between observability, controllability matrices and singular values, vectors are assumed to be exist:

$$\mathbb{O} = U_1 S_1^{1/2}, \quad (3.16a)$$

$$\mathbb{C} = S_1^{1/2} V_1^T. \quad (3.16b)$$

With this choice, the state transition, A , and output matrix, C , can be estimated as follows:

$$C = \text{first } n \text{ rows of } \mathbb{O}, \quad (3.17a)$$

$$A = S_1^{-1/2} U_1^T \mathcal{H}_1 V_1 S_1^{-1/2}. \quad (3.17b)$$

What is proposed in this chapter is another auxiliary technique called the modal plot. A modal plot, a representative of which is given in Figure 3.2, is a diagram that reveals the interaction of all estimated frequencies and corresponding mode shapes of high order time domain models. When the term modal is used, there would be an expectation to relate it with three modal parameters, which are the natural frequencies, the mode shapes, and the modal damping ratios. The modal plot comprises the first two and how modal damping ratios affect a modal plot will be discussed in Section 3.5. Moreover, the definition of modal zones of computational estimates will be also one of the issues to be dealt with in Section 3.4 for a discrete system and in Section 4.4 for a continuous system.

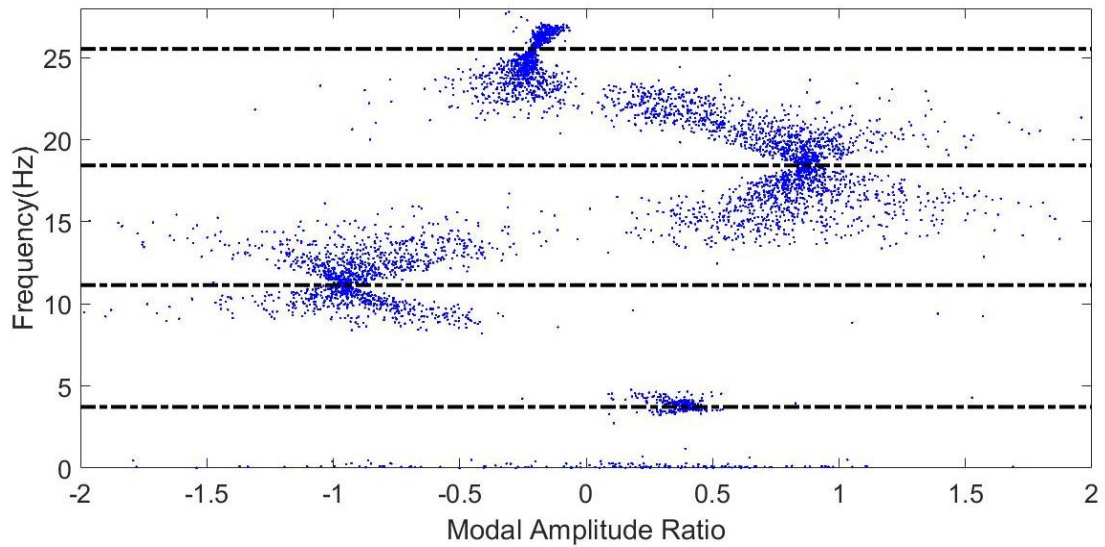


Figure 3.2. A representative modal plot.

The number of singular values included is maximized as much as possible in the ERA step to generate the state space model with a maximum dimension in order to estimate as many modal parameters as possible and a further elimination step is not required in order to draw the modal plot.

The scaling of the mode shapes is done by setting the amplitude of the mode shape to 1 (one) at the reference node. Once all the modal parameters are extracted from all the systems identified using all the overlapping data segments, each frequency and mode modal amplitude ratio pair is plotted for each node to construct the modal plots. The modal plot is a graphical tool which will be used in latter sections to detect the existence of damage in a continuous system, is next converted to the count plots to identify the real modes.

3.3. The Count Plot

The count plot is a clustering approach that allows simultaneous determination of the true natural frequencies and the corresponding mode shapes of a system. The premise which the approach is based on is that the modal variables calculated by the system identification methods contain errors, even if in small amounts, but when different data sets are used, the scattering in the “actual” modes will be smaller compared to the “computational” modes.

For a particular system, when different models are set up using the data collected within a time period that the system properties are assumed not to change, the exact same values for modal variables will not be obtained from the identified systems. It can, however, be said that the distribution of the modal values (within certain limits) will in fact to be related with the same model supposedly corresponding to real structure. Based on this clustering approach, the number of the modal variable estimates lying within certain limits are counted and are plotted based on the frequency values to obtain the count plot. The frequencies that correspond to the peaks in the count plots are expected to correspond to the actual frequencies of true structural modes. Since both frequencies and mode-shapes are used in clustering, the average of the frequency and mode-shape prediction sets corresponding to the peaks can be calculated automatically. Thus, the “real” natural-frequencies and mode-shapes of the system (which will be referred to here as the ‘modal point’) are estimated. Since the modal variables are calculated according to the peaks, a count plot, which is directly processed in the time domain, is quite similar to the PSDs of the response signals calculated via the Fourier transforms. The count plot approach proposed here will be used to estimate the modal variables to be employed in the case studies to be discussed in Sections 4.1-4.3.

3.4. A Case Study

This part is related to system identification of a discrete system, and the aim of this case study is to demonstrate how to estimate modal parameters using the modal plot.

The numerical model, with properties provided in Table 3.1, is a one dimensional, 15 DOF spring-mass chain system with one end fixed to a stationary point as shown in Figure 3.3. During the simulations, the following guidelines are followed:

- i. System is excited by a white noise input applied at 15th DOF (15th point mass).
- ii. System is linear, time invariant, and undamped.
- iii. There is neither measurement nor plant noise.

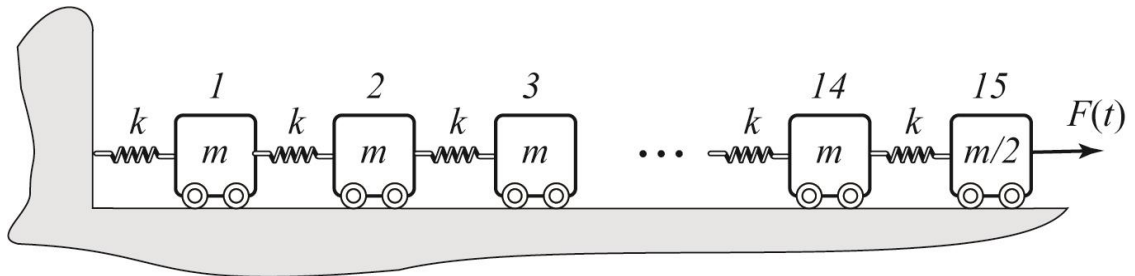


Figure 3.3. The mass-spring 'cantilever' system used.

Table 3.1. Numerical Analysis Specifications

# of DOFs	15
End Conditions	Fixed-Free
Spring Stiffness [k]	2.27E8 N/m
1st-14th DOF mass [m]	4530 kg
15th DOF mass	2265 kg
Damping	No
Input DOF	15 th DOF
Input Type	Ambient force

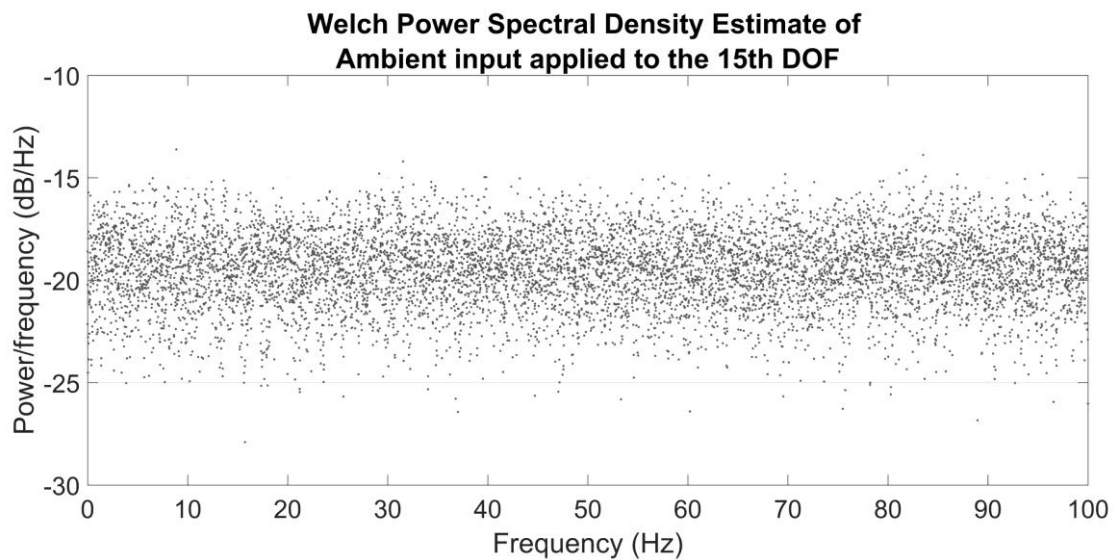


Figure 3.4. Power spectral density estimate of the ambient input applied on the 15th DOF.

Power spectral density of the input time history used in the analyses are shown in Figure 3.4. The white noise assumption is valid for the input used in the analysis.

The power spectral density function of the responses obtained on the first, 5th, 9th, and 13th DOFs are shown in Figure 3.5. Peaks are clear, well separated and correspond to the actual frequencies of the system.

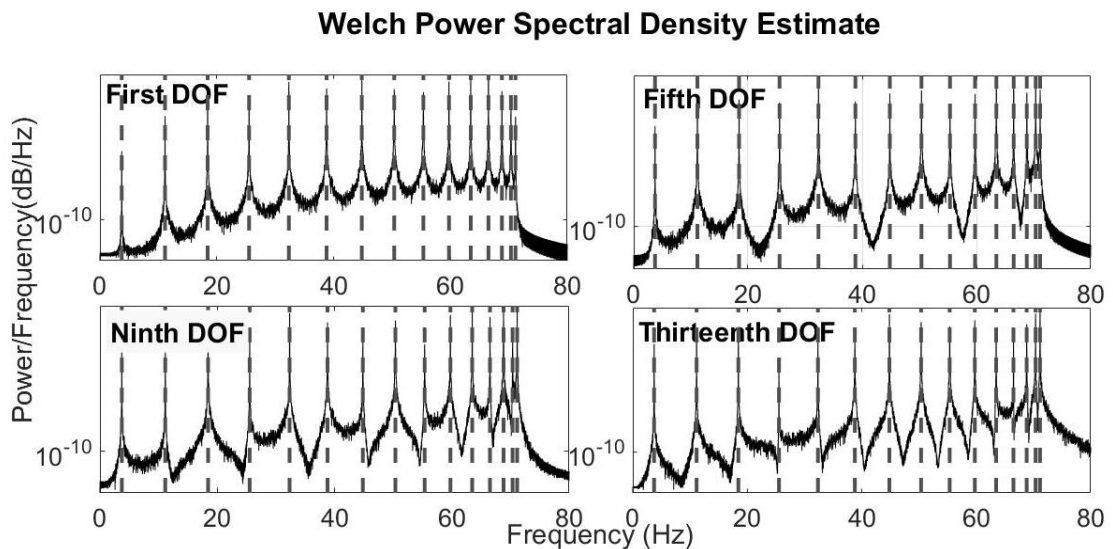


Figure 3.5. Power spectral density estimates for the 1st, 5th, 9th, and 13th DOFs.

The procedure followed to sketch the modal plots is as follows:

In each analysis, four measurement locations are considered. The 15th DOF is taken as a reference DOF and the remaining 14 DOFs are analyzed in five steps such that in the first step, the 1st, 2nd, 3rd, and the 15th DOFs are analyzed, and in the last step the first, 13th, 14th, and the 15th DOFs are analyzed. Therefore, the first DOF is analyzed twice.

In each step, the response time histories are divided into segments with 80% overlap.

O3KID: A relatively high order is chosen for the observer model which is initially constructed as a regressive model (in this example model order is 300, which is half of the number of observer Markov parameters in the O3KID analysis) and more than 5000 Markov Parameters are calculated.

ERA: The Markov Parameters are used in a square Hankel matrix which has dimensions greater than 4000 by 4000. The system order for the realization is set to 4000, and the natural frequency and mode shapes of the system are calculated for the realized A and C matrices.

When all computation process is complete, the frequency – mode shape component pairs are plotted as in Figure 3.6, and these plots are what are coined here as ‘modal plots’

The modal plots for the first DOF has around 20 000 and the other DOFs have and 10 000 frequency – mode shape component pair estimates, between 0-40 Hz.

In Figure 3.6, the actual natural frequencies and mode shape amplitudes of the system are indicated as circles. These actual reference values are referred to as ‘modal points’. All estimates which are not close to the modal points are candidates for computational modes. Based upon this classification, a ‘modal zone’ is defined as a region containing a modal point and a ‘curve’ of the surrounding computational modes, as shown in Figure 3.6.

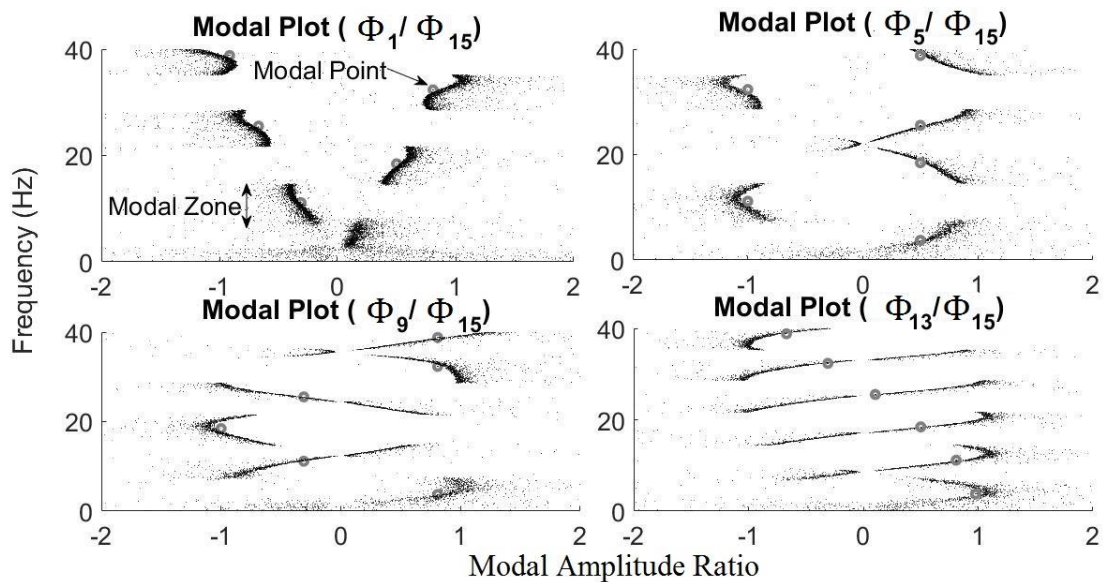


Figure 3.6. Modal plots for various DOFs, including actual modal points (circles) and modal zones.

For identification purposes, these modal plots are converted to count plots as follows:

- (1) [Optional] Order all estimates according to increasing values of frequencies.
- (2) Define a tolerance limit for the mode shape and the frequency components as in Figure 3.7.
- (3) For an estimate, count estimates (other than itself) within the tolerance limit.
- (4) Repeat (3) for all estimated points.
- (5) Plot counts versus frequencies for all estimates as in Figure 3.8. This plot is referred to as the “*count plot*”.

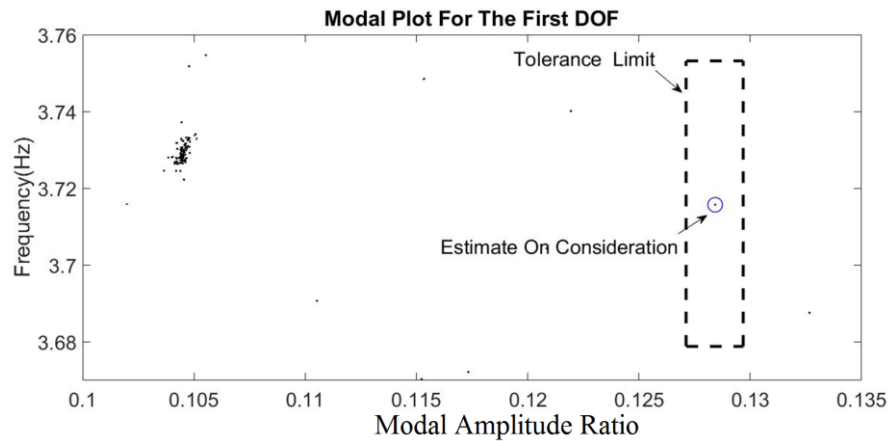


Figure 3.7. Modal plot tolerance limits.

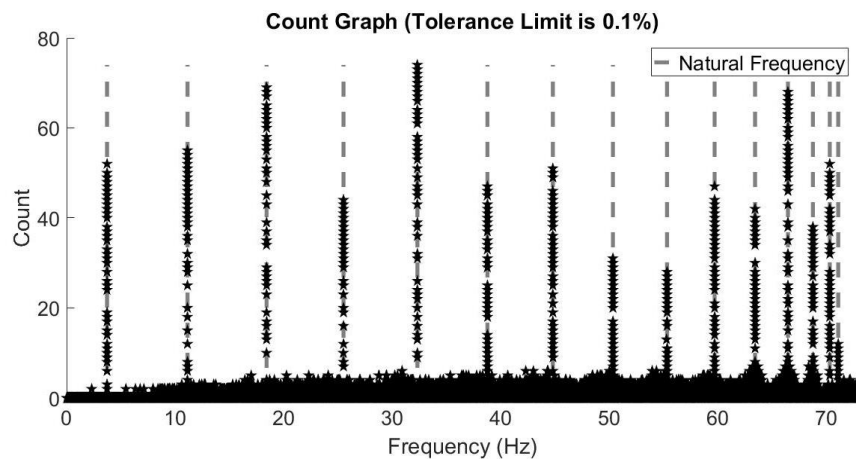


Figure 3.8. Count plot for 0.1% tolerance limit.

The actual natural frequencies of the system and the count plot peaks are compatible with each other as can be seen in Figure 3.8. The ranges within which the identified frequencies are contained are defined according to Figure 3.8. The estimates with maximum counts are selected automatically as the candidates for modal points depending on the ranges defined. The mode shape values are calculated as the average value of the accumulation of points which contains one of the peaks of the count plots as shown in Figure 3.9.

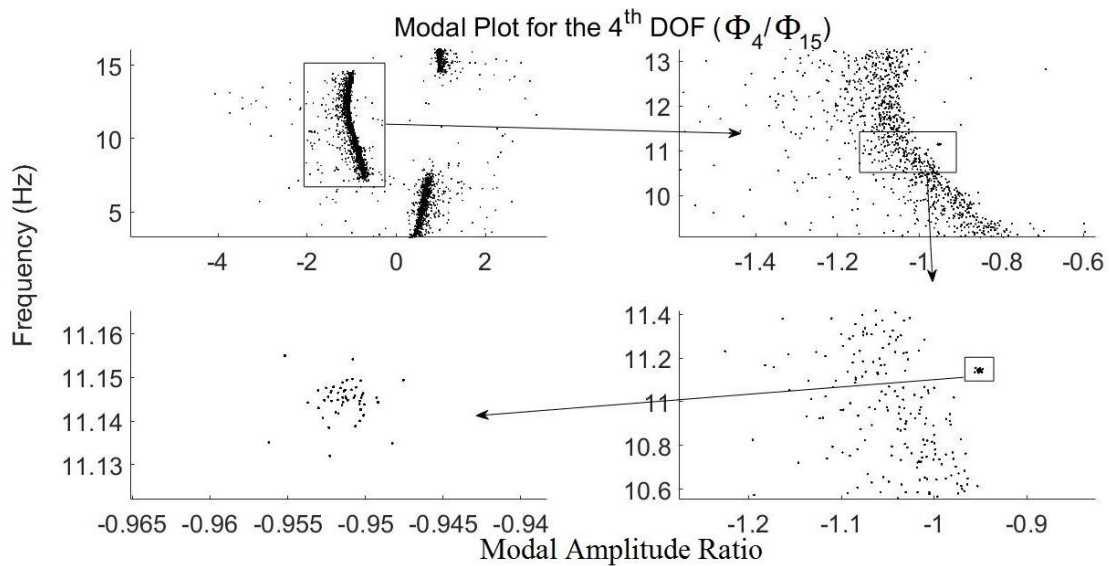


Figure 3.9. Accumulation of estimates in Modal Parameters for DOF 4.

Figure 3.10 shows the comparison between the mode shapes of the system and estimated mode shapes for the first four modes. A very close match is attained for each mode and each DOF. The results show that maximum relative errors in the mode shape components in percentage are 0.055, 0.067, 0.082, and 0.147 for the first four modes, respectively. Therefore, for the particular example considered, the count plots provide satisfactorily accurate results.

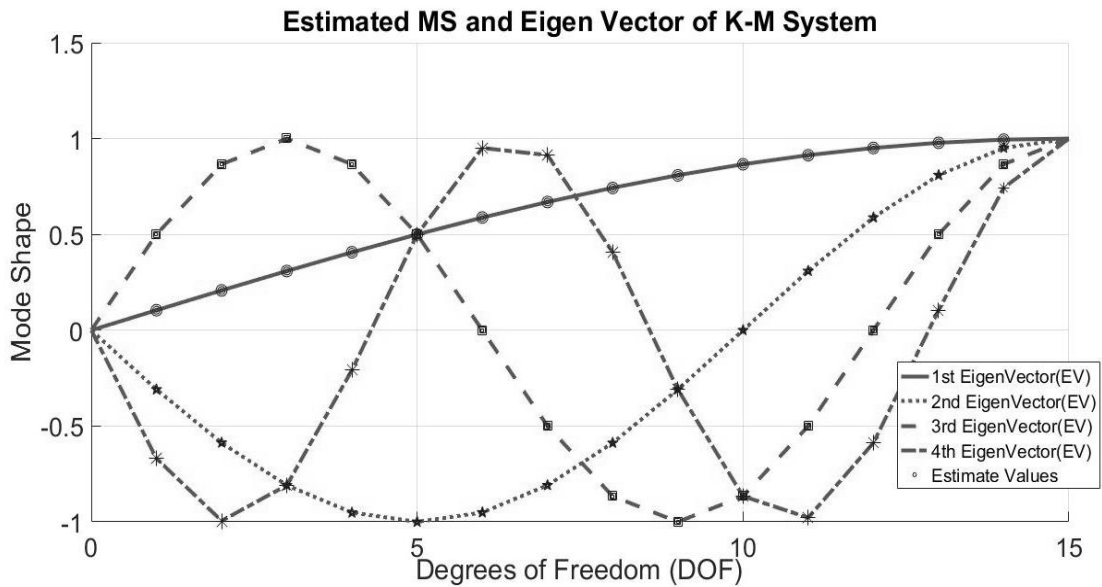


Figure 3.10. The first 4 mode shapes: Lines: exact mode shapes calculated via the eigenvalue problem; markers: estimated values using the count plot.

It should be noted that if the tolerance limit is chosen as a relatively a high value, as for example 1% for each modal parameter then counts of computational modes may also be included in the assembly of real modal parameters as schematically shown in Figure 3.11. It therefore stands to reason to define the tolerance limit as an acceptably low percentage or value.

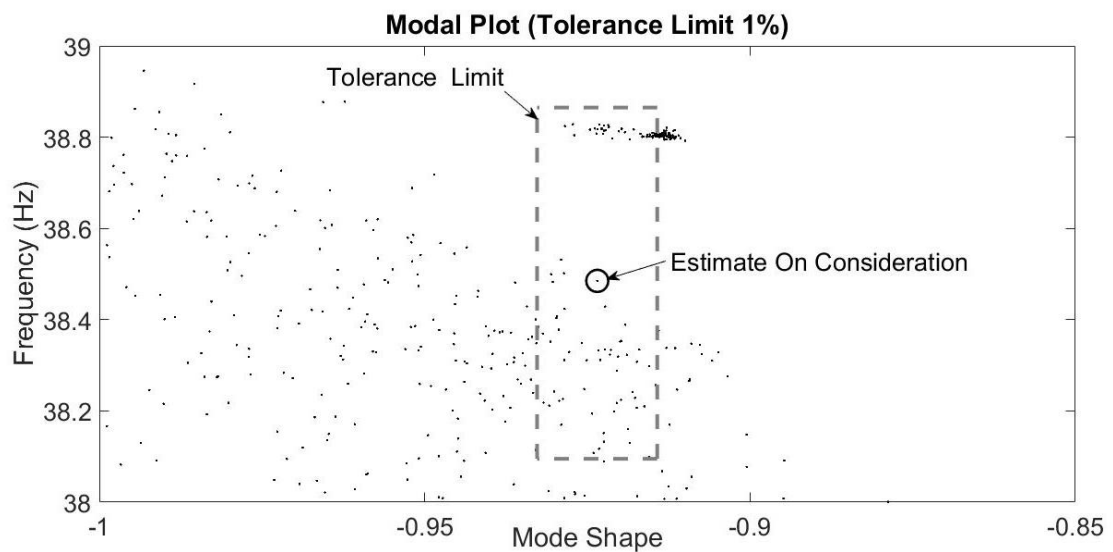


Figure 3.11. Modal plot: 1% tolerance limit.

In order to investigate the impact of the user defined tolerance limit on the identified modal parameters, the modal points identified for the 15 DOF system discussed above are clustered with various tolerance limits. To simplify the discussion, tolerance limits for both mode shapes and natural frequencies are selected to be same and are defined in terms of percentage points. Due to the scaling of the mode shapes, the maximum modal amplitude is 1 (one). In the analysis, the tolerance limits around each modal point are set as $\pm 0.1\%$, $\pm 1\%$ and $\pm 5\%$ of the frequency value (corresponding to the vertical axes of the modal plots) and of 1 (corresponding to the horizontal axes of the modal plots). Figure 3.12-3.15 show the count plots obtained for the 1st, 4th, 7th and the 14th DOFs using these three tolerance limits. It is noteworthy that in all cases the natural frequencies are correctly identified, i.e. the cluster peaks coincide with the actual values of the frequencies that are also marked on the figures. The ‘noise’ in the results, however, indicated by the variations in the scatter of the non-peak clusters, tends to increase with increasing tolerance limits. This is to be expected as $\pm 5\%$ is a significant deviation. In any case, the consistency of the identified frequencies is an encouraging indicator of the robustness of the approach with regards to user defined tolerance limits.

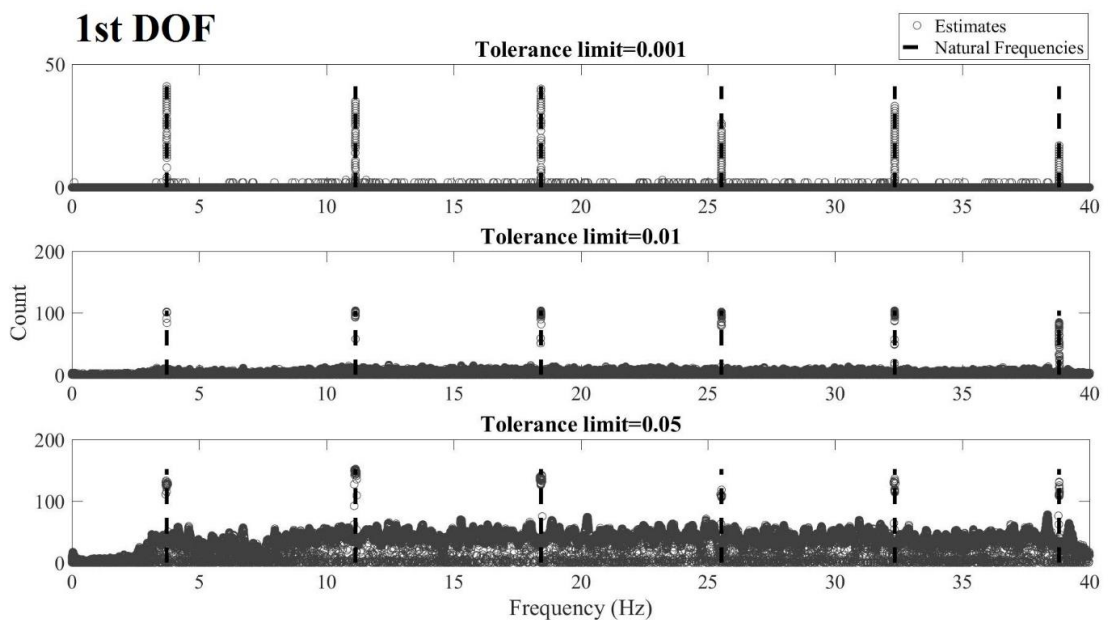


Figure 3.12. Count Plot for different tolerance limits for 1st DOF.

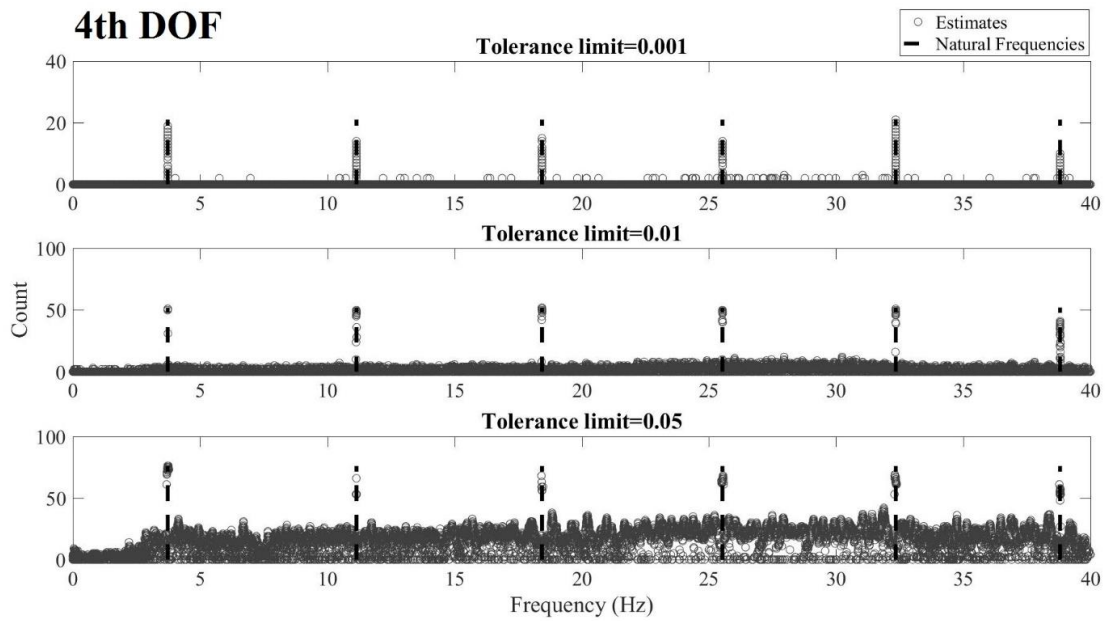


Figure 3.13. Count Plot for different tolerance limits for 4th DOF.

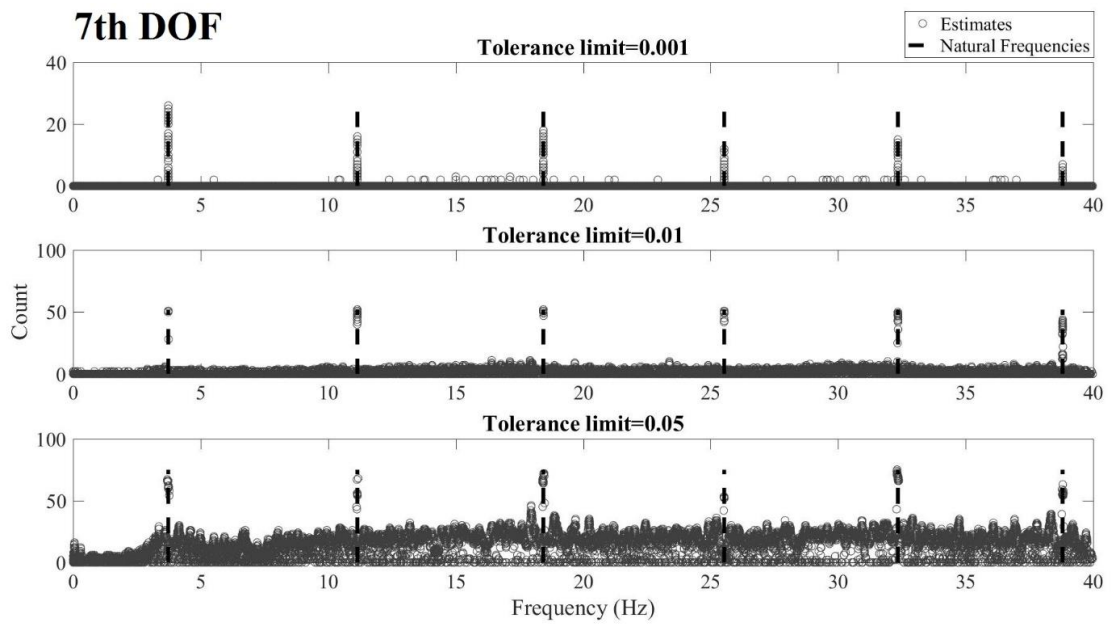


Figure 3.14. Count Plot for different tolerance limits for 7th DOF.

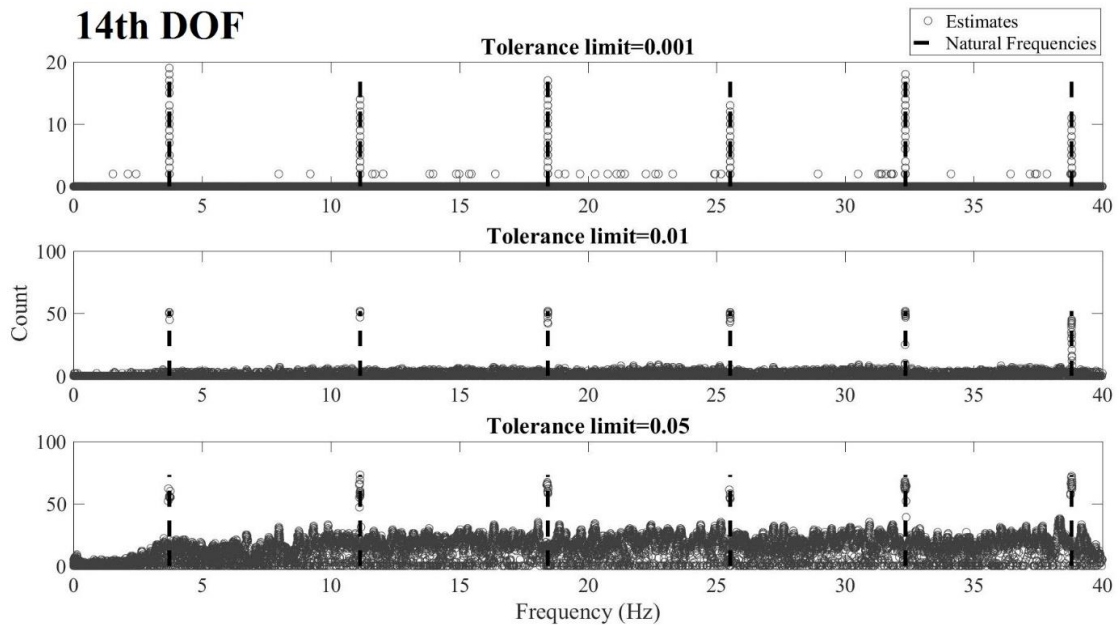


Figure 3.15. Count Plot for different tolerance limits for 14th DOF.

The minimum and maximum errors corresponding to different tolerance limits are given in Figures 3.16-3.18. The errors in the estimates of both the natural frequencies and the mode shapes are very low and attest to the robustness of the proposed count plot approach. The only relatively large errors in the mode shapes appear in the $\pm 5\%$ case. It should be emphasized, however, that such a tolerance limit is excessively high and included in this discussion only as a representative upper limit.

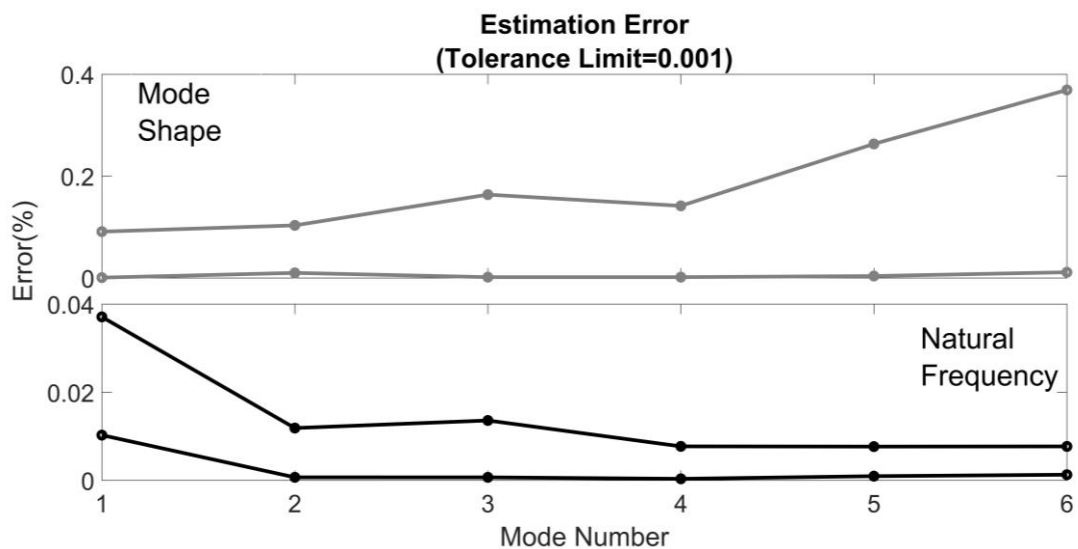


Figure 3.16. Error limits in modal parameters for tolerance limit 0.001.

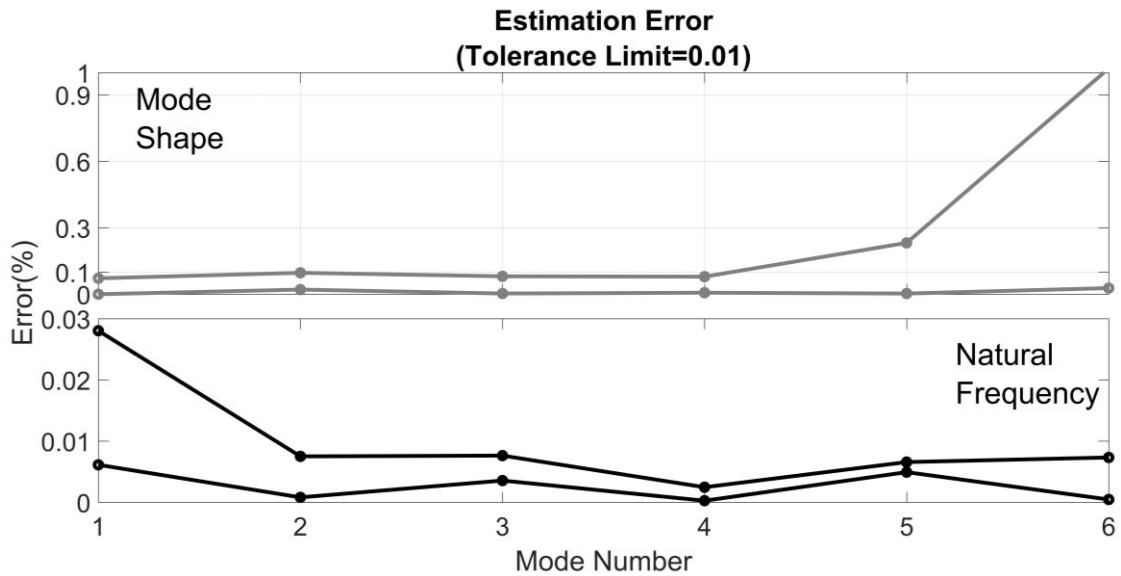


Figure 3.17. Error limits in modal parameters for tolerance limit 0.01.

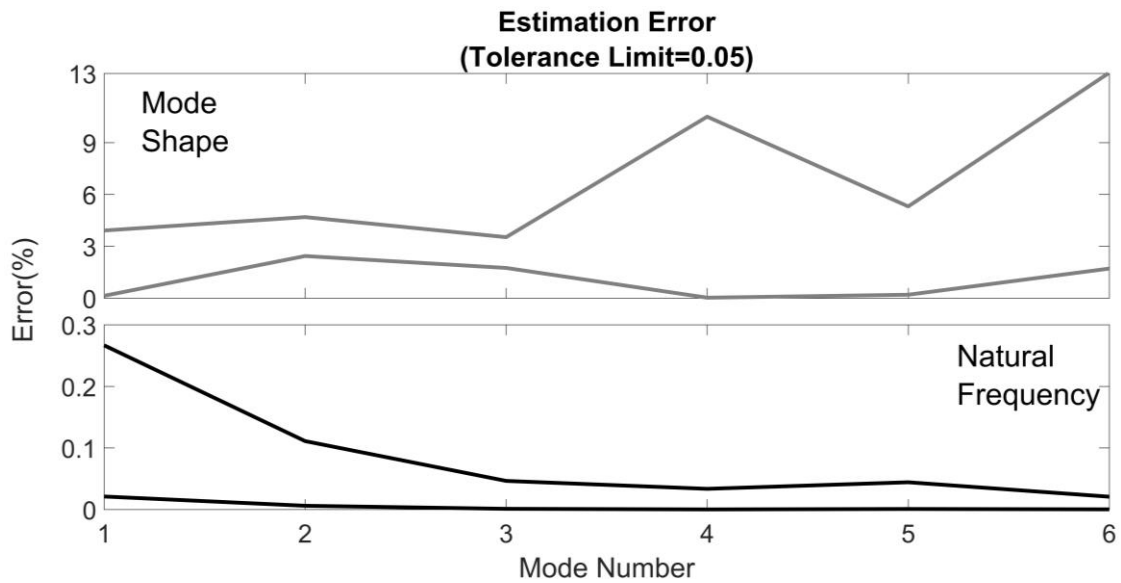


Figure 3.18. Error limits in modal parameters for tolerance limit 0.05.

As an alternative to count plots, histogram plots may also be used for frequency estimates. In Figure 3.19 the peaks appear at the natural frequency values in the histogram plot. The counts in the histogram are higher than that in the count plot at the frequency bands containing the actual values of natural frequencies. However, the error in histogram plot is much higher than in the count plots, as evidenced by the high counts in the off peaks.

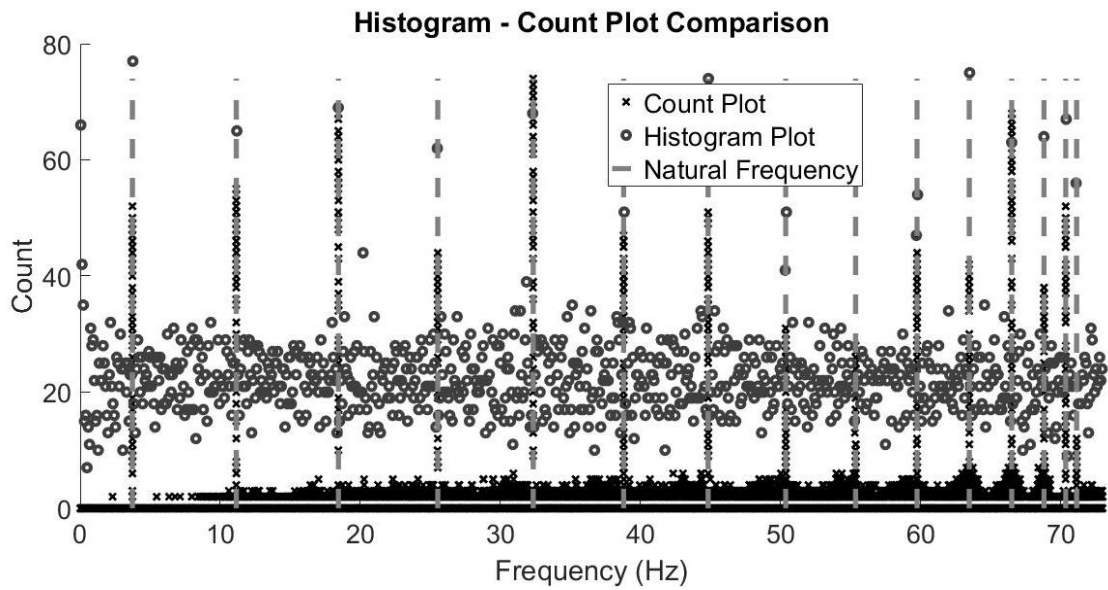


Figure 3.19. Histogram using frequency estimates and its comparison with the count plot.

3.5. Effect of Damping Ratio on Modal Plot and Count Plot

Count plot is an efficient tool for modal parameter estimation under no damping and no noise case. However, as the noise and in damping ratio increase, the accumulation of points around actual modal points may not appear in the modal plots, as hinted by Figure 3.20.

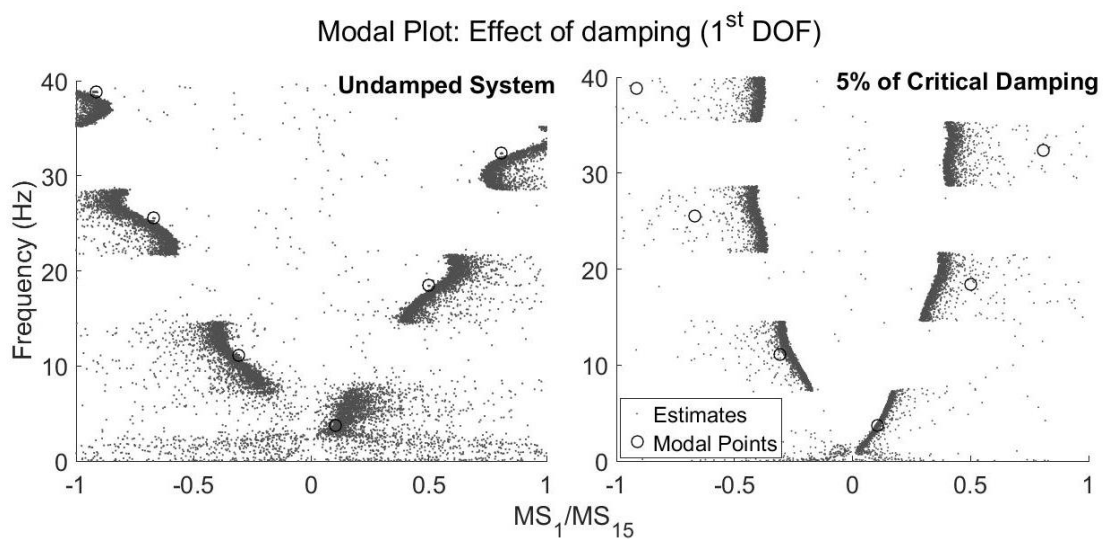


Figure 3.20. Change in a modal plot for increasing damping for the 1st DOF.

To investigate the damping effect on the count plot, four critical damping ratios (CDR) are considered in this section which are 0.2%, 1%, 5%, and 10%. The ten percent damping ratio is selected deliberately since it may be close to an upper bound for damping ratios typically encountered in civil engineering structures.

Amongst modal parameters, mode shapes are the most sensitive to damping. The undamped eigenvalue problems for typical mechanical systems yield “real modes”, such that the mode shape values at the nodes have phase differences of either 0 or π . Physically, a real mode shape corresponds to a modal vibration wherein the maximum (minimum) amplitudes are reached simultaneously at all nodes, as well as simultaneous attainment of the equilibrium (‘zero’) configuration. A damped eigenvalue problem, however, yields “complex modes” unless the damping is classical. In a complex mode, the mode shape values at the nodes may generally have phase differences other than 0 or π . Physically, this would mean that the nodes reach their relative maxima/minima at different times, such that, for example for a phase difference of $\pi/2$ between two nodes, one node would be passing through its equilibrium configuration while the other is already at its peak. Naturally this brings about various issues regarding the visualization and interpretation of a ‘mode shape’. Noise and modelling errors generally tend to scramble the phase information such that, even though the system may be classically damped, the phase differences between the components of identified modes do not comply with what would be expected of real modes. Therefore one issue that comes to the forefront when damping is present is the artificial coupling of the modes, i.e. the deviations of the mode shapes from ‘real’ modes, that are induced by accumulated errors in the identified models. In the example considered herein, for systems with 0.2% and 1% damping ratios, mode shape estimates, which turn out to be complex valued, are directly converted to real numbers using the following equations:

$$\beta_{j,i} = \cos^{-1} \frac{Re(\Phi_{j,i})}{|\Phi_{j,i}|} \quad (3.18)$$

$$\Phi_{j,i} = \begin{cases} |\Phi_{j,i}| & \text{if } -\pi/2 < \beta_{j,i} < \pi/2 \\ -|\Phi_{j,i}| & \text{Otherwise} \end{cases} \quad (3.19a)$$

$$(3.20b)$$

where $\Phi_{j,i}$ is the value of the j th mode shape on the i th node, $\beta_{j,i}$ is phase angle of that same mode shape value, $|\cdot|$ is the magnitude operator and $Re(\cdot)$ is the real part of a complex number. This approach is quite crude in that it maps a wide range of phase angles to either 0 or π , but it may be expected to yield reasonably good answers when the identified modes are close to real.

Since the phase angle of mode shape estimates for the systems with critical damping ratio less than 1% is close to 0° and 180° , the real parts of the mode shapes and the amplitudes calculated via Equations (3.1) and (3.2) are very close. The estimates of mode shapes identified from response data are close to the actual mode shapes calculated using the mass and stiffness matrices, as shown in Figures 3.21 and 3.22.

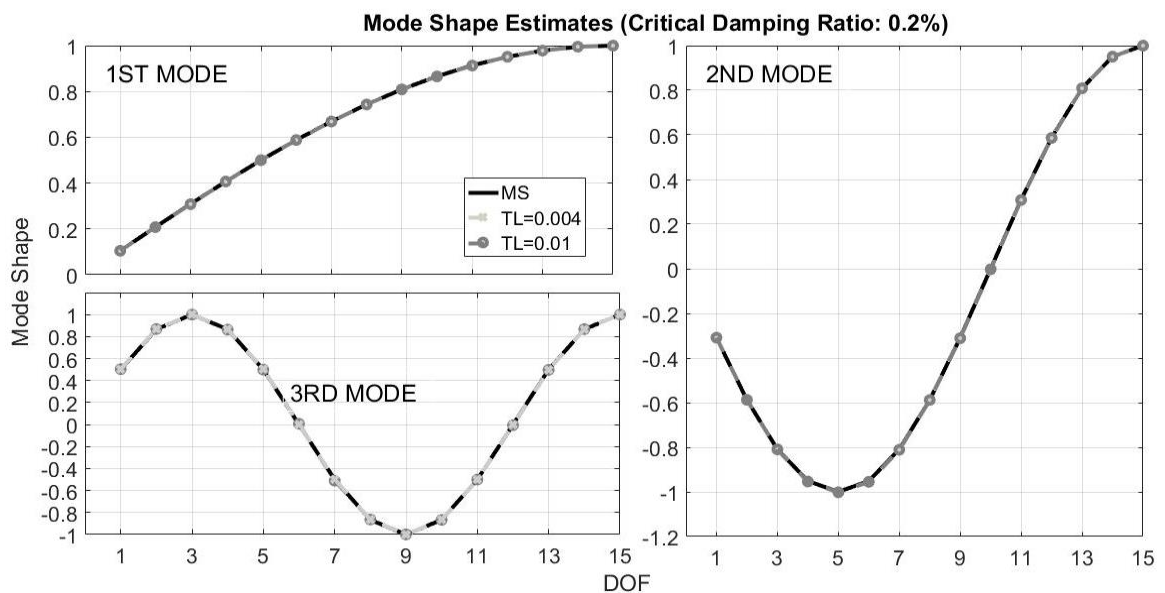


Figure 3.21. Mode shape estimates for the tolerance limit 0.004 and 0.01 for CDR 0.2%.

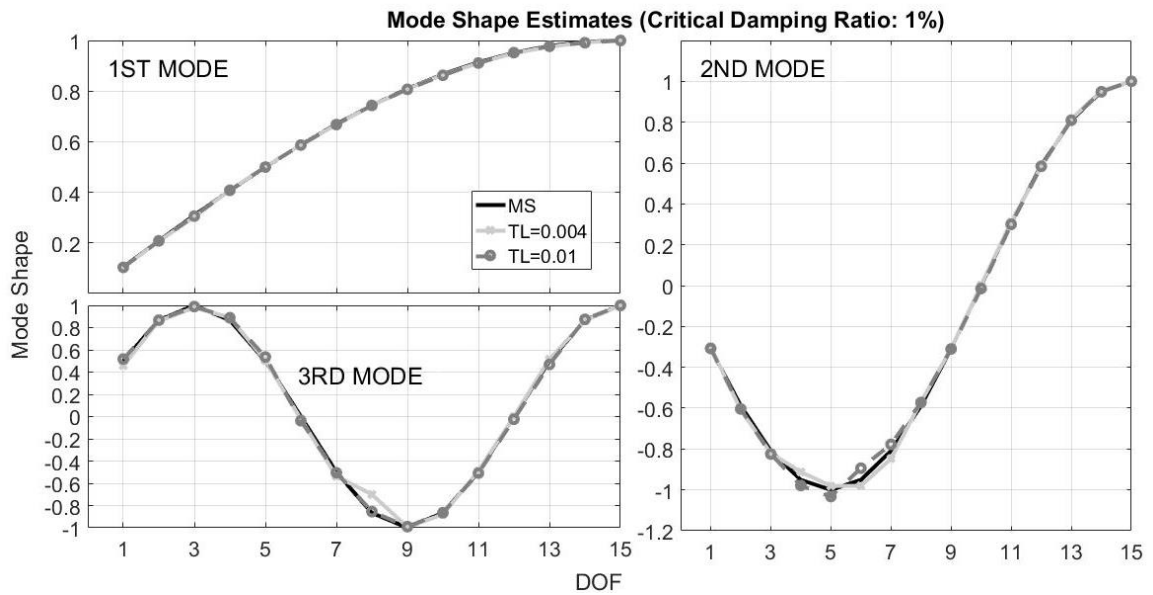


Figure 3.22. Mode shape estimates for the tolerance limit 0.004 and 0.01 for CDR 1%.

However, for the systems with CDR 5% or more, the variations in the phase angles of the mode shape estimates become more pronounced. Therefore, the phase differences between the nodes lead to bigger errors. To address this problem, and assuming that the underlying system is classically damped so that the more a mode shape deviates from a real mode the more likely it is to belong to an artificial, computational mode, estimates with phase angle deviations higher than a certain threshold are not taken into account, and the modal plot is constructed with the remaining estimates. In such a case, one would have to determine two thresholds, one pertaining to the phase angle, and the other pertaining to the tolerance limit used in constructing the count plots. To reduce the problem from two variables to one variable, the tolerance limit is varied in a range and the average of the mode shape estimates identified via all the different tolerance limits is taken as the estimate for the given phase angle. In the particular example considered, for CDRs 5% and 10%, the tolerance limit is varied from 0.004 to 0.08 with a step size of 0.002, and the threshold values for the phase angles are selected as $\pi/4$ and $\pi/10$. The significance of the threshold values for the phase angles is as follows: For a given threshold value δ , i. if the phase angle remains within $0 \pm \delta$, it is considered as 0; ii. if the phase angle remains within $\pi \pm \delta$, it is considered as π ; iii. if the phase angle lays outside these regions, the mode shape is discarded. The identified mode shapes are sketched in Figures 3.24 and 3.25

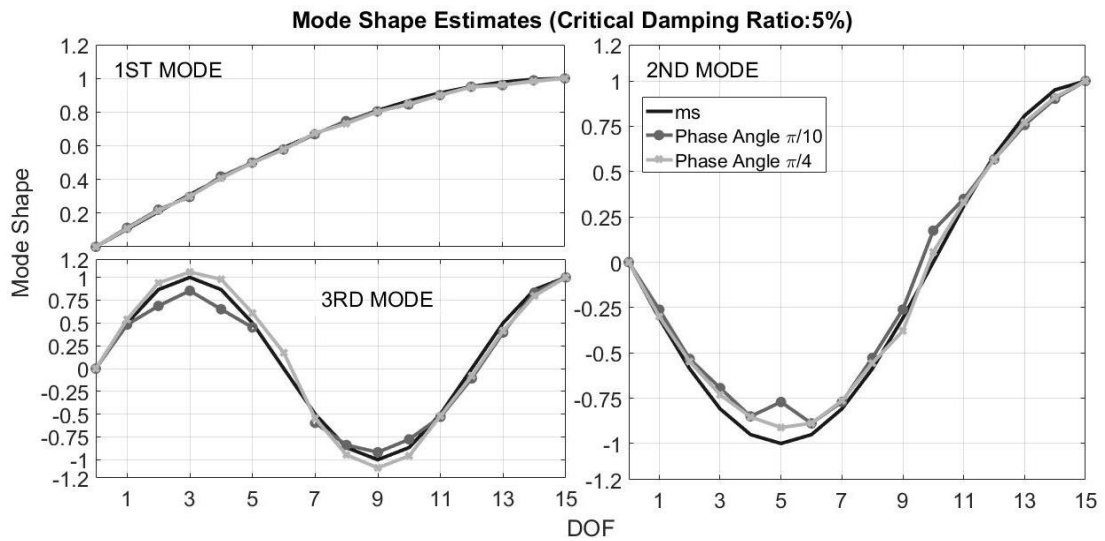


Figure 3.23. Mode shape estimates identified for the system with CDR 5% using threshold phase angle values of $\pi/4$ and $\pi/10$.

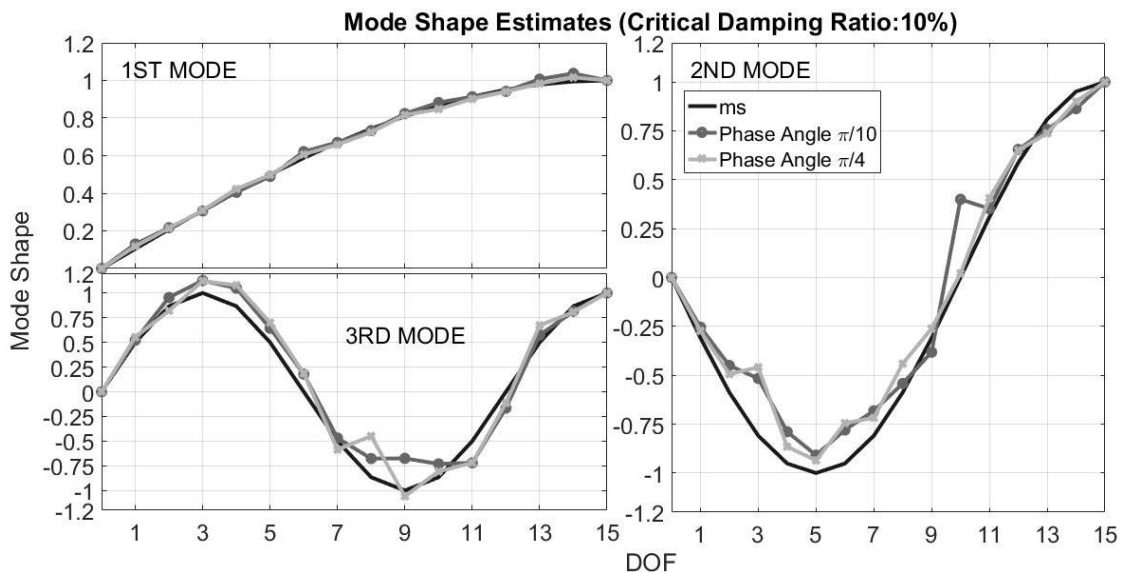


Figure 3.24. Mode shape estimates identified for the system with CDR 10% using threshold phase angle values of $\pi/4$ and $\pi/10$.

To investigate whether a higher model order would lead to improved results as has been reported by various previous studies discussing OKID/ERA, the analyses are repeated with a higher order for the identified state space model; specifically, the model order is increased from 400 to 1000. Figures 3.25 and 3.26 show that the results improve slightly but not necessarily significantly to justify working with much increased model orders.

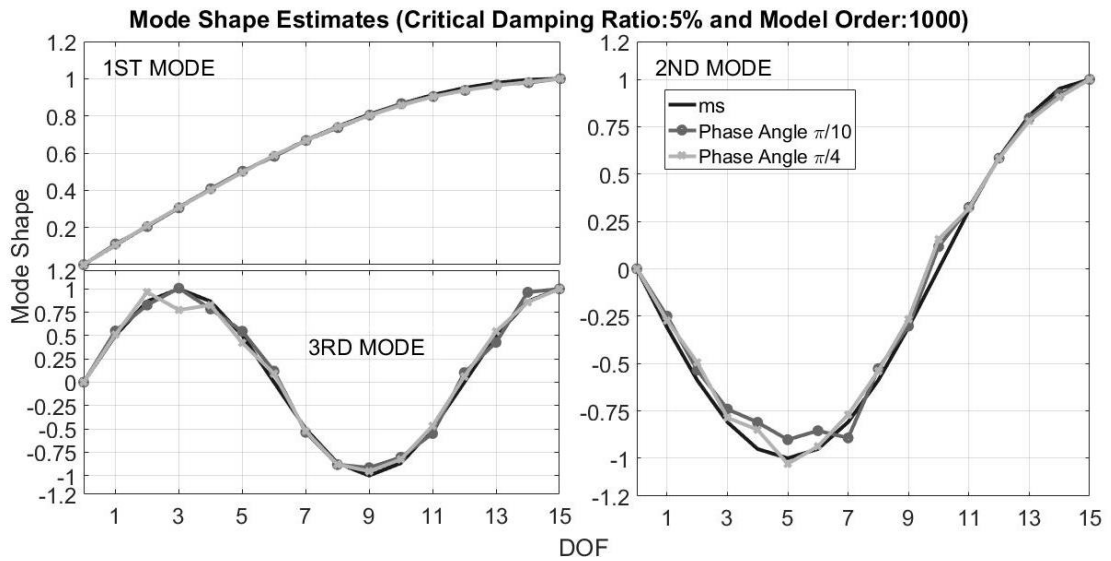


Figure 3.25. Mode shape estimates identified for the system with CDR 5% using higher model orders and threshold phase angle values of $\pi/4$ and $\pi/10$.

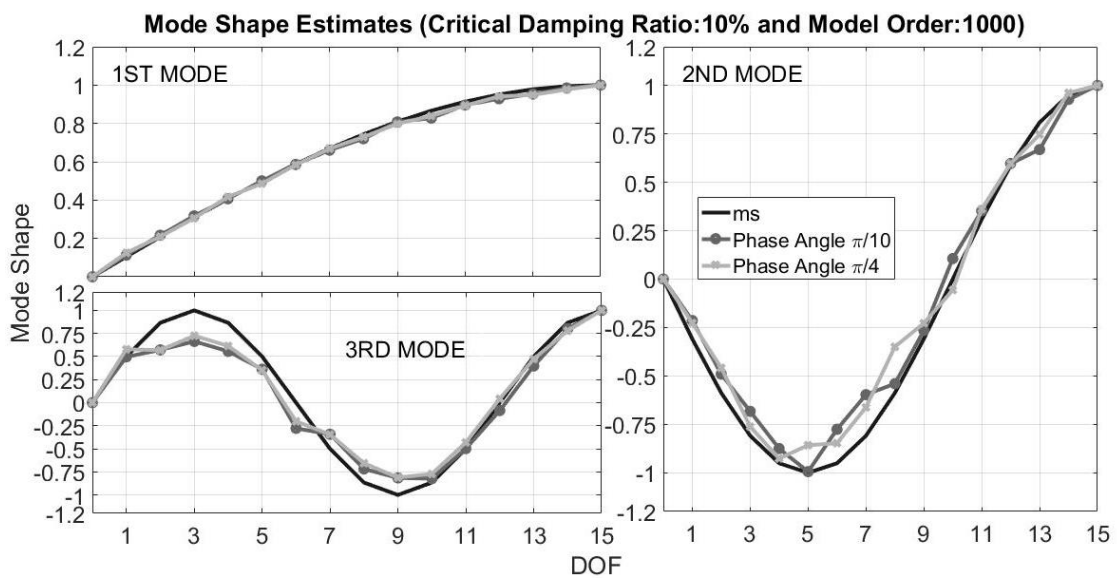


Figure 3.26. Mode shape estimates identified for the system with CDR 10% using higher model orders and threshold phase angle values of $\pi/4$ and $\pi/10$.

4. NUMERICAL AND EXPERIMENTAL CASE STUDIES

The aim of the analyses undertaken in this chapter is to discuss in detail the performance of the methods proposed in Chapters 2 and 3. In the first three sections, modal parameters are estimated from response data by utilization of count plots, and location of damage is estimated successfully by the proposed damage indicators. The first and third sections are ‘blind tests’ in the sense that only the number of DOFs of the mass-spring system, the type of damage (reduction in spring stiffness) and one-minute response measurements from each DOF is provided beforehand. Last two sections are related to estimation of the existence and location of damage inspired by the observations on experimental data.

4.1. Fault Identification with Noise-Free Ambient Vibration Data:

Exact calculation of the modal variables is not possible in practice as they would have to be estimated from field tests. To address this issue, application of modal analysis to simulated operational data is investigated. Acceleration data obtained from a 10-DOF, damped spring-mass chain fixed-free system is examined in this section in order to observe the effects of the error in the estimation of modal parameters on the proposed indicator. For numerical analyses, accelerations are simulated at all DOFs under the white noise type forces that resemble ambient inputs. Response histories are calculated for a period of one minute with 200 Hz for the undamaged condition and two different damage conditions. The data was produced and provided with no additional knowledge. After the analyses were concluded it was later confirmed that the first damage case corresponds to a 20% reduction in the stiffness of the 8th spring, and the second damage case corresponds to 20% stiffness reductions in the 6th and the 8th springs. The purpose of this study is to estimate the system parameters with the use of the count plots and to identify the location of damage with the proposed damage indicator for noise-free data.

The initial step undertaken upon receipt of data is a preliminary investigation regarding the quality of the data: there is no trend in the signal, and the average of the accelerations at each measurement channel is zero. Secondly, the PSD of the data is examined: there are 10 separate peaks between 0-8 Hz as shown in Figure 4.1. Table 4.1 presents the possible natural-frequency ranges to be used in the count plot, the range is selected so that it covers undamaged and two damaged conditions.

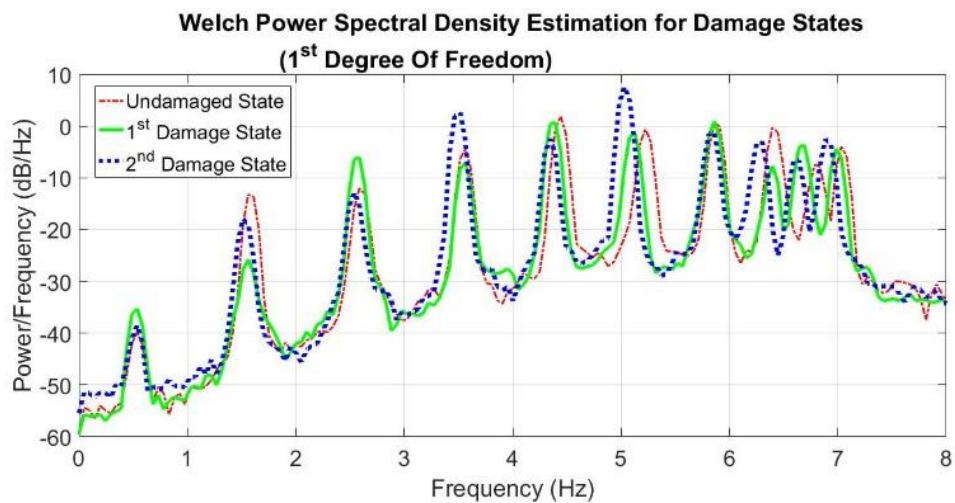


Figure 4.1. PSD estimates for the three data sets obtained from acceleration data ‘measured’ at the first DOF.

The first two steps described above provide preliminary information about the data and the system. In the third step, first-order dynamic models are established with O3KID and ERA methods. The number of observers is set to 800 in O3KID analysis. In the analysis every DOF is analyzed separately with the (reference) 10th DOF. The data is divided into 25.35-second long segments with overlapping 2.54 second data. For each data segment, a total of 390 frequencies between 0-100 Hz and corresponding mode shapes are calculated via the identified state space models and the modal plot is constructed. According to ± 0.04 tolerance limit for the modal variables, the counts for each estimate are calculated and the count plots shown in Figure 4.2 are obtained.

Table 4.1. Estimated frequency ranges for the first three modes:

Mode Number	Lower Bound (Hz)	Upper Bound (Hz)
1	0.4	0.7
2	1	2
3	2	3
4	3	4
5	4	5
6	5	5.5
7	5.5	6
8	6	6.5
9	6.5	6.9
10	6.9	7.5

Table 4.2. The natural frequencies determined by O3KID / ERA and the count plots

Mod	Undamaged System			Damaged Case 1			Damage Case 2		
	Min.	Mean	Max.	Min.	Mean	Max.	Min.	Mean	Max.
1	0.528	0.529	0.529	0.527	0.528	0.529	0.517	0.518	0.518
2	1.576	1.582	1.594	1.534	1.544	1.571	1.519	1.523	1.529
3	2.599	2.600	2.603	2.564	2.565	2.568	2.535	2.537	2.540
4	3.560	3.560	3.561	3.548	3.550	3.551	3.494	3.495	3.497
5	4.437	4.438	4.439	4.367	4.371	4.372	4.344	4.348	4.350
6	5.226	5.227	5.229	5.108	5.110	5.111	5.032	5.034	5.034
7	5.878	5.878	5.879	5.858	5.859	5.860	5.832	5.832	5.833
8	6.412	6.414	6.416	6.383	6.391	6.398	6.277	6.279	6.280
9	6.785	6.796	6.802	6.668	6.671	6.675	6.617	6.618	6.618
10	7.039	7.045	7.048	6.990	6.994	6.998	6.897	6.918	7.054

The mean values of peaks and estimates within the tolerance limit are given in Table 4.2 and Table 4.3. It has been mentioned previously that every modal plot, and the corresponding count plot, contains information regarding one node (and also a reference node kept constant across all analyses). Therefore, one modal amplitude and one frequency value is estimated from each peak cluster in a count plot, and there are as many count plots as the number of non-reference nodes. In Table 4.2, the maximum, the minimum, and the average values of frequencies obtained via the count plots pertaining to different nodes are given for each mode and each damage state.

Table 4.3. The mode shapes determined by O3KID / ERA and the count plots

Mode	Undamaged Case			Damaged Case 1			Damaged Case 2		
	1	2	3	1	2	3	1	2	3
DOF 1	0.148	-0.444	0.733	0.146	-0.407	0.783	0.142	-0.446	0.714
DOF 2	0.292	-0.804	1.061	0.291	-0.752	1.154	0.282	-0.822	1.066
DOF 3	0.429	-0.989	0.834	0.428	-0.961	0.933	0.416	-1.057	0.873
DOF 4	0.557	-1.003	0.156	0.555	-0.993	0.223	0.542	-1.076	0.244
DOF 5	0.673	-0.789	-0.616	0.67	-0.798	-0.606	0.656	-0.911	-0.523
DOF 6	0.776	-0.425	-1.055	0.767	-0.461	-1.122	0.781	-0.484	-1.126
DOF 7	0.863	0.007	-0.925	0.85	-0.061	-1.063	0.863	-0.07	-1.04
DOF 8	0.932	0.447	-0.312	0.934	0.48	-0.294	0.939	0.469	-0.26
DOF 9	0.978	0.794	0.465	0.975	0.81	0.476	0.976	0.804	0.499
DOF 10	1	1	1	1	1	1	1	1	1

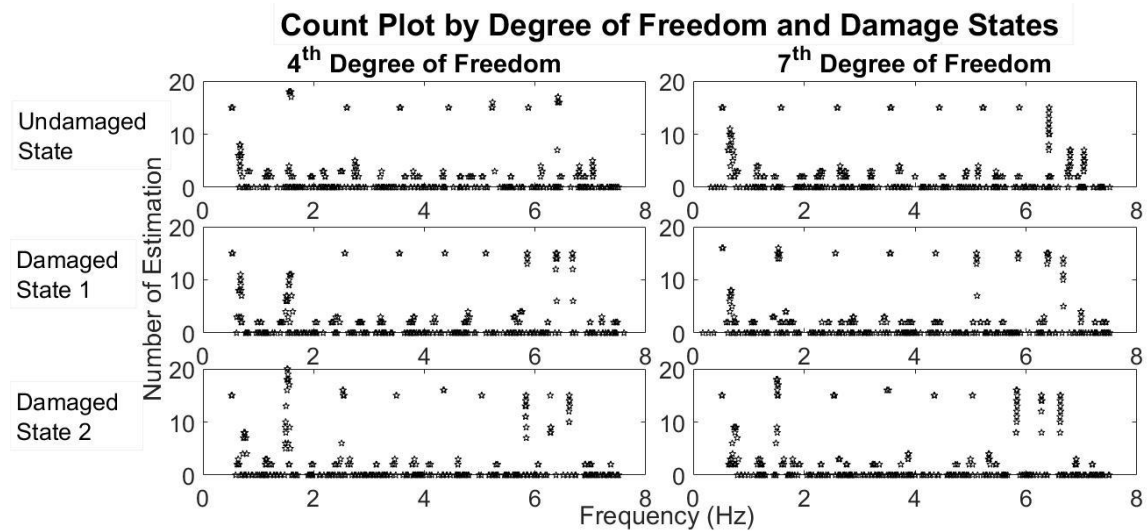


Figure 4.2. Count Plots for the 4th and the 7th DOFs for the three data sets.

The damage positions are determined using Equation 2.15 using the single mode indicator with only the first mode and the multiple mode indicator using the first three modes leading to the results presented in Figure 4.3. Based on the location of the critical nodes where the damage indicators show a pulse-like increase, it is observed that there is a certain ‘damage’ (i.e. an alteration) between the 7th and the 8th nodes (thereby indicating the 8th spring) when Damage Case 1 is compared with the Undamaged Case, and similarly that the 6th and the 8th springs are signaled as damaged when Damage Case 2 and the Undamaged Case are compared. It is also seen that the damage indicator calculated with the sum of the

first three modes for both cases can locate the damage more clearly than first mode damage indicator does.

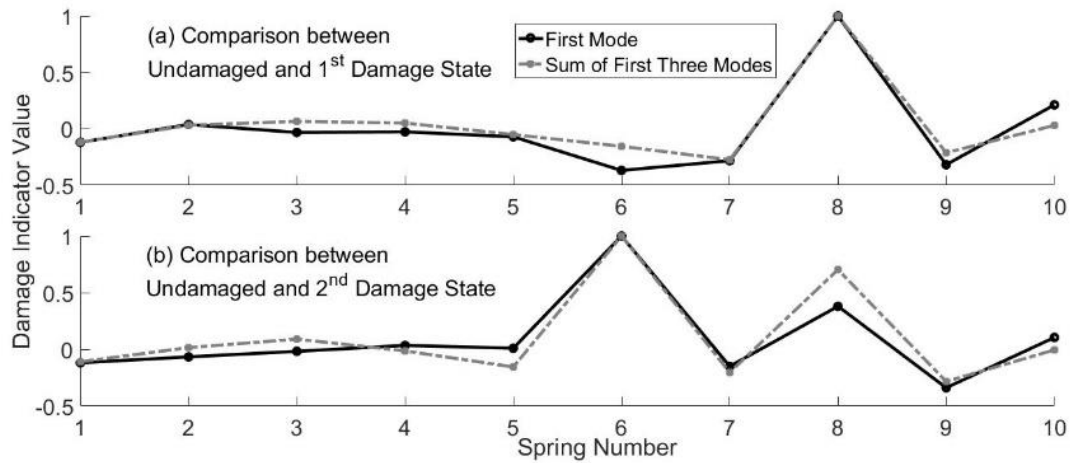


Figure 4.3. Damage indicator values for Damage Cases 1 and 2 for the 10 DOF system.

4.2. Fault Identification for Noise-Free Data with Limited Measurement Locations

In this section, the analysis conducted with exact modal variables in Section 2.5.2 is repeated for single and multiple damage cases using noise-free acceleration measurements simulated under ambient inputs. The 100 DOF spring-mass chain ‘cantilever’ system shown in Figure 4.4 is considered with a critical damping ratio of 1% for all modes. The first 10 natural frequencies are close to the natural-frequencies of the 10 DOF system discussed in Section 4.1. The acceleration data are ‘read’ at every 10th DOF, as in Section 2.5.2, and on those same DOFs white noise type forces are applied. For Damage Case 1, the stiffness of the 85th spring is reduced by 20%, and for Damage Case 2, the stiffness of the 55th and the 85th springs are reduced by 20%. Because a few number of measurements were used to locate the damage, the responses were analyzed with a high overlap (95%). Modal variables are determined automatically by using count plots and the information about the first three modes identified are presented in Table 4.4 and 4.5.

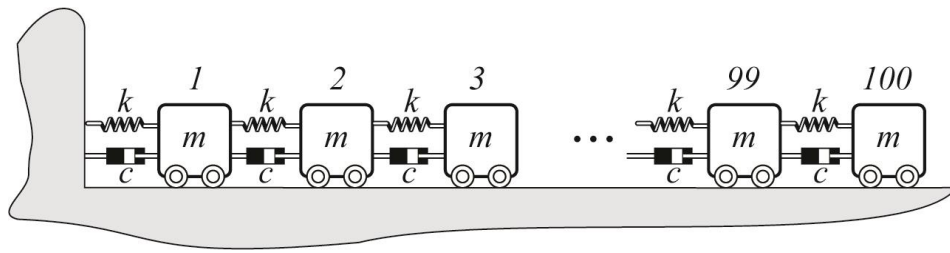


Figure 4.4. 100 DOF damped 'cantilever' system.

Table 4.4. Natural-frequencies determined by O3KID / ERA and count plot

Mod	Undamaged Case			Damaged Case 1			Damaged Case 2		
	Min	Average	Max	Min	Average	Max	Min	Average	Max
1	0.549	0.551	0.552	0.550	0.551	0.552	0.549	0.551	0.552
2	1.673	1.675	1.677	1.672	1.675	1.678	1.669	1.673	1.676
3	2.770	2.784	2.799	2.764	2.775	2.793	2.763	2.771	2.782

Table 4.5. Mode shapes determined by O3KID / ERA and count plots

Mode	Undamaged Case			Damaged Case 1			Damaged Case 2		
	1	2	3	1	2	3	1	2	3
DOF 1	0.156	-0.442	0.765	0.156	-0.436	0.745	0.156	-0.436	0.736
DOF 2	0.309	-0.784	1.098	0.308	-0.773	1.072	0.308	-0.779	1.061
DOF 3	0.453	-0.966	0.788	0.452	-0.952	0.797	0.451	-0.953	0.789
DOF 4	0.587	-0.934	0.023	0.586	-0.923	0.026	0.585	-0.928	0.026
DOF 5	0.706	-0.700	-0.664	0.706	-0.694	-0.648	0.704	-0.699	-0.642
DOF 6	0.809	-0.321	-1.054	0.808	-0.320	-1.035	0.809	-0.311	-1.031
DOF 7	0.890	0.143	-0.748	0.889	0.139	-0.739	0.890	0.142	-0.735
DOF 8	0.950	0.573	-0.031	0.949	0.566	-0.038	0.949	0.567	-0.053
DOF 9	0.987	0.881	0.681	0.987	0.881	0.685	0.987	0.881	0.686
DOF 10	1.000	1.000	1.000	1.000	1.000	1.000	1.000	1.000	1.000

Figure 4.5 shows that according to the first mode damage indicator and the multi-mode damage indicator comprising the first three modes, the location of possible damage for Damage Case 1 is estimated to be between the 80th and the 90th DOF, and the locations of possible damage for Damage Case 2 are estimated to be between the 50th and the 60th and between 80th and the 90th DOFs.

The results shown in Figure 4.5 indicate that the multiple mode damage indicator is more robust and it can help to determine the location of damage more consistently than the

first mode damage indicator. This is partly due to the fact that the first mode shape, especially with limited measurements, does not reflect significant variations with the damage scenarios considered herein. In order to determine the location of damage with smaller errors by using the first mode damage indicator, using a denser sensor array may be considered at the expense of increased installation and operation costs.

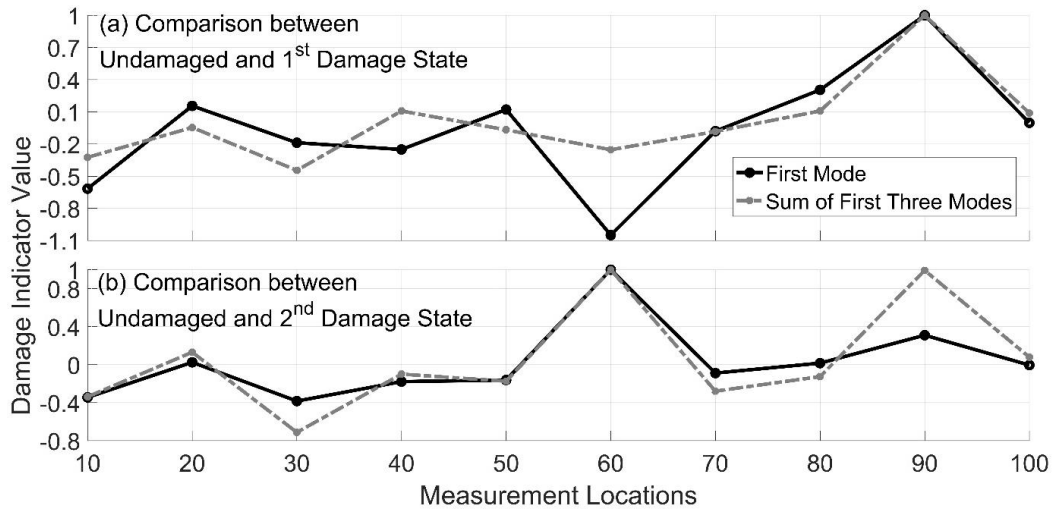


Figure 4.5. Damage indicator values for Damage Cases 1 and 2 for the 100 DOF system with limited measurements.

4.3. Fault Identification for Noisy Data

The 10 DOF system used in Section 4.1 is also used in this case study. Likewise, damage to the system is defined only as a reduction of the spring stiffness. For numerical analyses, the accelerations are simulated at all DOFs when system is excited with white noise type inputs applied at all DOFs, for a period of 1 minute with a sampling rate of 200 Hz, and ‘noise’ is added to the responses. The noise time histories are identically distributed independent random sequences. Data is generated for the undamaged system and 2 different damage conditions. Damage Case 1 corresponds to a 20% reduction in the stiffness of the 8th spring, and Damage Case 2 corresponds to 20% reductions in the stiffnesses of the 5th and the 8th springs. The purpose of this study is to estimate the system parameters with count

plots and to identify the locations of damage with the proposed damage indicator for noisy data in a fully instrumented system.

To examine the natural frequencies of the system and to observe the effects of noise, the PSDs obtained from the 1st DOF response data are given in Figure 4.6. The data seems to indicate clearly separated peaks and observable shifts in the frequencies when the three damage cases are considered. On the other hand, the effects of noise become apparent when the PSD estimates obtained via noisy and noise free data are considered as shown in Figure 4.7. In this figure it is clearly seen that the peak amplitude corresponding to the 1st mode gets buried under noise.

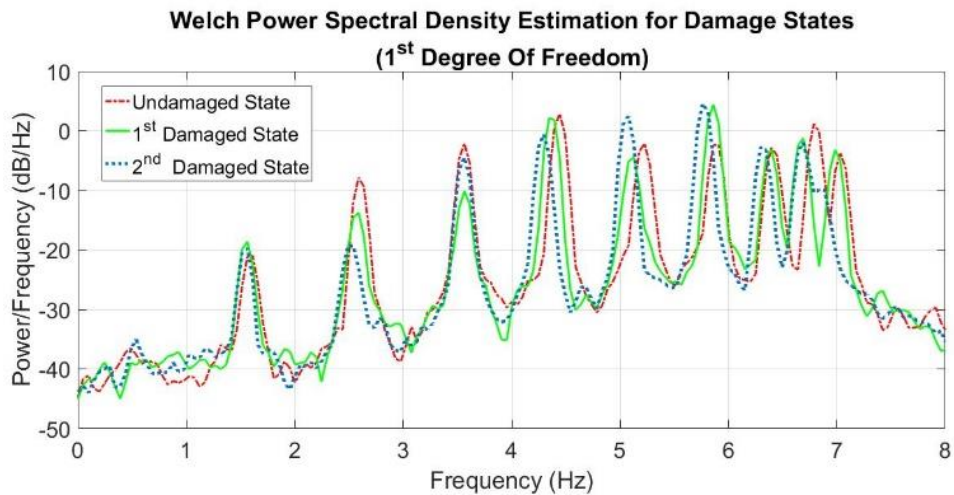


Figure 4.6. PSD estimates obtained using the noisy acceleration data measured from the 1st DOF for the damage cases considered (0-8 Hz).

The first two steps described above provide preliminary information about the data and the system. In the third step, first order dynamic models are established with the O3KID/ERA approach and modal variables are calculated from these models. Using ± 0.008 tolerance limit for the modal variables, the count plots shown in Figure 4.8 are produced. Modal variables that have the highest count value within the tolerance limit and the range given in Table 4.1 are estimated and the mean values of the clusters within the tolerance limit are given in Table 4.6 through Table 4.9. In the analyses with O3KID / ERA, every DOFs is analyzed one by one with the (reference) 10th DOF, and the data is divided into 25 second segments with 95% overlaps.

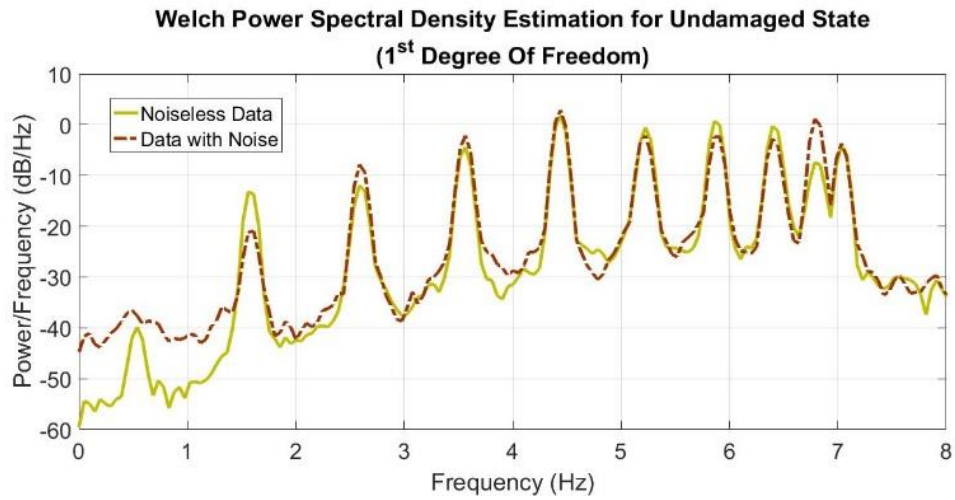


Figure 4.7. PSD estimates obtained using noisy and noise free data measured from the 1st DOF for the undamaged system (0-8 Hz).

Table 4.6. Natural frequencies determined by O3KID / ERA and count plots

Mod	Undamaged Case			Damaged Case 1			Damaged Case 2		
	Min	Average	Max	Min	Average	Max	Min	Average	Max
1	0.528	0.530	0.532	0.523	0.526	0.536	0.517	0.521	0.523
2	1.589	1.591	1.595	1.550	1.551	1.552	1.539	1.547	1.555
3	2.597	2.598	2.599	2.573	2.575	2.576	2.518	2.522	2.524
4	3.560	3.563	3.567	3.545	3.561	3.569	3.555	3.556	3.557
5	4.438	4.439	4.440	4.365	4.366	4.367	4.290	4.291	4.294
6	5.205	5.213	5.230	5.100	5.105	5.114	5.063	5.064	5.065
7	5.881	5.882	5.884	5.857	5.858	5.859	5.774	5.776	5.777
8	6.410	6.412	6.415	6.378	6.382	6.385	6.316	6.317	6.317
9	6.799	6.800	6.801	6.669	6.673	6.678	6.676	6.677	6.678
10	7.033	7.035	7.036	6.989	7.038	7.407	7.097	7.145	7.213

For each segment, the number of observers is set to 800 in O3KID analysis and a total of 390 frequencies between 0-100 Hz and their corresponding mode shapes relative amplitudes are calculated for the tolerance limit ± 0.008 . In Table 4.6, the maximum, the minimum, and the average values of frequencies obtained via the count plots pertaining to different nodes are given for each mode and each damage state.

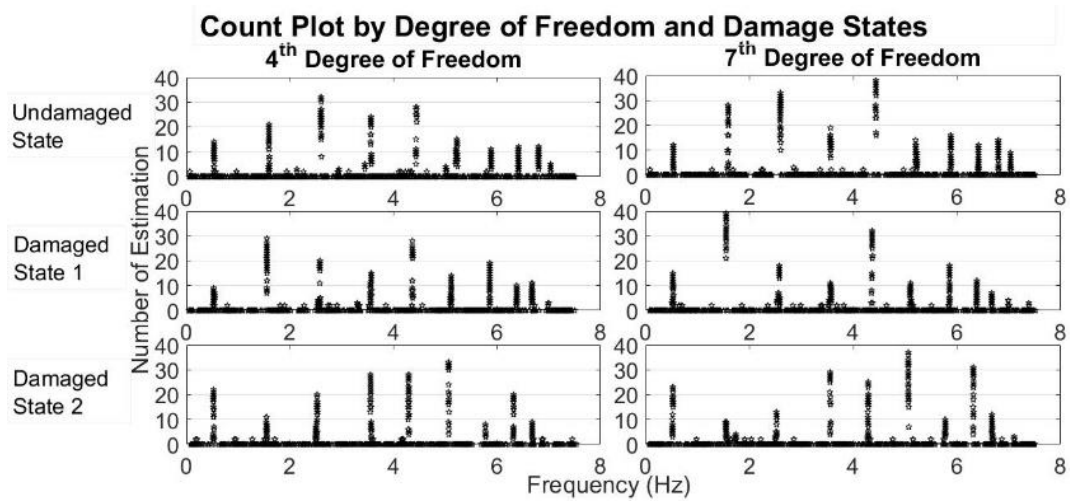


Figure 4.8. Count plots for the 4th and the 7th DOFs for the three cases.

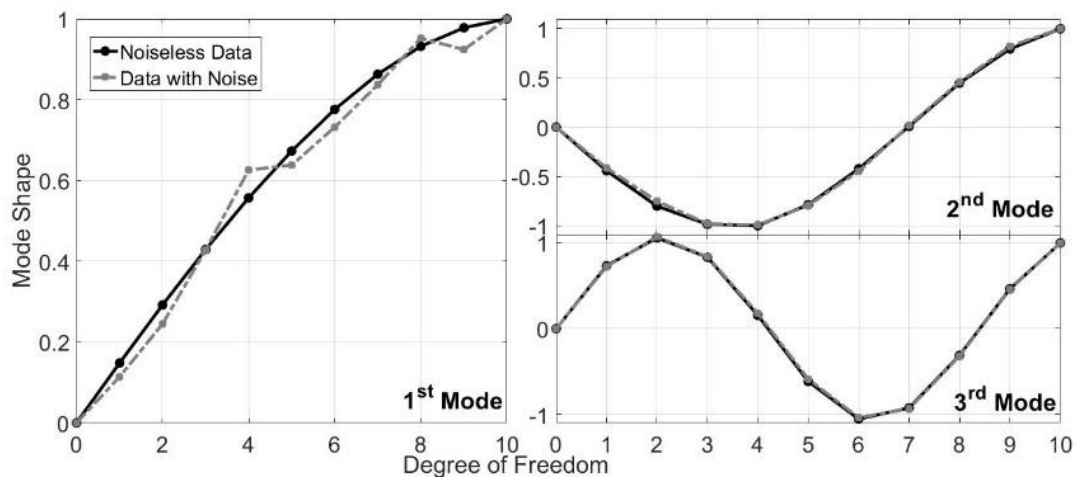


Figure 4.9. Effects of noise on mode shapes.

The first three mode shapes identified via noisy and noise free data are sketched in Figure 4.9. It is seen from the comparison with the noise free case presented in Section 4.1 that noise affects the 1st mode shape of the system considerably. This finding is in line with the previous observation that the peak amplitude of the first mode was somewhat concealed by the noise.

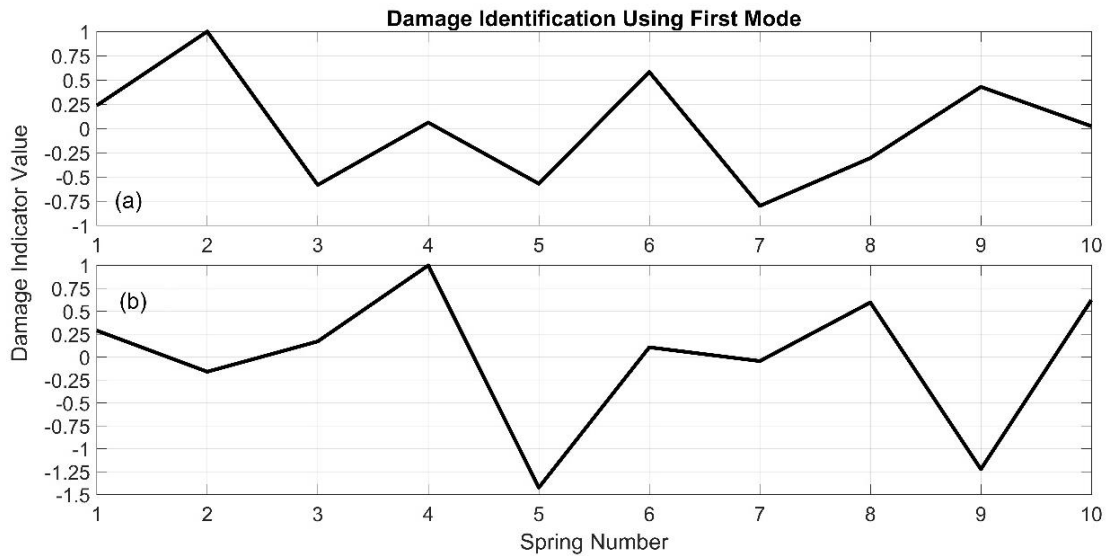


Figure 4.10. Single mode damage indicator calculated using the 1st mode: (a) comparing Damage Case 1 with the Undamaged Case, (b) comparing Damage Case 2 with the Undamaged Case.

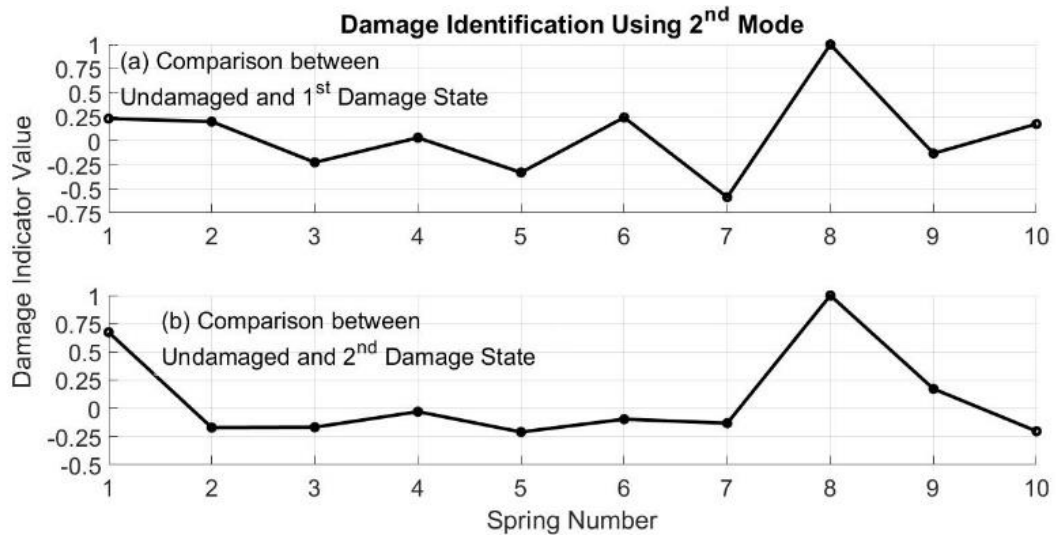


Figure 4.11. Single mode damage indicator calculated using the 2nd mode: (a) comparing Damage Case 1 with the Undamaged Case, (b) comparing Damage Case 2 with the Undamaged Case.

The same deteriorating effect, however, is not dominant in the other two modes so that the results obtained for the second and the third modes seem to be quite accurate. Firstly, the single mode damage indicator is calculated using the 2nd mode. The results, shown in Figure

4.11, imply that there is a change in the stiffness of the 8th spring when Damaged Case 1 is compared with the Undamaged Case, and that there are changes in the stiffness of the 1st and the 8th springs when Damage Case 2 is compared with the Undamaged Case.

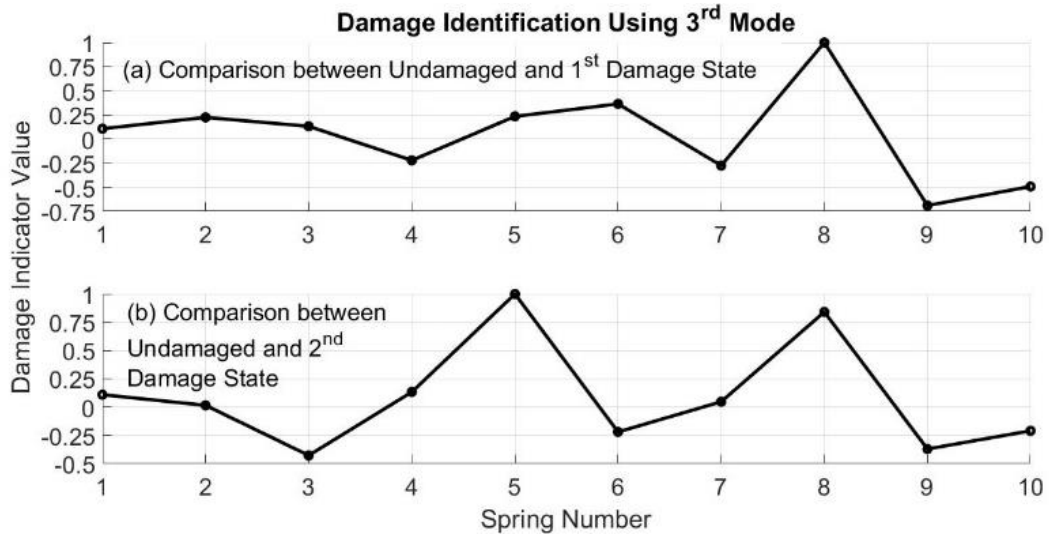


Figure 4.12. Single mode damage indicator calculated using the 3rd mode: (a) comparing Damage Case 1 with the Undamaged Case, (b) comparing Damage Case 2 with the Undamaged Case.

Secondly, the single mode damage indicator is calculated using the 3rd mode. The results, shown in Figure 4.12, imply that there is a change in the stiffness of the 8th spring when Damage Case 1 is compared with the Undamaged Case, and that there are changes in the stiffnesses of the 5th and the 8th springs when the Damage Case 2 is compared with the Undamaged Case.

The results are affected also by the presence of what are termed here as ‘saddle points’. The saddle points of a damage indicator are those locations at which the derivative of the mode shape are zero. The identifiers of those springs (spring numbers) that overlap with the locations of the saddle points are given in Table 4.10. The results shown in Figure 4.11 and Figure 4.12 both indicate the existence of damage on the 8th spring when Damage Case 1 is compared with the Undamaged Case. When Damage Case 2 and the Undamaged Case are compared, however, there is a discrepancy between the single mode indicators calculated via the 2nd and the 3rd mode shapes: the result obtained from the second mode damage

indicator imply damage in the 1st and the 8th springs, whereas the third mode damage indicator implies damage in the 5th and the 8th springs. As Table 4.10 shows, the 5th spring overlaps with the location of the saddle point for the 2nd mode, whereas the saddle points of the 3rd mode do not overlap with any of the damage locations. Consequently, the damage estimate obtained via the 2nd mode damage indicator is adversely affected by the existence of the saddle point, whereas the 3rd mode indicator is not. The first mode, which will not be adversely affected by any saddle point, is however not available for this particular example, and this unavailability. The inability to use the first mode without saddle points makes it difficult to judge strongly.

Table 4.10. Numbers of the springs overlapping with the saddle points of the first three modes of the 10 DOF system

Mode	Springs overlapping with saddle points
1	-None-
2	5th spring
3	3rd and 7th springs

It is evident in the example given in this section that saddle points may lead to errors in the detection of damage via the proposed approach. For this reason, this section discusses SHM system sensor deployment strategies to remedy this issue. The issue of which sensors should be employed and how they should be deployed on a structure is generally both structure and methodology dependent. For example, in Meehan (2011), it is recommended that strain gauges should be installed on those locations where the largest displacements occur when different loading scenarios are considered in static analyses, and that accelerometers should be placed on or near saddle points identified during dynamic analyses. It is also recommended, based on to results of damage detection studies conducted on real construction applications, that strain gauges or Large Area Electronics (LAE) should be installed at the saddle points of the first three or even higher modes and accelerometers should be placed on both sides of the saddle points. According to this criterion, possible deployment strategies for sensor sets including LAE and accelerometers for the 100 DOF cantilever and simply supported systems considered in the previous sections may be chosen to comprise the layouts shown schematically in Figure 4.13.

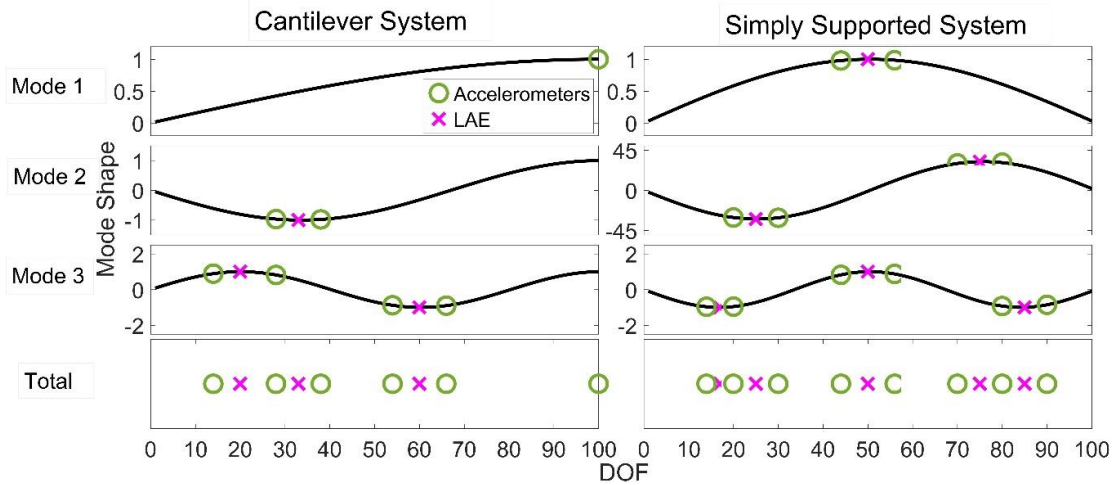


Figure 4.13. Deployment of sensors for the cantilever and simply supported system.

As a final note to conclude this section, we discuss whether it would be possible to further the analyses by estimating the amount of damage. This analysis is strictly restricted to those systems which have diagonal mass matrices with all the non-zero values equal to each other (i.e. all the lumped masses are equal). The well generalized eigenvalue problem governing the frequencies and mode shapes of a mechanical system is given by

$$K\Phi = M\Phi\Lambda, \quad (4.1)$$

where Φ is the mode shape matrix with its columns containing arbitrarily scaled mode shapes; Λ is the diagonal matrix containing the eigenvalues (squares of the natural frequencies) on its diagonal. K and M are the stiffness and the mass matrices of the system. When the mass matrix is diagonal with all diagonal entries equal, this eigenvalue problem may be expressed as

$$K\Phi = aI\Phi\Lambda = a\Phi\Lambda, \quad (4.2)$$

where I is the identity matrix comprising one (1) on its diagonal and zeros everywhere else, and a is a scalar. If all the modal parameters, i.e. all the frequencies and the (arbitrarily scaled) modeshapes, are identified, then the stiffness matrix may be approximated through Eq. (4.2) up to an unknown scalar coefficient:

$$\tilde{\mathbf{K}} = a\Phi\Lambda\Phi^{-1}. \quad (4.3)$$

In this expression, $\tilde{\mathbf{K}}$ is an estimate for the stiffness matrix and a is an undetermined scalar coefficient whose determination requires knowledge of the mass. The ordering of the eigenvalues and the mode shapes is assumed to be consistent in constructing these matrices. Note that the scaling of the modeshapes has no bearing on the estimate. To see why this is so, consider two sets of modeshapes Φ and $\hat{\Phi}$ scaled differently so that $\hat{\Phi} = \Phi\Theta$ where Θ is a diagonal matrix containing scaling coefficients on its diagonal. In this case one would have

$$\tilde{\mathbf{K}} = a\hat{\Phi}\Lambda\hat{\Phi}^{-1} = a\Phi\Theta\Lambda\Theta^{-1}\Phi^{-1} = a\Phi\Lambda\Phi^{-1}, \quad (4.4)$$

so that the scaling coefficients in Θ are seen to have no effect on the final estimate.

In order to identify the changes in the stiffness matrix, relative changes in the estimated stiffness coefficients are used:

$$H_{ij} = 100(\tilde{\mathbf{K}}_{ij}^d - \tilde{\mathbf{K}}_{ij}^u)/\tilde{\mathbf{K}}_{ij}^u, \quad (4.5)$$

where, H is the matrix of relative changes of the stiffness matrix (as percentage), lower indices i and j denote the row and column numbers, respectively; upper indices d and u denote the damaged and the undamaged cases, respectively. The important observation is, even if the stiffness matrix may not be uniquely identified since the scalar a is unknown when the mass distribution is unknown, the relative change matrix H may still be uniquely identified if the mass matrix is constant between the damaged and the undamaged cases. For the 10 DOF system under consideration, the relative change matrices corresponding to the two damage states are given in Table 4.11 and Table 4.12.

The maximum decrease in the relative change matrix presented in Table 4.11 is about 21% at the location of the 8th spring; the corresponding values in Table 4.12 are about 20% at the location of the 8th spring and in excess of 16% at the location of the 5th spring. The small positive and negative values observed in these tables are due to the errors in the identified modal parameters which, as the reader would recall, were identified with noisy data, which adversely affected particularly the 1st mode results.

Table 4.11. Relative Stiffness Matrix for Damage Case 1 as percentage

		Column Number										
		1	2	3	4	5	6	7	8	9	10	
Row Number	1	0.4	-0.5									
	2	2.3	-0.3	1.0								
	3		0.2	0.2	2.9							
	4			-4.6	1.1	-5.5						
	5				10.3	2.5	9.4					
	6					-4.9	-0.3	0.9				
	7						1.8	-11.3	-21.1			
	8							-21.3	-8.3	-2.1		
	9								1.8	-1.8	3.5	
	10									-0.7	1.4	

Table 4.12. Relative Stiffness Matrix for Damage Case 2 as percentage

		Column Number										
		1	2	3	4	5	6	7	8	9	10	
Row Number	1	4.1	16.3									
	2	0.3	0.4	2.4								
	3		16.3	7.8	13.7							
	4			-13.1	-12.3	-27.9						
	5				-16.0	-8.8	3.5					
	6					7.0	1.5	4.9				
	7						0.6	-10.1	-19.5			
	8							-20.5	-5.8	-2.6		
	9								5.8	-2.1	5.2	
	10									6.1	3.7	

Although this analysis is restricted to those systems with identical masses on the diagonal mass matrices, the results still are useful in that they clearly show the efficacy of the proposed approach in identifying modal parameters from noisy data as well as collaborating the results obtained via the damage indicators. The results of the relative stiffness matrices comply well with single mode damage indicators previously discussed.

4.4. Level 0 Damage Detection on a Beam with Hinges Using Modal Zones

In this experimental study, it is aspired to detect damage in an actual steel beam. For this purpose, an intact steel beam with a hollow-rectangular cross-section is cut into nine almost identical pieces with a cut angle of 45° . These segments are reconnected to each

other using bolts and nails. Holes the size of the diameters of the nails are drilled into the samples. And bolts are tightened so that the nails are placed into these holes prevent any relative sliding of the segments. The cross sectional dimensions are 40 mm by 40 mm, and the wall thickness of the specimen varies from 1.6 mm to 2 mm. When bolts are loosened, slight sliding is possible along the connection zone. This small sliding in turn leads to a reduction in the interaction area.

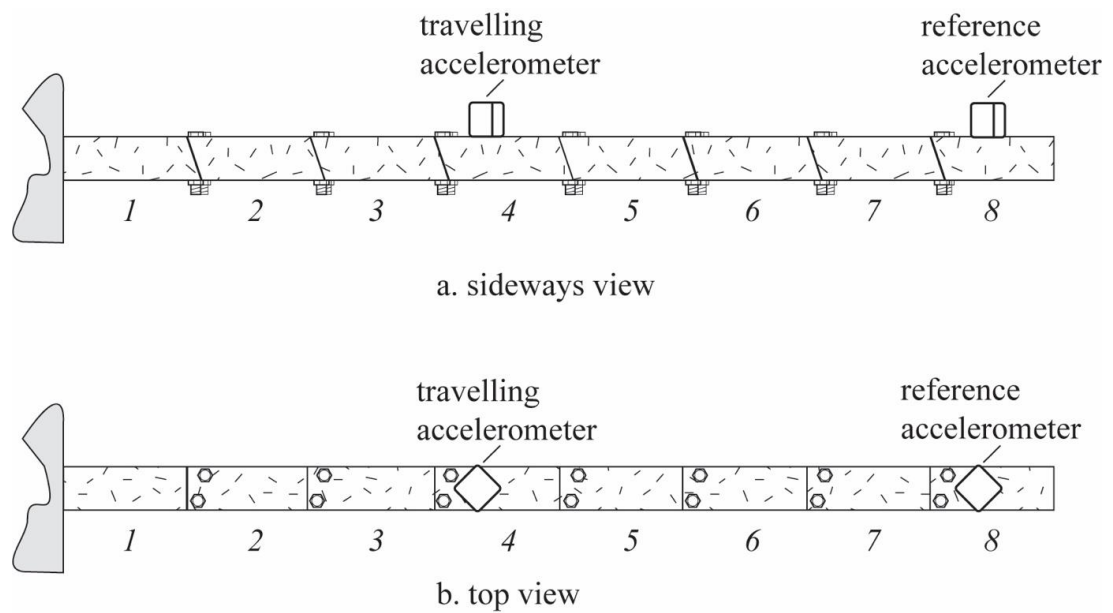


Figure 4.14. Schematic representation of the steel beam showing segment numbers and the locations of the accelerometers.

Due to their availability, the accelerometers used in this study are Kinematrix EpiSensor ES-U2 force balance uniaxial accelerometers. It should be noted that the system properties change depending on the measurement location due to the mass of the accelerometer. The mass of an accelerometer is 346 grams and mass of each segment is around 280 grams. When the measurement location is changed, the mass distribution of the system also changes, which results in a variation in the system in every measurement. On the other hand, only one damage scenario as will be described below is considered. Therefore, the whole analysis amounts to one damage scenario, defined as the loosening of the bolts at one location, being tested for seven similar but different systems in this case study.

The damage imposed is the loosening of two of the bolts located on the 5th piece from the fixed end as marked on the photograph of the specimen shown in Figure 4.15. The bolts are loosened to the level at which they can be further loosened by hand.

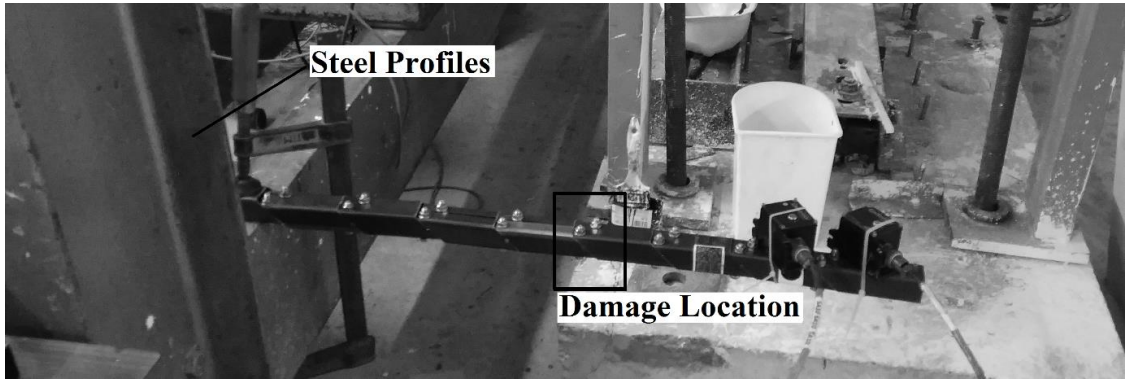


Figure 4.15. Experimental setup and the black box marks the damage position.

The specimen is instrumented with two uniaxial accelerometers aligned with the vertical, one of which is located on the last segment at the free end, and the second one being moved to a different segment at each test. For each setup, the duration of measurements is five minutes with a sampling rate of 200 Hz.

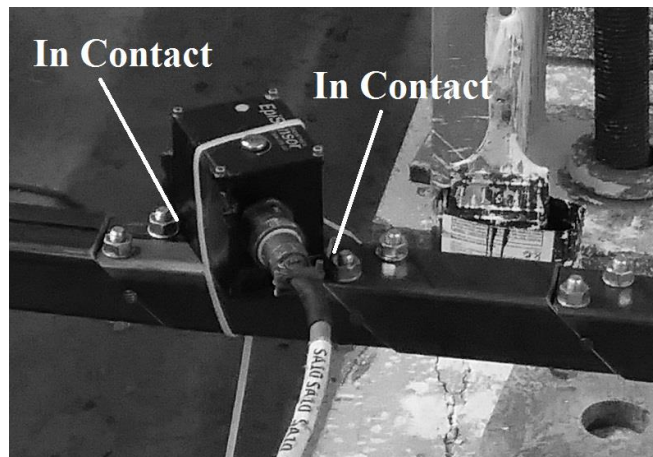


Figure 4.16. Accelerometer orientation.

The sensor located at the same location in all the tests is treated as and referred to as the 'reference sensor' while the second sensor is referred to as the 'travelling sensor'. A close up of sensor installation is presented in Figure 4.16.

The measurements are done in the following order (numbers refer to Figure 4.14):

Before damage: segment 7, 6, 5, 4, 3, 2, 1

After damage: segment 1, 2, 3, 4, 5, 6, 7

The system is excited by ambient inputs. Only once a periodic force is applied manually with fingertips before the onset of damage in the 2nd segment measurement and it is pursued for most of the duration of that set of measurements in order to observe any effects related to the amplitude variation of the input force in the modal plot. The L_1 and L_2 norms of the normalized response measurement at the reference measurement, defined by

$$L_1 = \sum_i |y(t_i)|, \quad L_2 = \sqrt{\sum_i |y(t_i)|^2} \quad (4.6)$$

where $y(t_i)$ is a zero-mean time series sampled at t_i for $i = 0, 1, 2, \dots$, are given in Table 4.13. The normalization process comprises removing the mean of the signal. Any impulsive deviations caused by the sudden environmental disturbances are excluded from the signal and thus some of the modal plots provide fewer estimates than the others.

Table 4.13. Norms of signals measured by the reference

Location of the Travelling Sensor	Damage Type	L_1	L_2
1	Undamaged	16.812	0.341
1	Damaged	55.646	0.669
2	Undamaged	2.776	0.017
2	Damaged	2.523	0.014
3	Undamaged	2.317	0.013
3	Damaged	4.778	0.070
4	Undamaged	2.597	0.017
4	Damaged	5.601	0.066
5	Undamaged	2.950	0.015
5	Damaged	3.599	0.022
6	Undamaged	3.000	0.021
6	Damaged	5.123	0.035
7	Undamaged	2.279	0.011
7	Damaged	2.737	0.015

Figures 4.17 through 4.24 present modal plots and count plots developed for damaged and undamaged cases. Figures of modal plots contain two plots, one corresponding to pre damage and one corresponding to post damage, with both plots obtained for the system with identical mass distribution (i.e. the same location for the travelling sensor). The distinct peaks observed on the count plots of Figure 4.18.

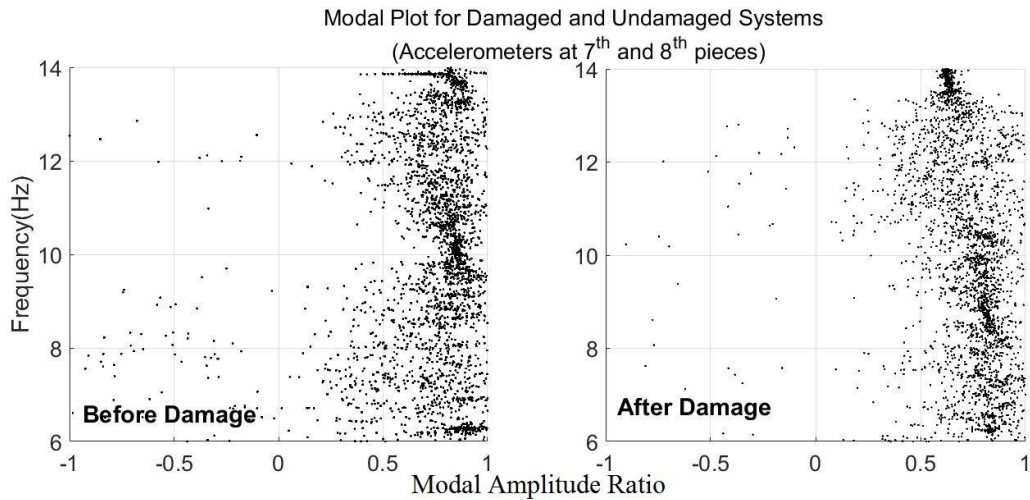


Figure 4.17. Modal plots for the undamaged and the damaged steel beam (accelerometers on the 7th and the 8th segments).

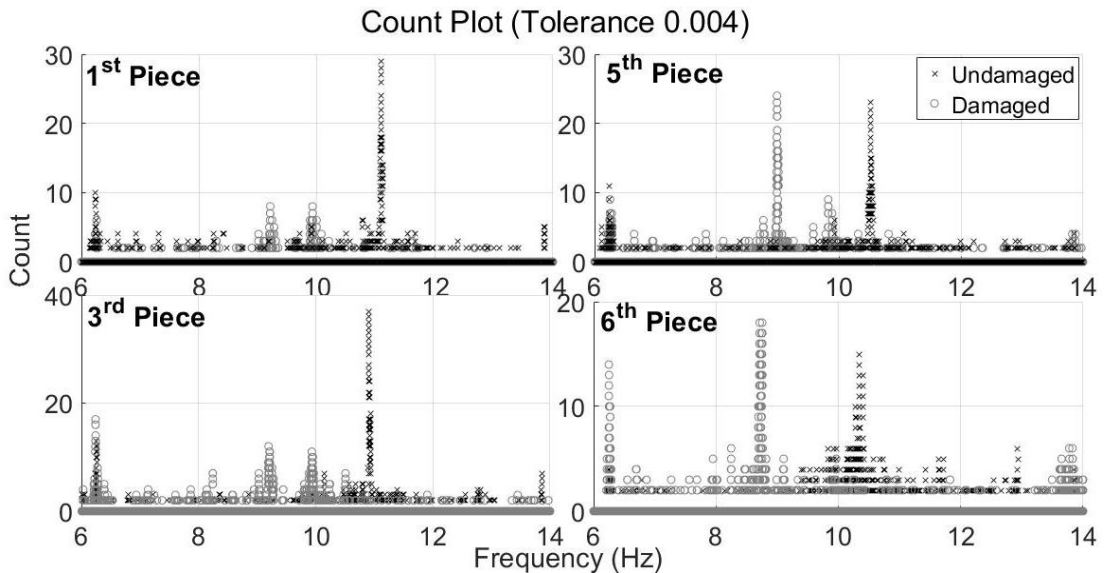


Figure 4.18. Count plots for the experimental beam (tolerance limit 0.004).

A close inspection of Figures 4.19 to 4.24 show that damage has changed the nature of the distribution of points in the first modal zone from 10-11 Hz down to 9-10 Hz. Moreover, at every post-damage measurement, there is a separation in the modal zone between 9-10 Hz which is not encountered in the pre-damage counterparts between 10-11 Hz. Systems have different mass distributions but have the same end conditions, and they are damaged at the same location with the same damage extent. Also, ambient vibration magnitudes are different as can be seen in Table 4.13. In addition, the same behavior is observed in six post-damage measurements and there is no evidence of such behavior in the measurements before the damage. Although this does not provide a conclusive proof, the behavior observed for this particular example implies that the distribution of computational modes within the modal zone may also be investigated such that a significant qualitative change in this distribution may be indicative of a certain systemic variation. Such an information may be useful for the Level 0 damage detection problem.

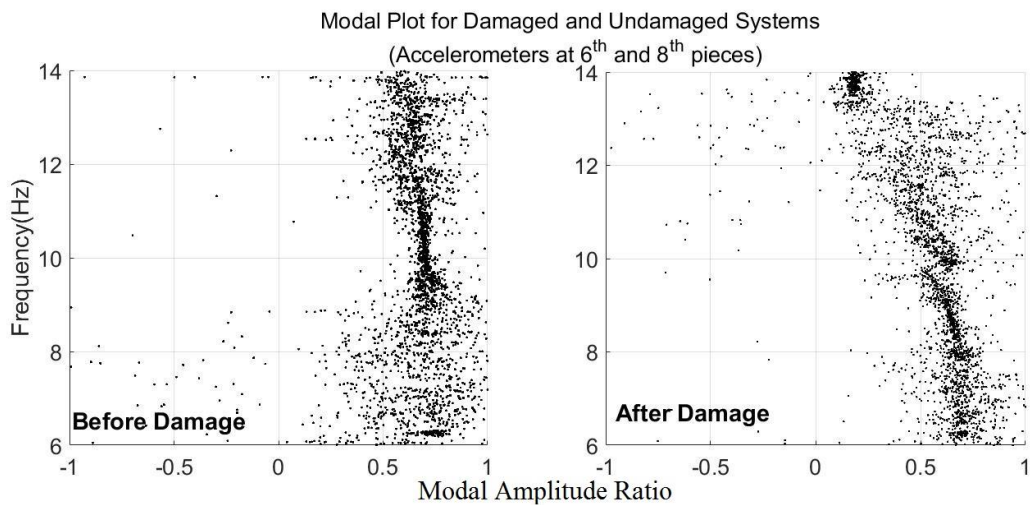


Figure 4.19. Modal plots for damaged and undamaged systems (accelerometers on 6th and 8th segments).

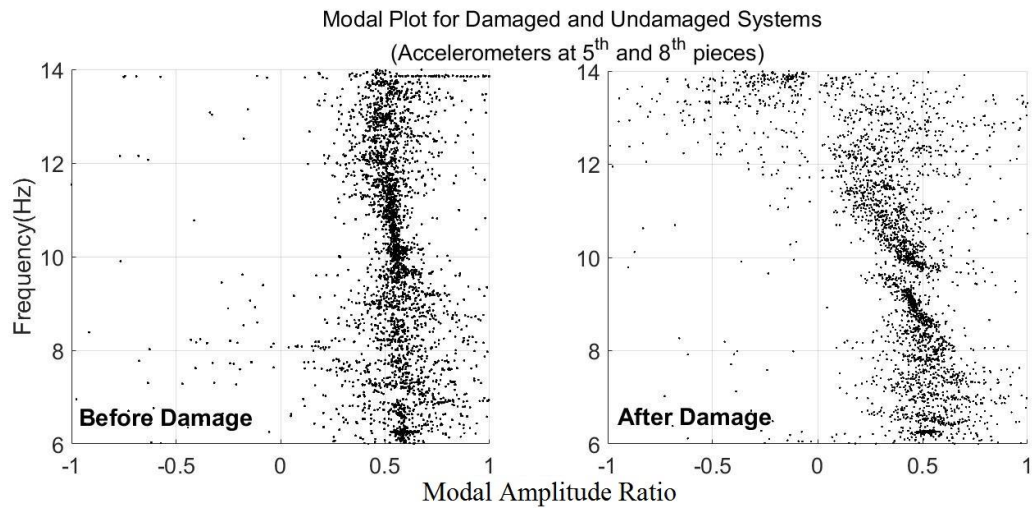


Figure 4.20. Modal plots for damaged and undamaged systems (accelerometers on 5th and 8th segments).

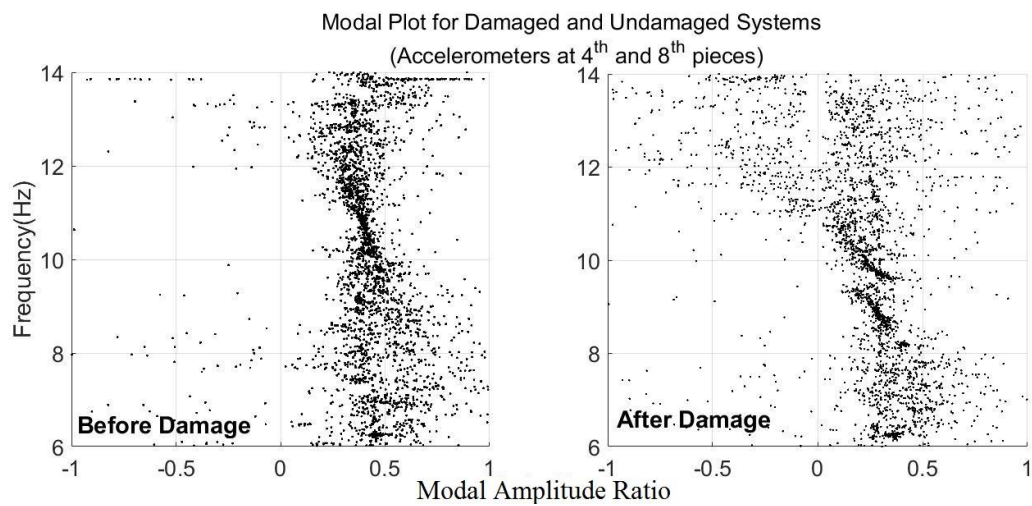


Figure 4.21. Modal plots for damaged and undamaged systems (accelerometers on 4th and 8th segments).

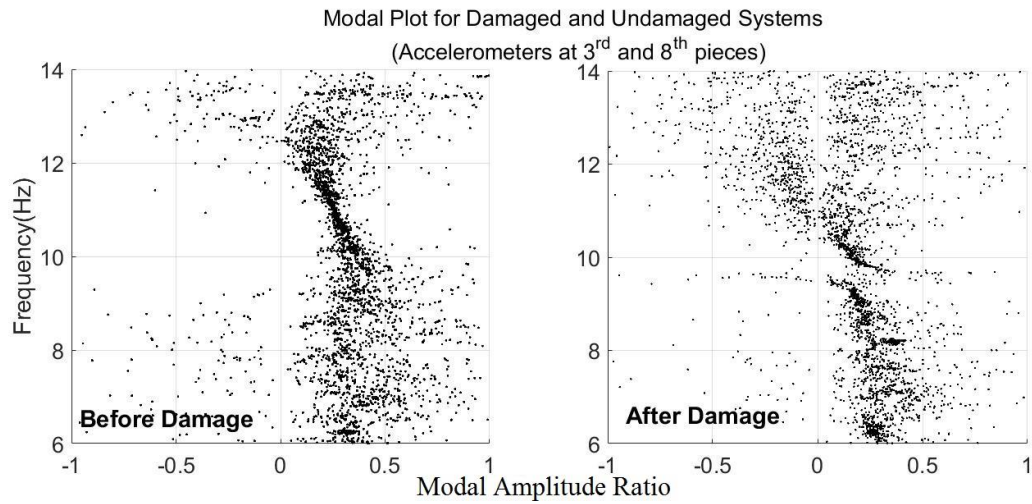


Figure 4.22. Modal plots for damaged and undamaged systems (accelerometers on 3rd and 8th segments).

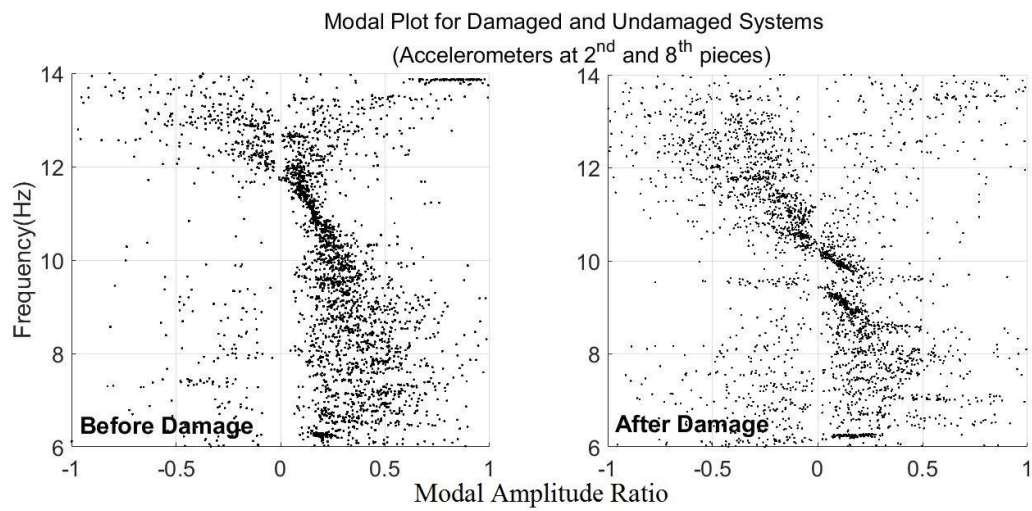


Figure 4.23. Modal plots for damaged and undamaged systems (accelerometers on 2nd and 8th segments).

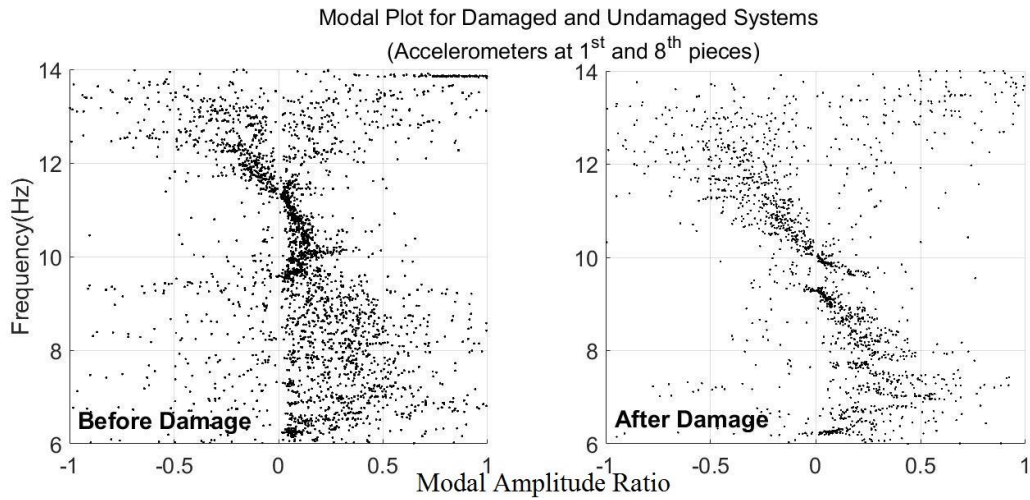


Figure 4.24. Modal plots for damaged and undamaged systems (accelerometers on 1st and 8th segments).

One possible benefit of this approach might be to offer an alternative for the problems associated with the dependence of modal points on environmental factors. It may prove to be difficult to detect the presence of damage by evaluating only the changes in the natural frequencies since it is well known that environmental factors may cause similar variations on the natural frequencies (Jiménez-Roa et al., 2016). To investigate the whole distribution in the modal zone, on the other hand, may be less prone to contributions from such effects since the distribution of computational modes may be expected to not depend explicitly of environmental factors such as temperature variations. A more rigorous discussion of this possibility would require extensive experimental work with controlled environmental variations but such a study is outside the scope of this work.

4.5. Level 1 Damage Identification of a Beam with Hinges Using the Damage Indicator

To further the discussion, in this section the experimental model considered above is reevaluated with an analogous numerical model with the aim of applying the proposed damage indicator for Level 1 detection. The other aims are (a) to show that the unscaled damage indicator defined in Equations 2.15 and 2.16 provides information on the extent of damage, and (b) to show the use of damage indicator on a system where rotational DOFs are

defined. To this end, exact values of modal parameters are calculated from the stiffness and the mass matrices of the numerical model.

The system used in Section 4.4 is a closed system in the sense that even though the internal distribution of the mass changes, the total mass of the system is constant. To investigate the possibility of the application of the damage indicator to such a problem, the proposed damage indicator will be tested for such a closed system in a numerical example where rotational and translational DOFs are defined for every element in the system. In other case studies in the thesis, systems for which rotational DOFs are inconsequential have been considered. Rotations may, however, be important for such a beam as used in the experimental work discussed in Section 4.4, and therefore the rotational DOFs are included here.

The numerical model employed in this section is a 30 DOF system with 15 beam elements in series. For every element, rotational and translational DOFs are defined at nodes. Section properties and modulus of elasticity of the beam elements are identical with system used in the Section 2.4.2. The stiffness and mass matrices of each beam element are identical and in compliance with the Bernoulli-Euler beam model. Mass of each accelerometers is equal to 1.25 times the translational mass of each piece. Four states of the system are considered (a) undamaged system, system with (b) 50% reduction, (c) 75% reduction and (d) 85% reduction in the modulus of elasticity of the 5th beam element.

Both unscaled and scaled equations are used when comparing the undamaged state and one of the damaged states of the system in order to locate the damage. For the unscaled damage indicator defined in Equation 2.15, the extent of damage can be detected as an increase in the damage indicator values as can be seen in Figure 4.25. However, the extent of damage is not apparent when the scaled damage indicators (calculated using Equation 2.17) are used as seen in Figure 4.26.

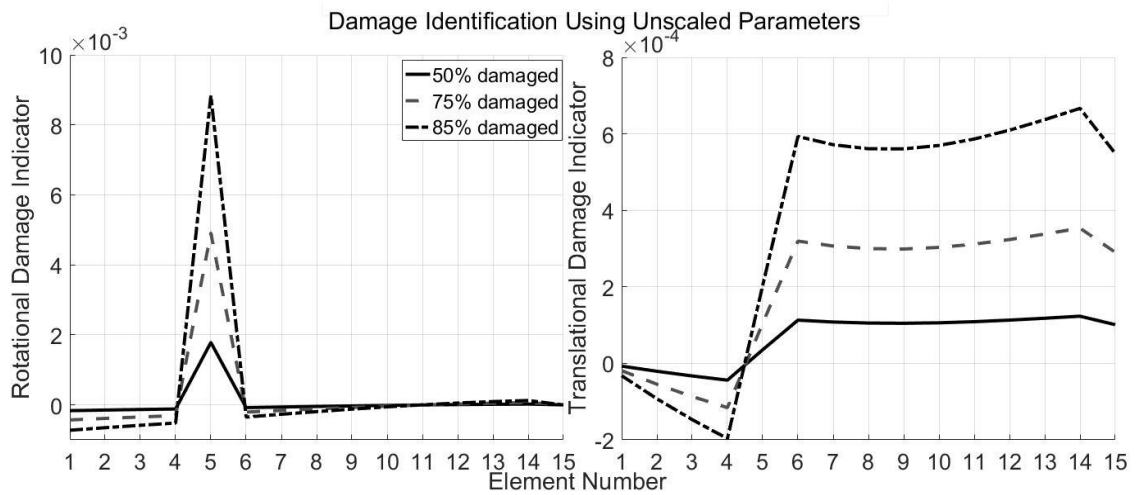


Figure 4.25. Unscaled Damage Indicator using Equation 2.15.

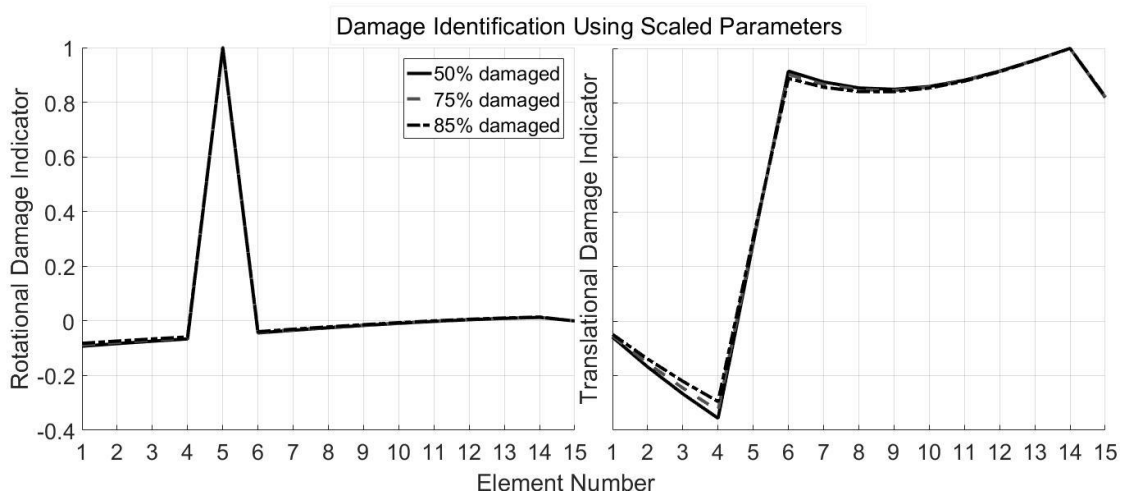


Figure 4.26. Scaled Damage Indicator using Equation 2.17.

Figures 4.25 and 4.26 show that when damage is at a single location, the damage indicator calculated with the first rotational mode is positive for a damage location and is negative for undamaged locations. On the other hand, the translational damage indicator value changes sign on the damage location. The damage indicator for the damaged element and for the higher numbered elements takes a positive value and negative in all previous locations.

Only translational responses are measured and the rotations are not measured in the experimental study in Section 4.4. The translational damage indicator value is expected to

be positive starting from the damaged element to the tip element and will be negative between the damaged element (omitted) and the support.

It is important to note that the natural frequencies and mode shapes have been found by solving the eigenvalue problems of the systems. Since the mass matrix is dependent on the location of the second sensor, the natural frequencies of the system also depends on this location (see Table 4.14). Because the travelling sensor and the reference sensor are not located on the same segment (on the last segment at the free end of the beam), the same natural frequency values are used for the element at the tip and the element closest to the tip element.

Table 4.14. Estimated Modal Parameters for the first mode

Element Number	Undamaged		Damaged	
	Natural Frequency	Mode Shape	Natural Frequency	Mode Shape
1	11.083	0.047	9.204	0.035
2	11.093	0.151	9.220	0.098
3	10.910	0.265	9.195	0.177
4	10.754	0.397	8.918	0.282
5	10.523	0.538	8.987	0.457
6	10.341	0.696	8.714	0.646
7	10.095	0.847	8.714	0.815
8	10.095	1.000	8.714	1.000

The translational mode shape of the damaged and undamaged systems are given in Table 4.14 and in Figure 4.27. The translational damage indicator is also given in Figure 4.28. The sign change is observed at the fifth element which is the damaged element as in the expectations.

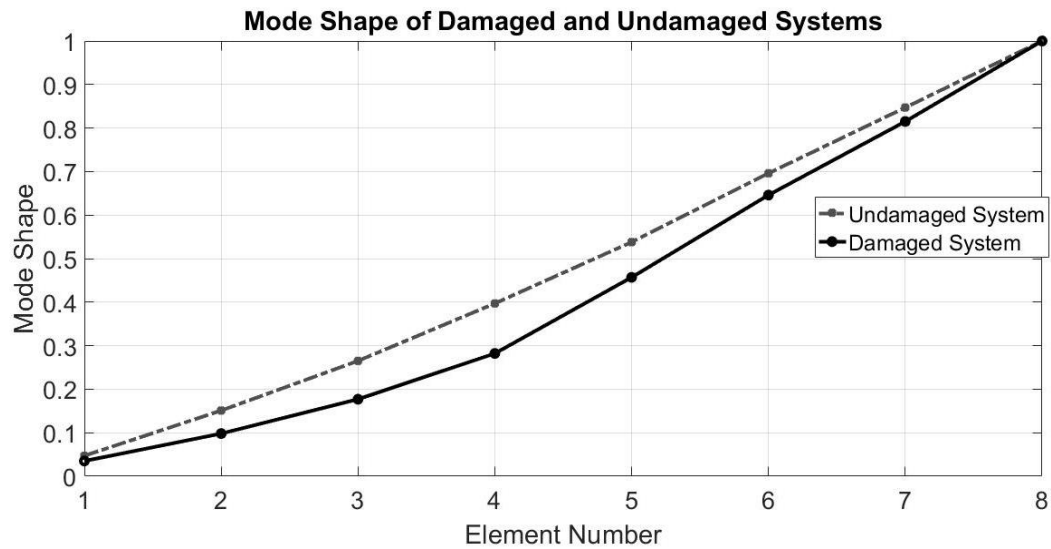


Figure 4.27. Mode Shape for two states of the system.

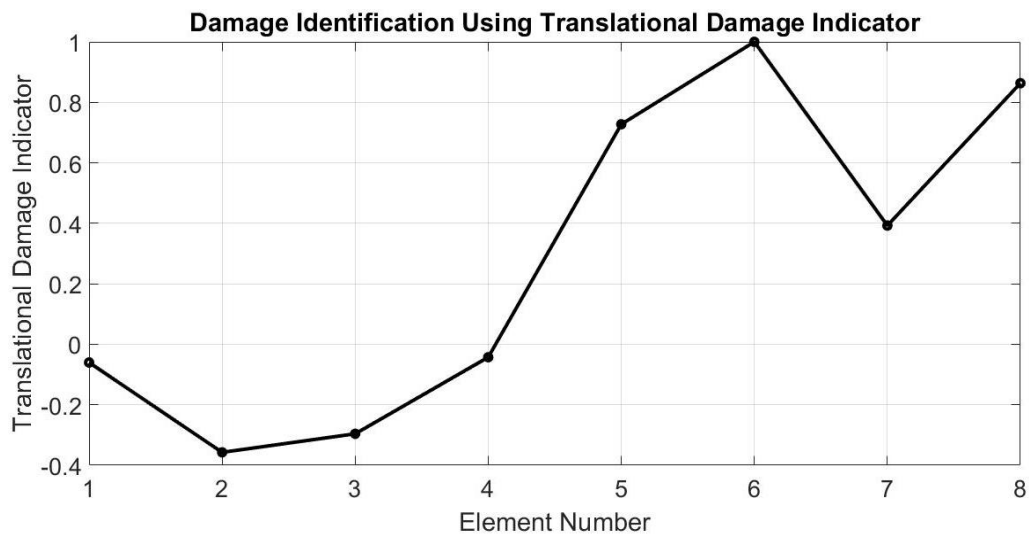


Figure 4.28. Location of damage using Translational Damage Indicator for the experimental study.

Based on the observations regarding this example, it is evident that rotational mode shapes should be measured if rotational DOFs contribute significantly to the dynamic response. It is possible, however, to detect damage using the translational damage indicator alone. The results also indicate that unscaled damage indicators should be preferred as they may lead to comparative estimates of the extent of damage when consecutively applied on a system with varying damage extent.

5. APPLICABILITY OF THE PROPOSED DAMAGE INDICATOR TO BUILDINGS

The aim of this chapter is to discuss the applicability and effectiveness of the damage indicator proposed in Section 2.4 to realistic civil engineering structures. To this end, 119 damage scenarios realized on a regular reinforced concrete building are simulated.

5.1. The Model Building and Damage Scenarios Considered

The numerical building model used in this chapter is a six-story reinforced concrete structure with 400 m² floor area. The original plan is symmetric regularly and equally spaced 25 columns with four spans in each direction as shown in Figure 5.1.

Slabs have no contributions to stiffness of the structure but work as diaphragms. Reduction factors of gross moments of inertia of beams and columns are assigned according to ACI 318S-05 Design Code. Columns have 60 cm x 60 cm dimensions and beams have 30cm x 50cm dimensions. Beam-column connection zones are rigid. Concrete grade used in structure is C25. Figure 5.2 schematically shows the elevation and the cross sections of the beams and the columns.

The damage introduced is defined as a decrease in the modulus of elasticity of the target column(s). Damage scenarios considered herein may be classified under four categories:

- Category I: Single Column Damaged
- Category II: Nine Columns Damaged
- Category III: All Columns Damaged at a Single Story
- Category IV: All Columns Damaged at Multiple Stories

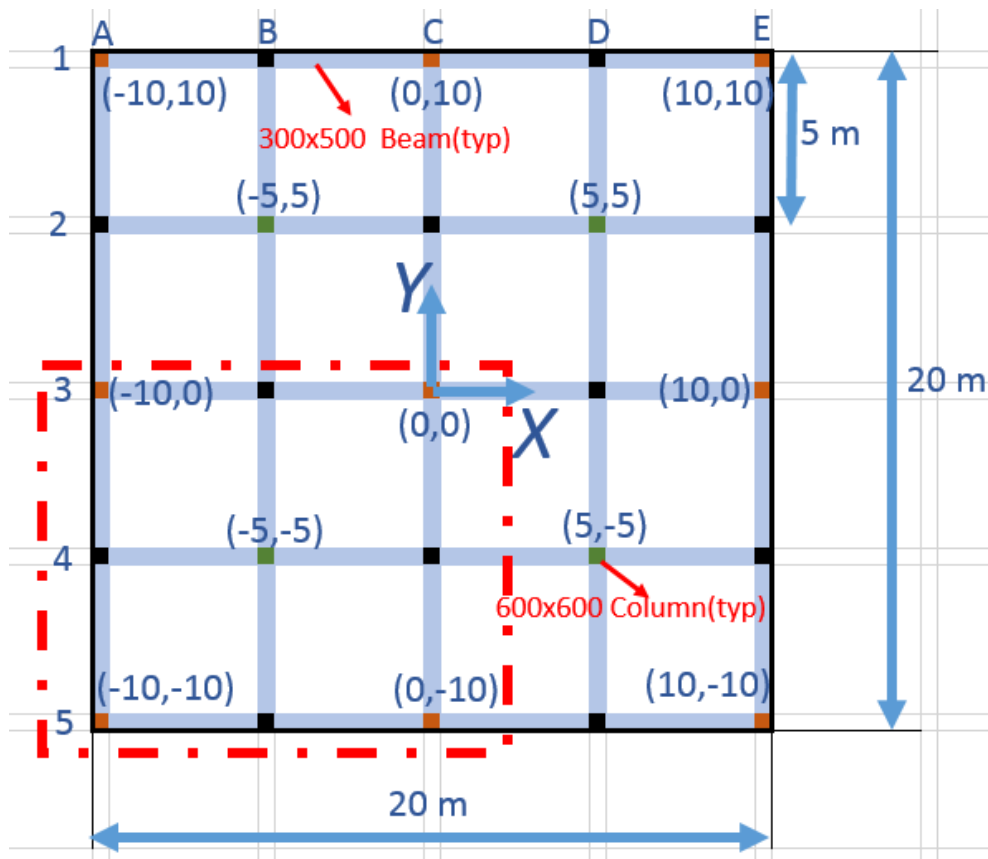


Figure 5.1. Typical floor plan.

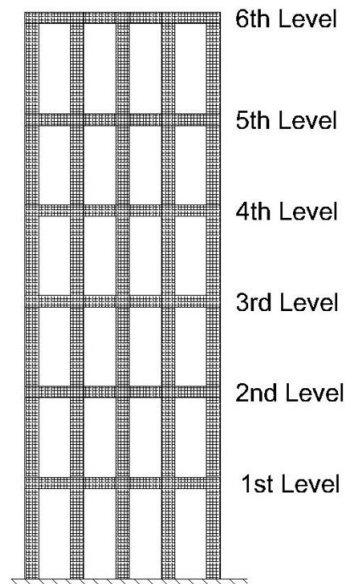


Figure 5.2. Elevation of the six story building.

First three categories are related to single story and the last item is related to multiple damage locations. Category I comprises 50% or 100% drop in the modulus of elasticity of a single target column. Category II comprises 25%, 50%, 75% or 100% simultaneous reduction in the moduli of elasticity of all (neighboring) nine columns. The remaining two categories address two levels: 10% damage corresponds to moderate damage and 90% damage corresponds to severe damage. Only in the last four scenarios in which all columns are considered damaged four levels corresponding to 10%, 40%, 60%, 90 % damage are investigated.

To provide a concise summary of the excessive number of scenarios considered, Tables 5.1-5.4 are presented. In these tables, the number of the damage scenario is given as dependent on variable N , which denotes the floor number. Therefore, the cases in which a single column on the 6th floor is damaged correspond to damage scenarios (DS # column) $(6-1)*9+1$ to $6*9$, i.e. to damage scenarios 46 to 54, The coordinates of the damages element, in reference to Figure 5.1, is given under column “Number of Damaged Elements and Damaged Zone Center” along with the number of damaged elements. The damage intensity associated with a particular case is provided under column “Reduced Stiffness of the Element” wherein the ratio of the post-damage modulus of elasticity (E_d) to the initial modulus of elasticity (E_i) is presented. To provide an example for a case in which multiple columns are damaged, $N = 1$ in Table 5.2 corresponds to the 58th scenario, in which 9 neighboring columns of the first floor ($N = 1$) located at the intersection of axes A, B, C and 3, 4, 5 as shown in Figure 5.2 with the central column located at coordinates [-5m, -5m] (hence the notation ‘9C(-5,-5)’ with 9 indicating the number of damaged columns and C(-5,-5) referring to the location of the central column in reference to the plan given in Figure 5.2).

Table 5.1. Damage scenarios for Category I (single column damage on a single story).

Damage Scenario Number	Story Level	Number of Damaged Elements and Damaged Zone Center	Damage Location At the Level	Reduced Stiffness of the Element (E_d/E_i)	Is Damage Symmetric
N*9-8	N	1C(0,0)	Middle	0	Yes
N*9-7	N	1C(10,0)	Edge	0	No
N*9-6	N	1C(-10,0)	Edge	0.5	No
N*9-5	N	1C(0,10)	Edge	0	No
N*9-4	N	1C(0,-10)	Edge	0.5	No
N*9-3	N	1C(-10,10)	Corner	0	No
N*9-2	N	1C(10,10)	Corner	0.5	No
N*9-1	N	1C(10,-10)	Corner	0	No
N*9	N	1C(-10,-10)	Corner	0.5	No

Table 5.2. Damage scenarios for Category II (nine neighboring columns damaged on a single story).

Damage Scenario Number	Story Level	Number of Damaged Elements and Damaged Zone Center	Damage Location At the Level	Reduced Stiffness of the Element	Is Damage Symmetric
51+4*N	N	9C(5,5)	Corner	0	No
52+4*N	N	9C(-5,5)	Corner	0.25	No
53+4*N	N	9C(5,-5)	Corner	0.5	No
54+4*N	N	9C(-5,-5)	Corner	0.75	No

Table 5.3. Damage scenarios for Category III (all columns damaged on a single story).

Damage Scenario Number	Story Level	Number of Damaged Elements and Damaged Zone Center	Damage Location At the Level	Reduced Stiffness of the Element	Is Damage Symmetric
78+N	N	25C(0,0)	All Columns	0.1	Yes
84+N	N	25C(0,0)	All Columns	0.9	Yes

Table 5-4 Damage scenarios for Category VI (all columns damaged on a multiple stories).

DS #	Story Level	Damaged Element/ Story (DE)	Damage Location At the Level	Reduced Stiffness of the Element	Is Damage Symmetric
91	1,2	25C(0,0)	All Columns	0.1	Yes
92	1,3	25C(0,0)	All Columns	0.1	Yes
93	1,5	25C(0,0)	All Columns	0.1	Yes
94	2,4	25C(0,0)	All Columns	0.1	Yes
95	3,6	25C(0,0)	All Columns	0.1	Yes
96	4,5	25C(0,0)	All Columns	0.1	Yes
97	1,6	25C(0,0)	All Columns	0.1	Yes
98	2,6	25C(0,0)	All Columns	0.1	Yes
99	1,2,3	25C(0,0)	All Columns	0.1	Yes
100	1,2,4	25C(0,0)	All Columns	0.1	Yes
101	1,2,5	25C(0,0)	All Columns	0.1	Yes
102	1,2,6	25C(0,0)	All Columns	0.1	Yes
103	2,4,6	25C(0,0)	All Columns	0.1	Yes
104	3,4,5	25C(0,0)	All Columns	0.1	Yes
105	4,5,6	25C(0,0)	All Columns	0.1	Yes
106	2,3,4	25C(0,0)	All Columns	0.1	Yes
107	1,3,5,6	25C(0,0)	All Columns	0.1	Yes
108	1,4,5,6	25C(0,0)	All Columns	0.1	Yes
109	2,3,4,6	25C(0,0)	All Columns	0.1	Yes
110	2,4,5,6	25C(0,0)	All Columns	0.1	Yes
111	3,4,5,6	25C(0,0)	All Columns	0.1	Yes
112	1,2,3,4	25C(0,0)	All Columns	0.1	Yes
113	1,2,3,4,5	25C(0,0)	All Columns	0.1	Yes
114	2,3,4,5,6	25C(0,0)	All Columns	0.1	Yes
115	1,2,3,4,6	25C(0,0)	All Columns	0.1	Yes
116	All	25C(0,0)	All Columns	0.1	Yes
117	All	25C(0,0)	All Columns	0.4	Yes
118	All	25C(0,0)	All Columns	0.6	Yes
119	All	25C(0,0)	All Columns	0.9	Yes

5.2. Results Obtained via the Single Mode Damage Indicator with the First Mode

Undamaged sand damaged systems in each damage scenario are analyzed and their respective eigenvalue problems are solved, so that the first natural frequencies in X and Y direction (Figure 5.2) and their corresponding, mode shapes are evaluated at the mass center. These frequencies and mode shapes are used in Equation 2.15 to estimate the damage location.

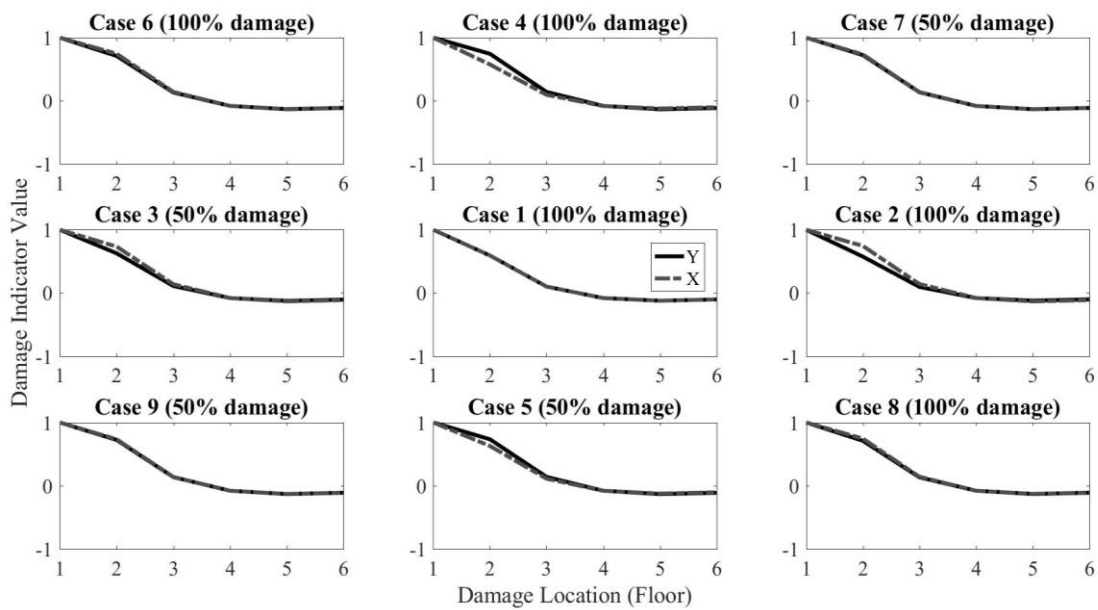


Figure 5.3. Single Column Damaged on the first story.

The results obtained via the proposed damage indicator are presented in Figures 5.3-5.14. To keep the presentation as concise as possible, these figures are divided into subplots in each of which resides a particular damage case. To visually correlate the location of the damage, the subplots are ordered in similar fashion to the location of the damage in reference to Figure 5.2. To give an example of this correlation, Case 1 in Figure 5.3 corresponds to damage in the central column (located at $[0,0]$ in Figure 5.2) whereas Case 7 corresponds to damage in the upper-right column (located at $[10,10]$ in Figure 5.2) and Case 3 corresponds to damage in the middle-left column (located at $[-10,0]$ in Figure 5.2). Rest of the figures follow the same construction logic.

It is seen in Figures 5.3 – 5.8 that damage at a single column can be identified via the damage indicator. The details of the figures and the possible success of the approach does show small variations depending on where the damage is. In Figure 5.3, for example, it is seen that the damage indicator takes on a value of 1 at the 1st floor level but it has a value around $\frac{1}{2}$ for the 2nd floor level, which does not provide a clear cut indication of the first floor. As a single column makes very little difference to the overall structure, it is interesting to see that this tendency is almost independent of the severity of damage.

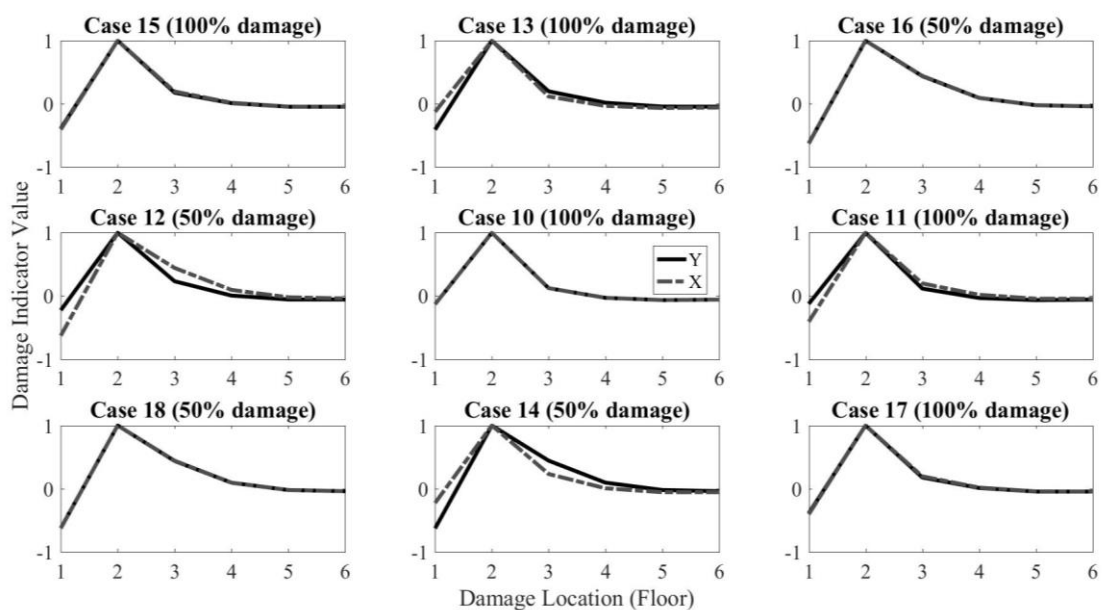


Figure 5.4. Single column damaged on the second story.

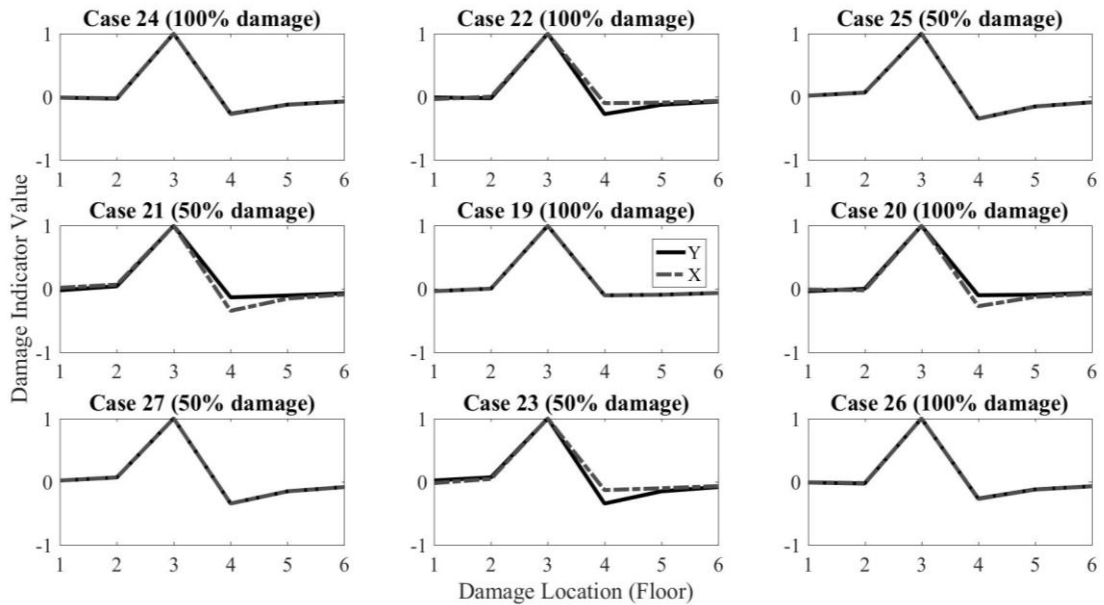


Figure 5.5. Single column damaged on the third story.

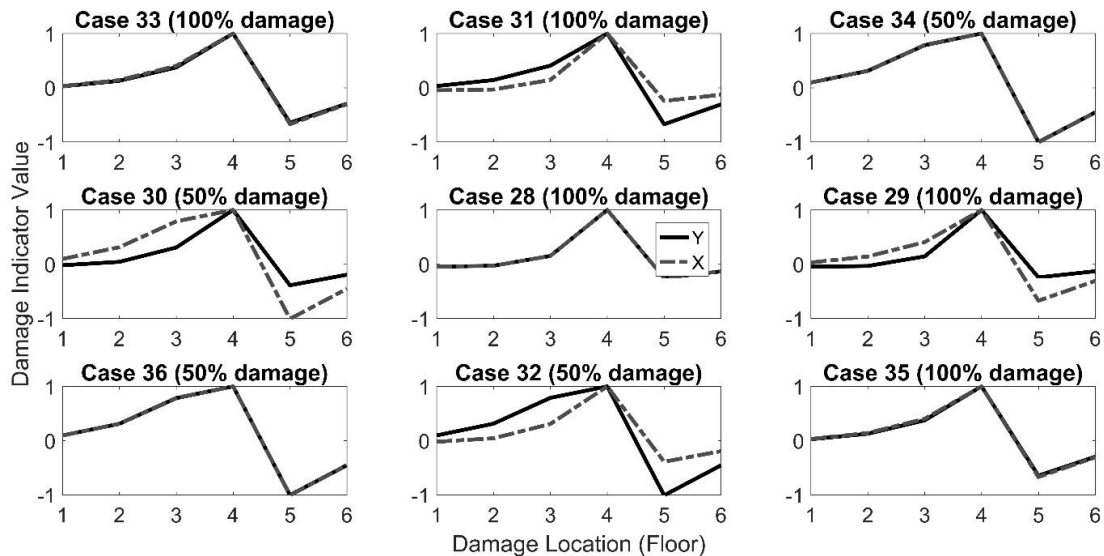


Figure 5.6. Single column damaged on the fourth story.

The results pertaining to single column damages on the second, third and fourth stories, as presented in Figure 5.4, Figure 5.5 and Figure 5.6, respectively, indicate that the damage indicator has performed acceptably well, with modes shapes along X and Y leading to slightly differing patterns. Overall, all the conclusions overlap with the correct locations, even though some cases may hint at multiple locations, especially in neighboring stories.

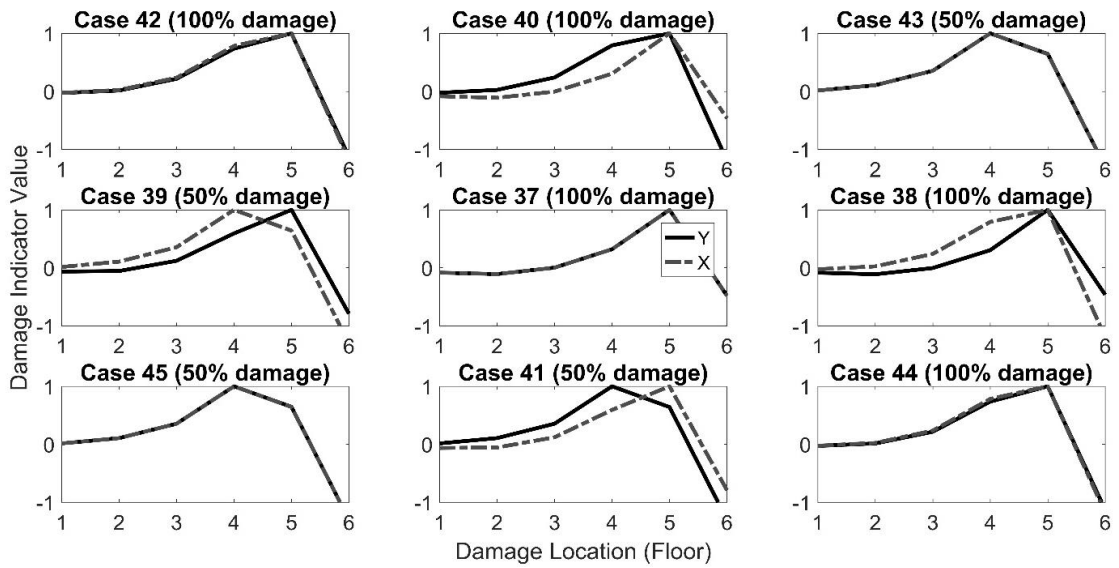


Figure 5.7. Single column damaged on the fifth story.

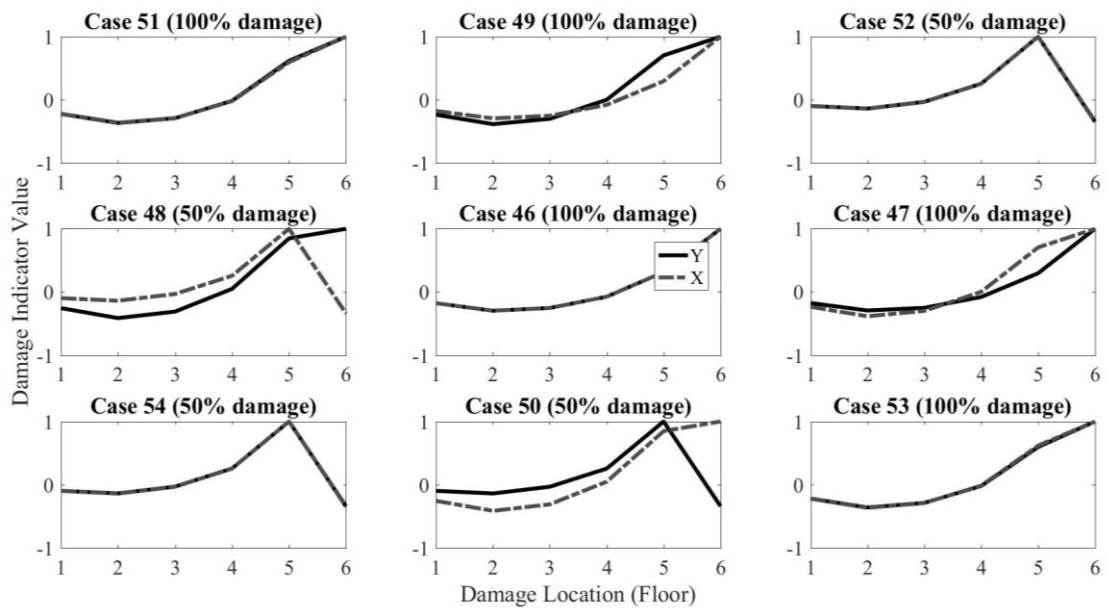


Figure 5.8. Single column damaged on the sixth story.

The cases in which a single column is damaged on the fifth and the sixth stories, however, have posed bigger challenges for the proposed indicator. It may be said that the changes in the fundamental frequencies and mode shapes caused by damage in a single column is quite limited, and further so when the damage is located on the upper floors. It is therefore not surprising that with such limited impact, Figures 5.7 and 5.8 show certain cases

in which the location is identified incorrectly: the success rate of the damage indicator is five out of nine cases for both directions and six out of nine for one direction.

On the other hand, if the damage severity is increased such that 9 columns are damaged on a given story, the proposed damage indicator has shown satisfactory performance in all cases pertaining to the first-five floors as shown in Figures 5.9-5.13. Once again, the cases associated with the sixth story pose bigger problems due to their limited impact on the fundamental frequencies and mode shapes. It is seen in Figure 5.14 that in 2 out of the 4 cases considered, the damage locations have been falsely identified as the 5th story instead of the 6th story. It is also noteworthy that in cases in which the damage indicator is successful, the reductions in stiffness due to damage are 100% and 75%, whereas in those cases in which the damage indicator is in error, these reductions are 50% and 25%. Furthermore, the trends observed in all cases pertaining to 9 columns being damaged are similar for both directions.

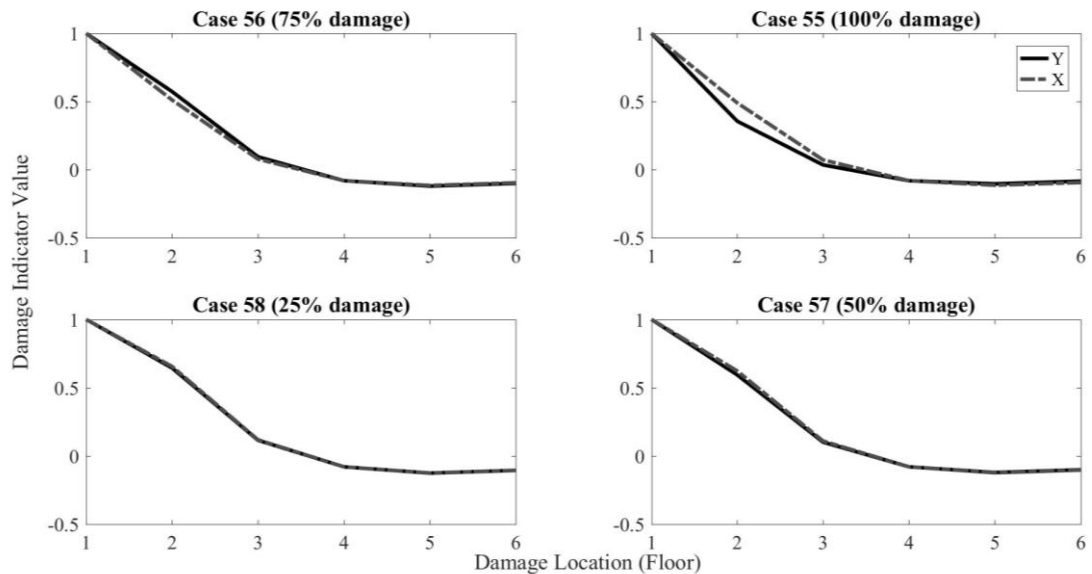


Figure 5.9. Nine columns damaged on the first story.

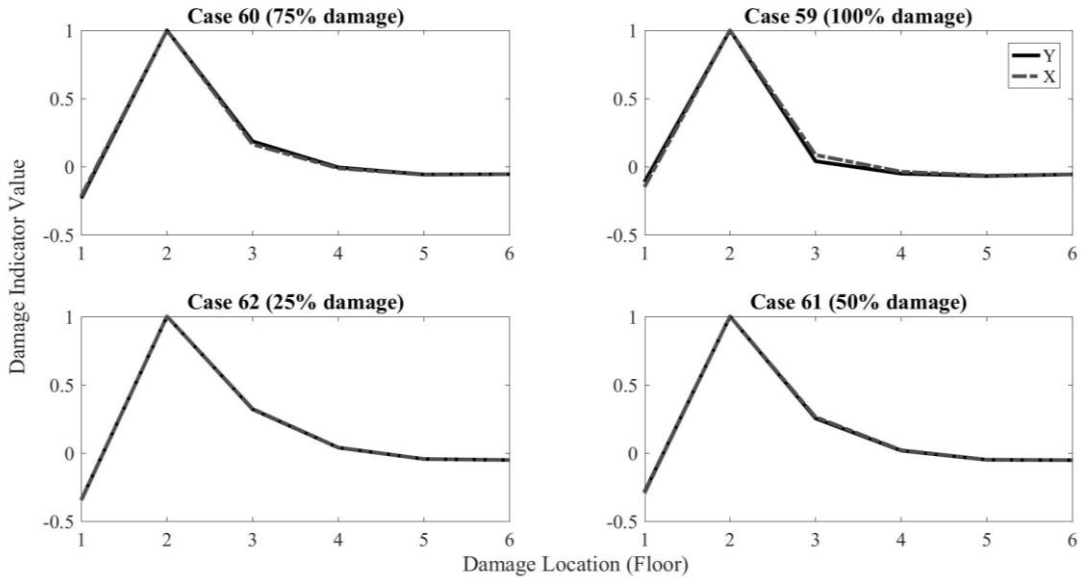


Figure 5.10. Nine columns damaged on the second story.

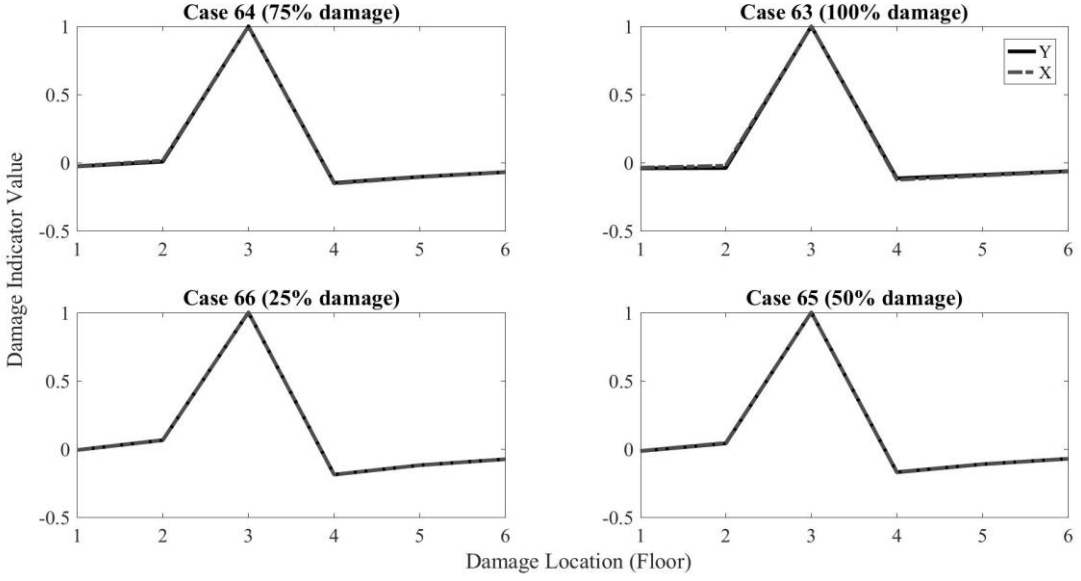


Figure 5.11. Nine columns damaged on the third story.

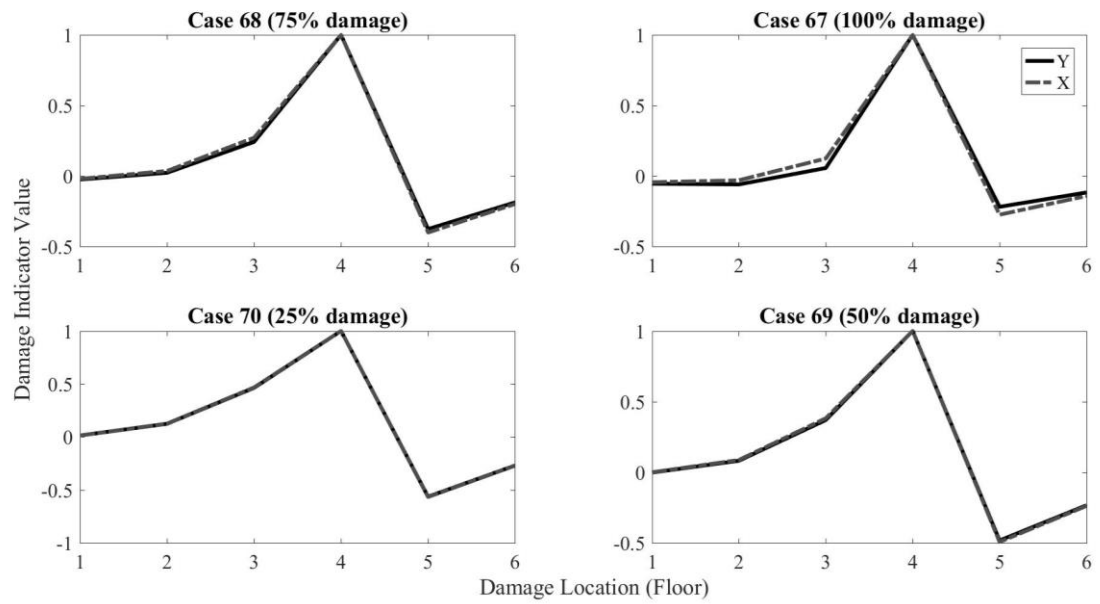


Figure 5.12. Nine columns damaged on the fourth story.

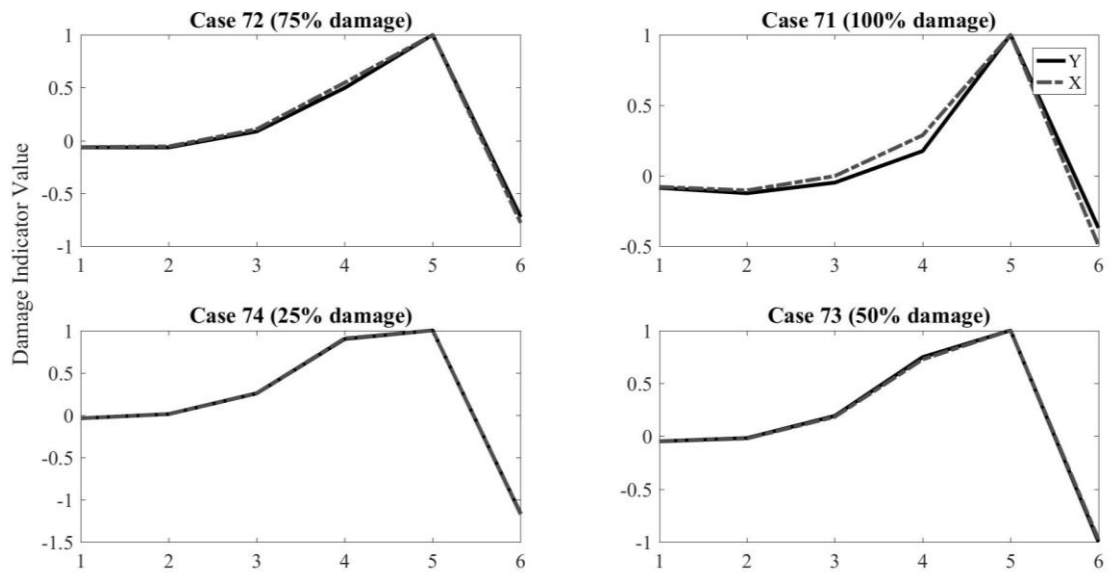


Figure 5.13. Nine columns damaged on the fifth story.

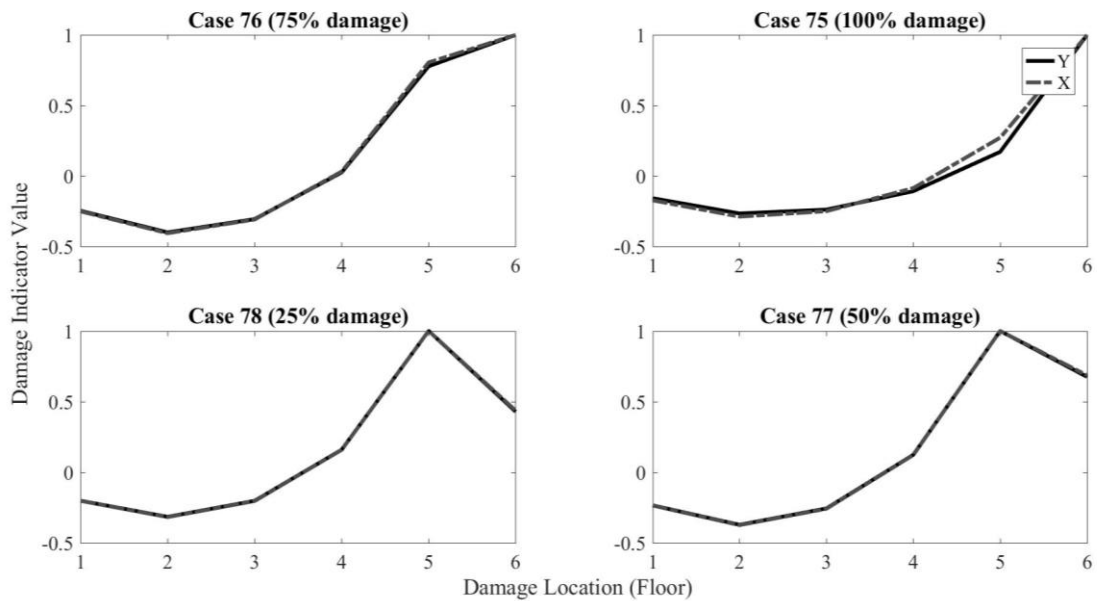


Figure 5.14. Nine columns damaged on the sixth story.

In the extreme case of having all columns damaged on a story, the performance of the proposed damage indicator is strongly correlated with the damage severity. For severe damage cases corresponding to 90% stiffness reduction, the proposed indicator can clearly identify the location. In the case of mild to moderate damage, as for example in the cases corresponding to 10% 10% reduction in stiffness, the proposed indicator yields some false positive results in the sense that the damage is located on adjacent story as opposed to the correct one. Relevant results are provided in Figures 5.15 and 5.16.

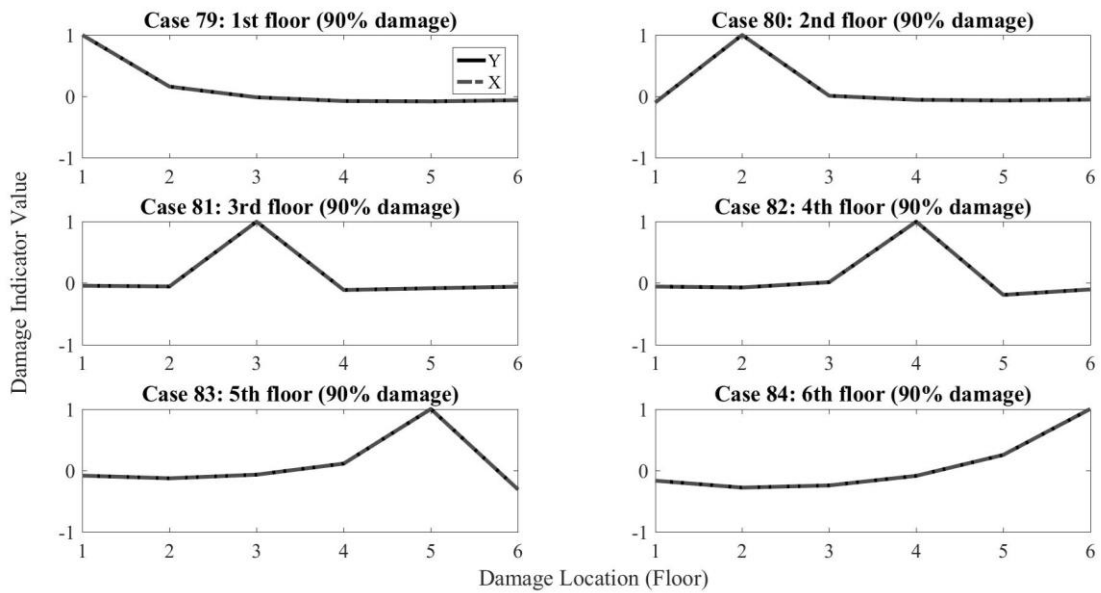


Figure 5.15. All columns severely damaged on a single floor.

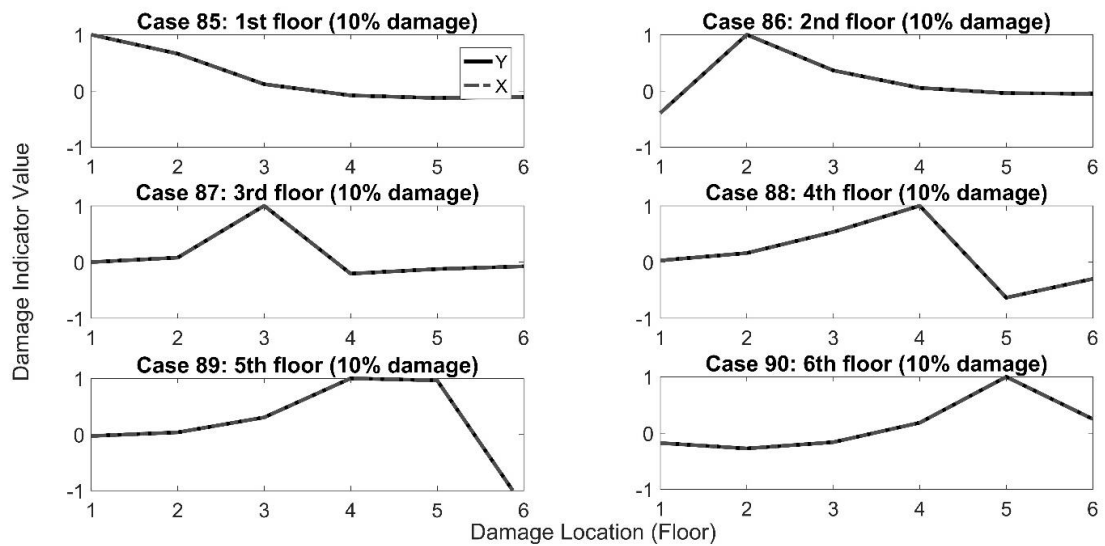


Figure 5.16. All columns mildly damaged on a single floor.

The observations related to cases in which damage occurs on a single story resurface when multiple damage locations (i.e. damage on a number of different stories) are considered. Figures 5.17 – 5.21 show results pertaining to those cases in which columns are severely damaged simultaneously on two or three floors. These results indicate that even when multiple locations are in effect, the proposed damage indicator may successfully be

employed to locate the damaged stories, especially if the stories are located around the mid-level of the building. As before, cases involving the last two stories are more prone to errors.

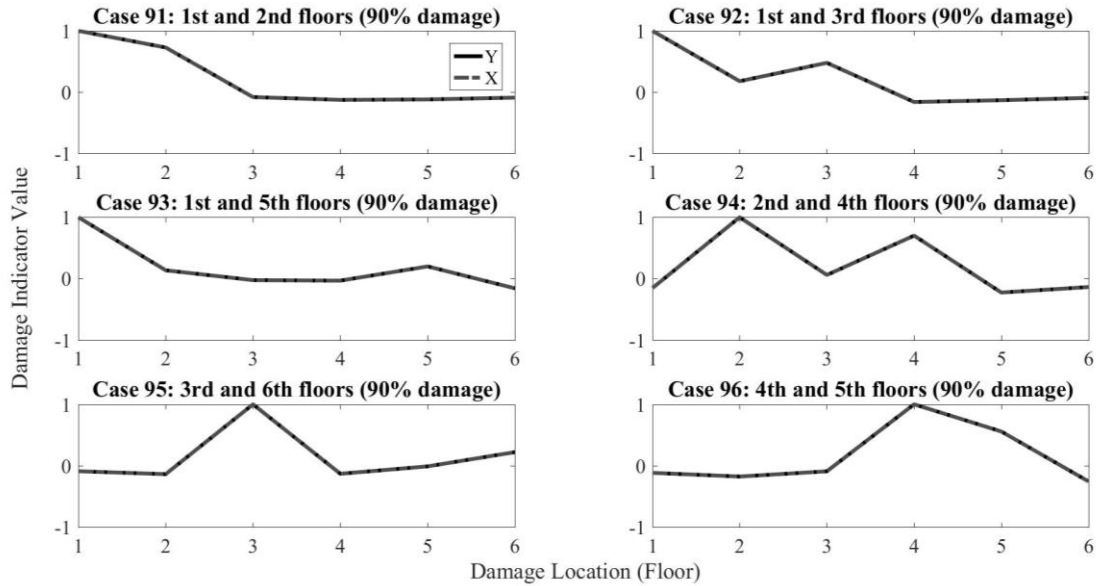


Figure 5.17. All columns severely damaged on two different stories.

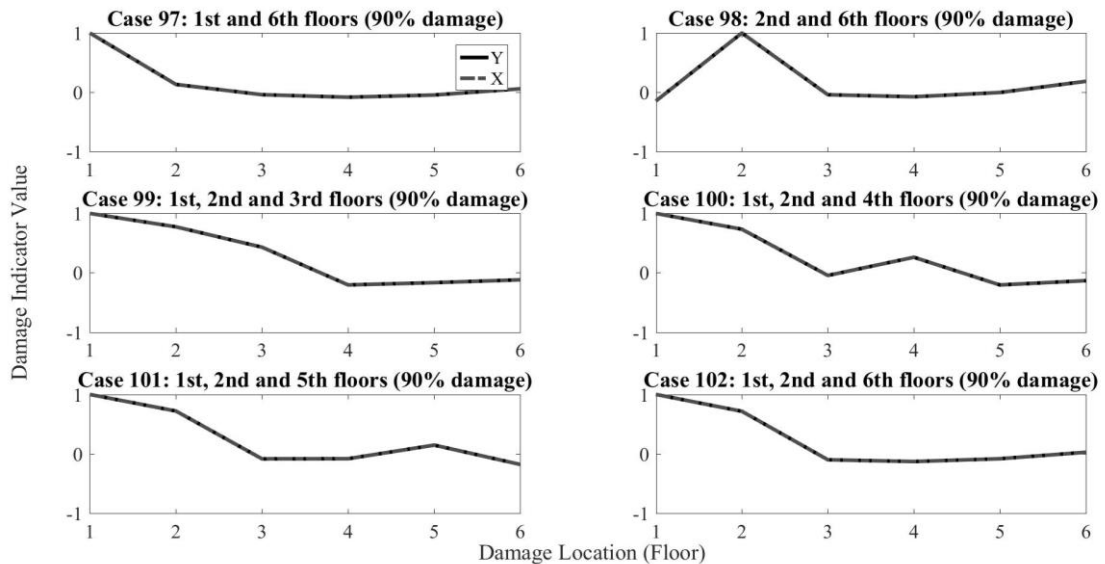


Figure 5.18. All columns severely damaged on two or three different stories.

It is important to note that as the number of locations increase, and in the final case reach the level that damage is simultaneously on all stories, the proposed indicator can no

longer lead to meaningful results. In essence, the proposed indicator is a ‘local’ tool and when the damage is distributed its effectiveness is lost.

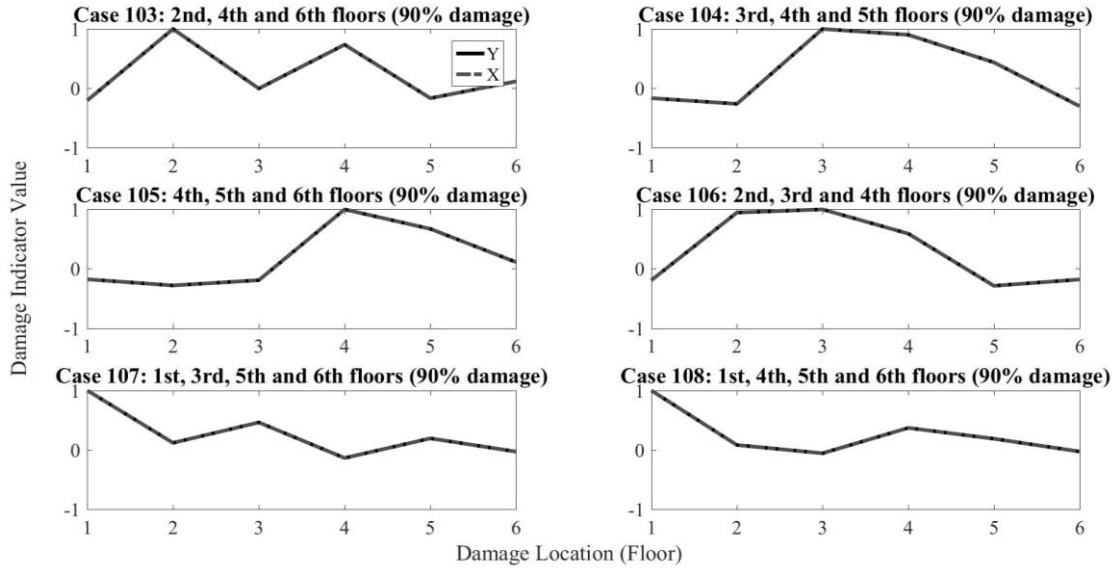


Figure 5.19. All columns severely damaged on three or four different stories.

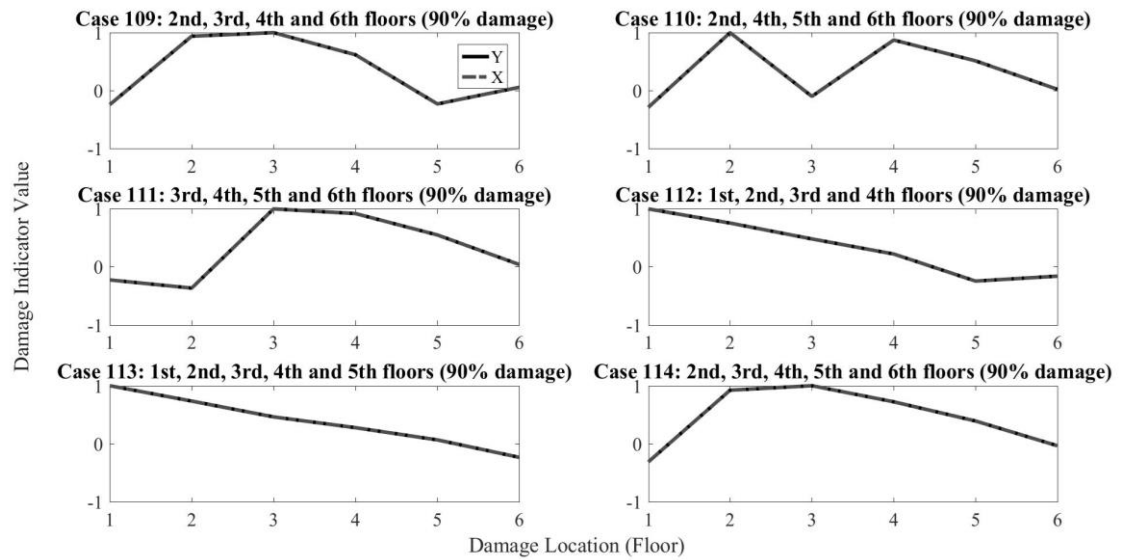


Figure 5.20. All columns severely damaged on four or five different stories.

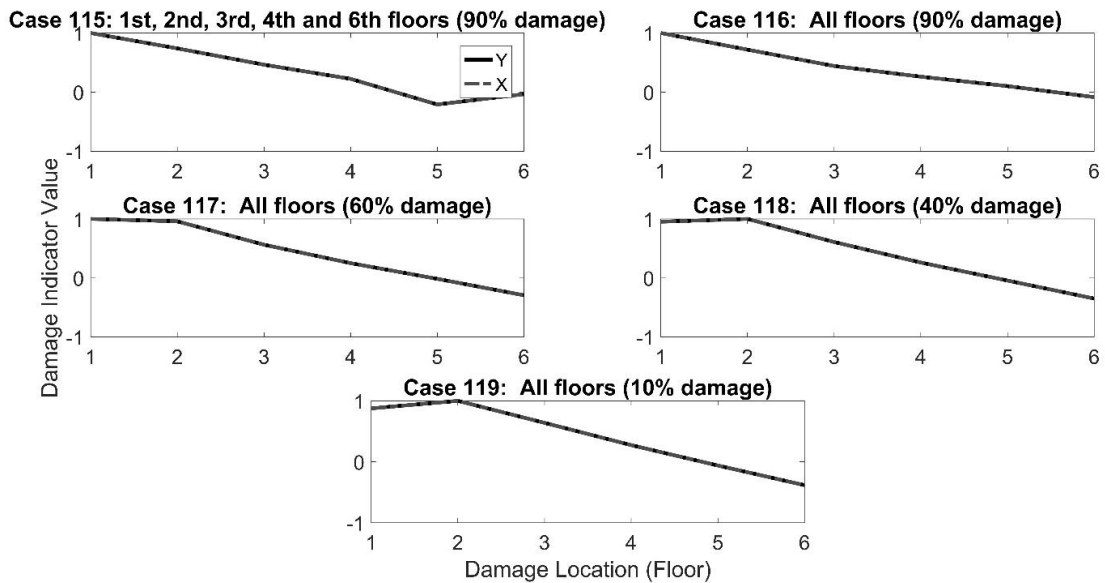


Figure 5.21. All columns severely damaged on five or six different stories.

5.3. Results Obtained via the Single Mode Damage Indicator with the Second and Third Modes

The previous analysis is replicated in this section by using the second and the third modes. The aforementioned procedure is used also in these cases for calculating the natural frequencies and the mode shapes of the second and the third modes at the mass center of the stories. For ease of comparison with the previous case, only some of the results related to the first, the third and the sixth stories are exhibited here.

In the first case, the performance of the single mode damage indicator using the second mode is analyzed. It is known from the previous studies of Sections 2.5 and 4.3 that saddle points hinder the proposed damage detection method. The saddle point of the second mode for this structure is between the third and the fourth floors, and thereby it is expected to affect the damage indicator in relation to the fourth story. The results in Figures 5.22 to 5.24 show that this indeed turns out to be the case as the damage indicator is affected by the saddle point such that a local peak occurs on the fourth story in the damage indicator estimates. Consequentially, the damage scenarios related to the third story cannot be detected by the second mode damage indicator. For the other damage scenarios related to first and sixth

story, the damage location is detected by this parameter in the sense that the largest peak occurs at the correct location even though erroneous peaks are still present.

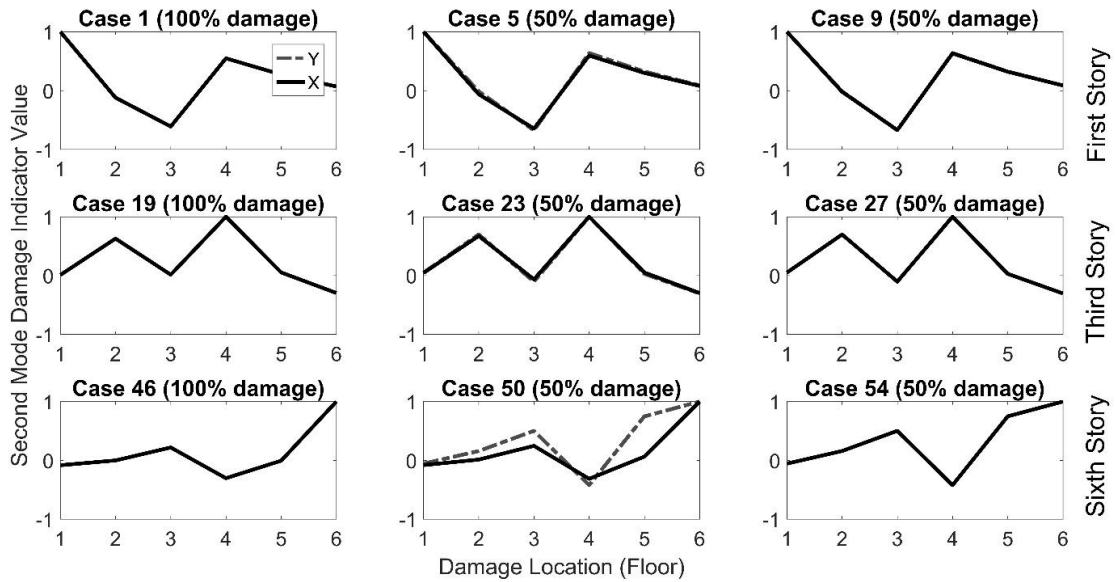


Figure 5.22. Damage detection for scenarios in which a single column is damaged on a single floor via the single mode damage indicator using the second mode.

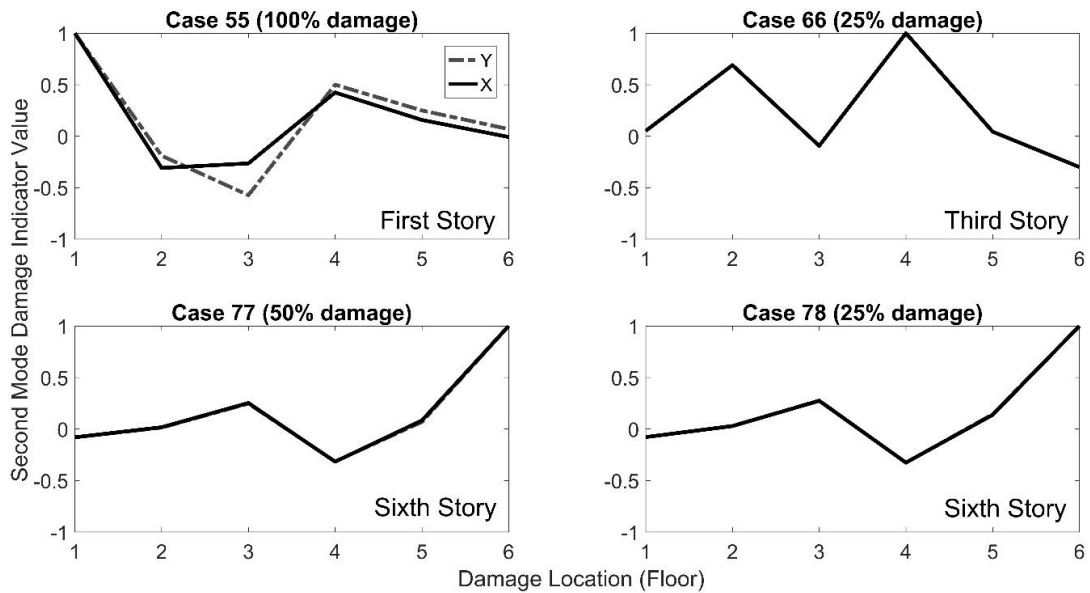


Figure 5.23. Damage detection for scenarios in which nine columns are damaged on a single floor via the single mode damage indicator using the second mode.

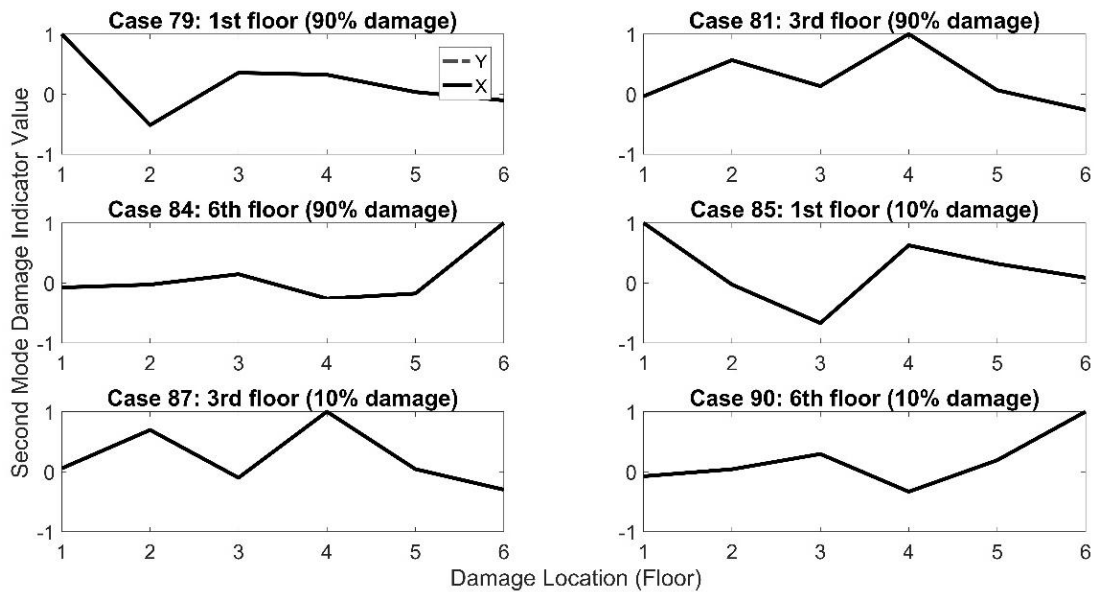


Figure 5.24. Damage detection for scenarios in which all columns are damaged on a single floor via the single mode damage indicator using the second mode.

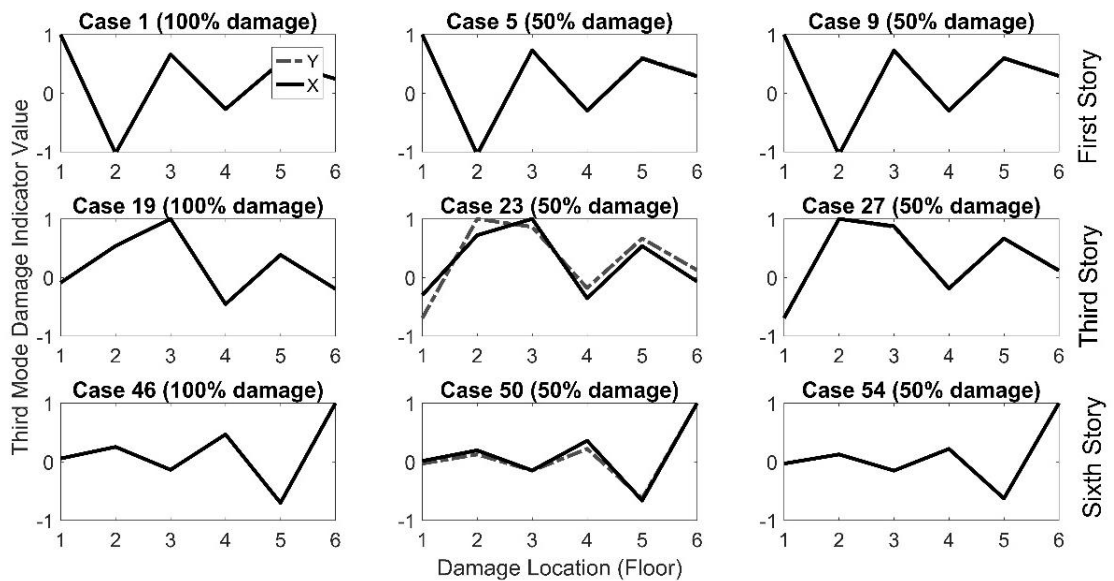


Figure 5.25. Damage detection for scenarios in which a single column is damaged on a single floor via the single mode damage indicator using the third mode.

As far as the single mode damage indicator using the third mode is concerned, the saddle points of the third mode are related to the third and fifth floors. The results in Figures

5.25 to 5.27 show that damage detection is affected by the presence of these saddle points as the damage indicator shows local peaks on the third and the fifth floors. The damage scenarios related to the third story are correctly identified by the third mode damage indicator with only 50% success. For the other damage scenarios related to the first and the sixth stories, the damage location is detected more accurately by this parameter even though the local peaks persist.

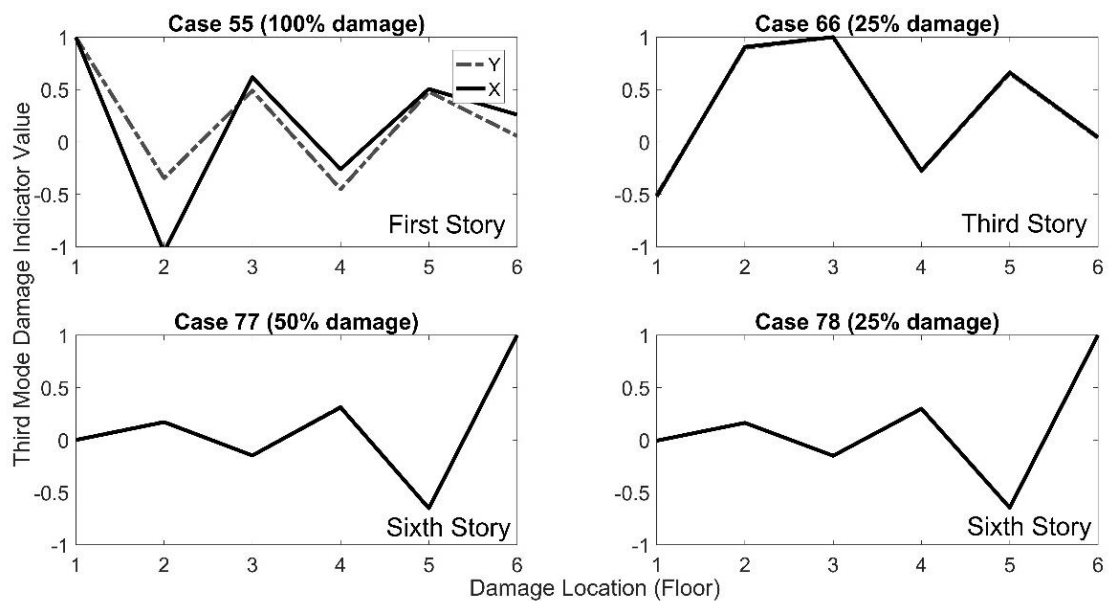


Figure 5.26. Damage detection for scenarios in which nine columns are damaged on a single floor via the single mode damage indicator using the third mode.

Compared with the case of the single mode damage indicator using the first mode, the use of the second and the third modes are seen to slightly increase the success rate pertaining to damage cases concerning the sixth story. On the other hand, when overall results are considered, the use of the first mode in the single mode damage indicator is seen to yield a higher confidence level.

As far as damage scenarios encompassing multi floors are concerned, the effect of saddle points on the damage indicator is observed similarly to the single story scenarios. In Figure 5.28, the local peaks coinciding with the saddle points yield false positive results. For

this example in which there are only six stories, the results pertaining to damage scenarios concerning multiple stories are negatively affected and unreliable.

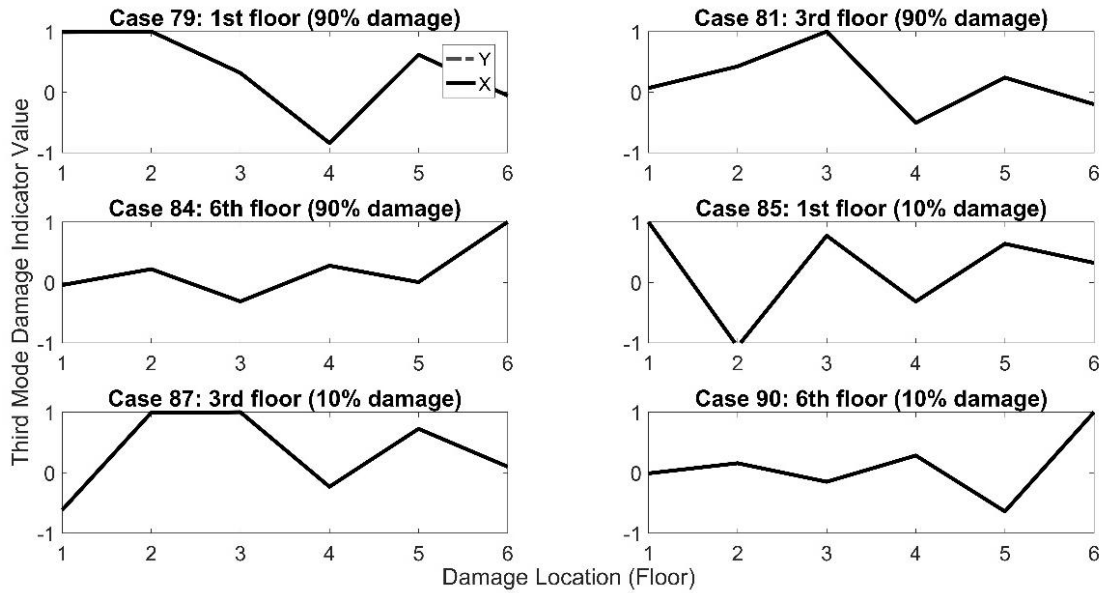


Figure 5.27. Damage detection for scenarios in which all columns are damaged on a single floor via the single mode damage indicator using the third mode.

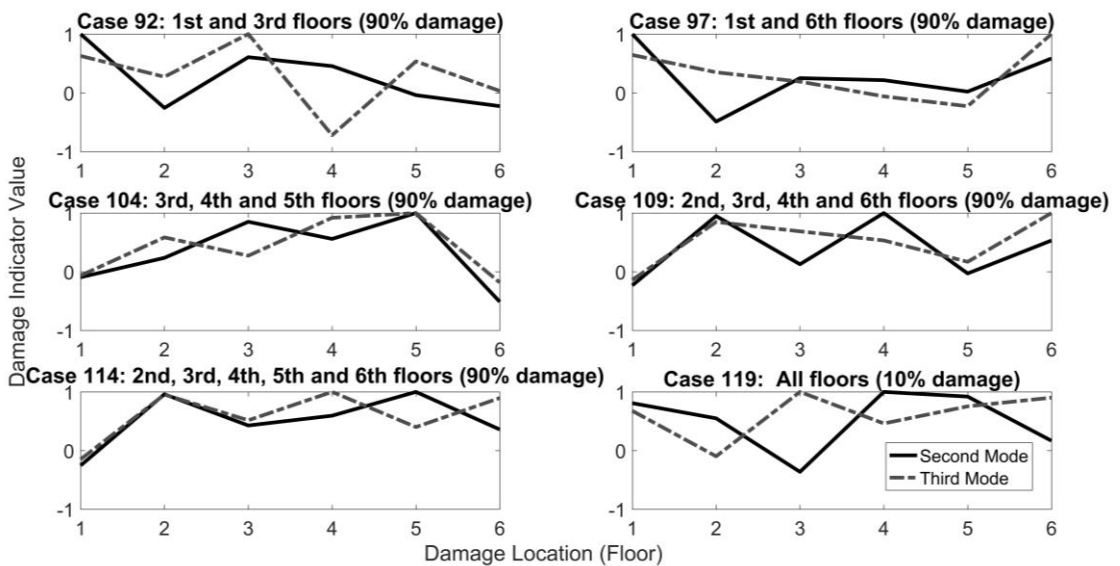


Figure 5.28. Damage detection for scenarios in which all columns are damaged on a single floor via the single mode damage indicator using the second and the third modes.

5.4. Results Obtained via the Multi-Mode Damage Indicator with the First Three Modes

It was observed in the previous sections that the first mode is susceptible to false alarms when damage occurs at the tip of the structure but that it is a reliable indicator for those cases in which damage occurs elsewhere. The second and the third modes, on the other hand, have shown better performance in estimating the damage when it is located at the tip of the structure whereas they have been significantly prone to false alarms around the saddle points. In order to overcome these disadvantages observed in the single mode damage indicator, the multi-mode damage indicator is investigated in this section. The multi-mode damage indicator is calculated by summing the unscaled damage indicator values of the first three modes. The results obtained for various damage scenarios are displayed in Figures 5.29 to 5.31.

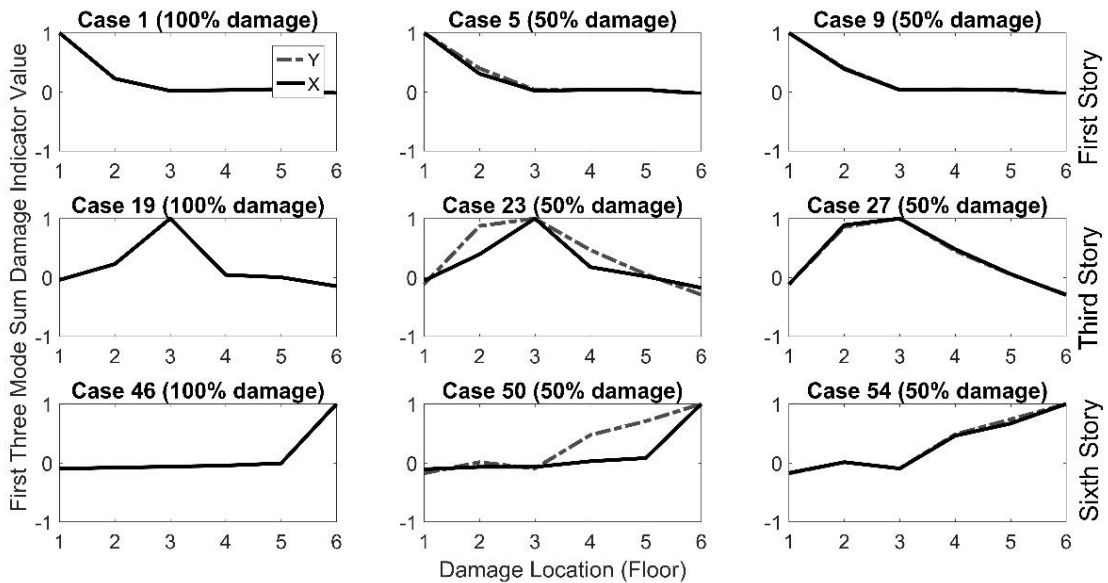


Figure 5.29. Damage detection for scenarios in which a single column is damaged on a single floor via the multi-mode damage indicator using the first three modes.

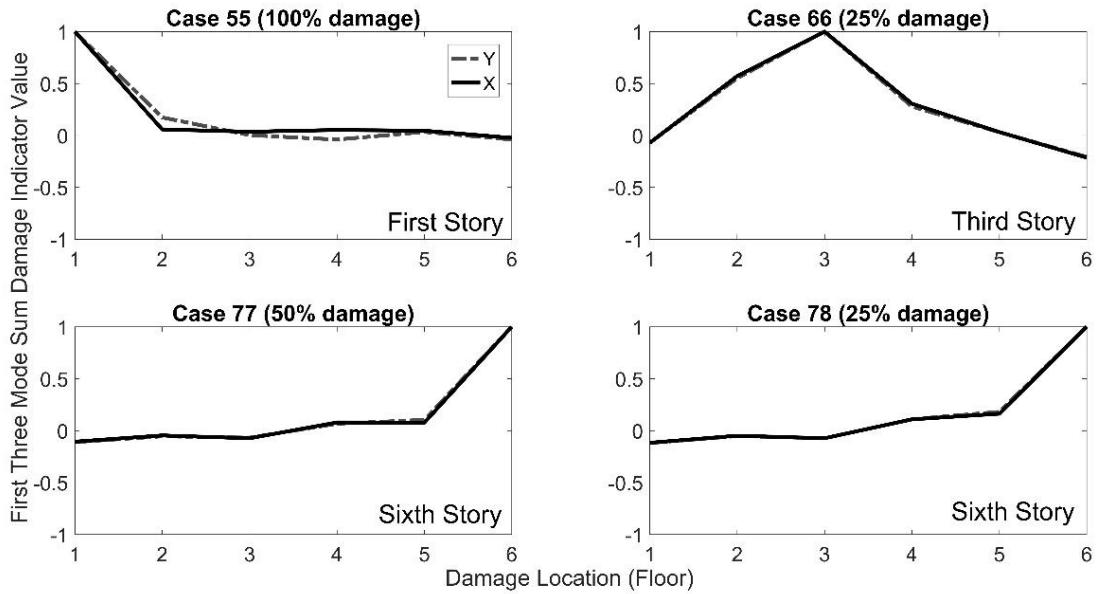


Figure 5.30. Damage detection for scenarios in which nine columns are damaged on a single floor via the multi-mode damage indicator using the first three modes.

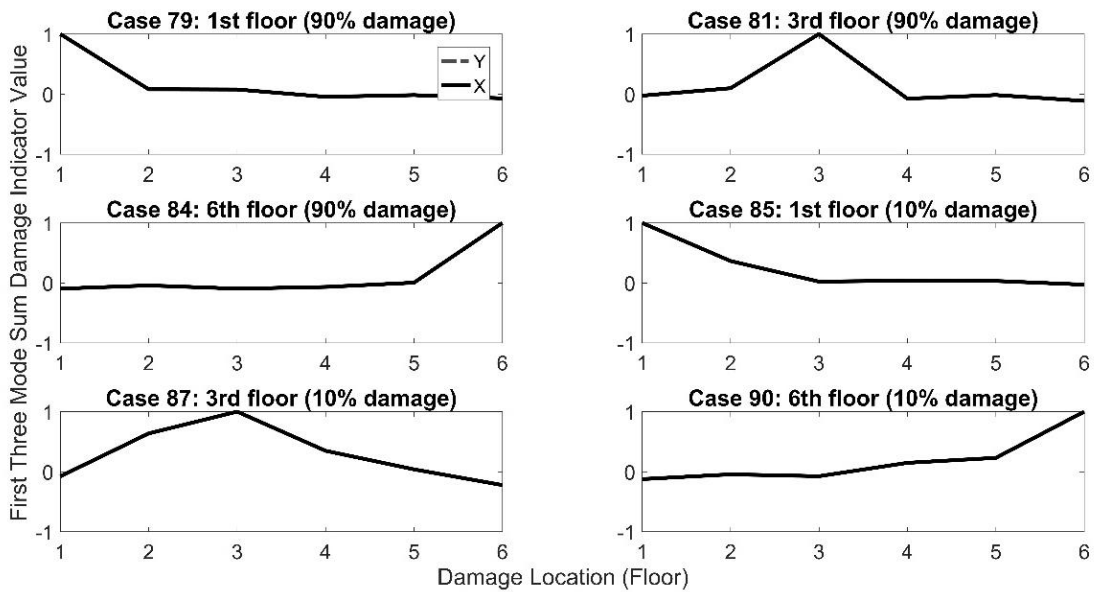


Figure 5.31. Damage detection for scenarios in which all columns are damaged on a single floor via the multi-mode damage indicator using the first three modes.

The multi-mode damage indicator is seen to have better success compared to the single mode indicator in detecting the actual damage locations in the damage scenarios considered.

The disadvantages of each single mode indicator discussed in the previous sections are seen to have been overcome by using a cumulative approach. Neither sets of saddle points pertaining to the second and the third mode indicators have noticeable adverse effects, and false positives are not encountered. Based on the analyses so far, it may be recommended that either the multi mode damage indicator and or the single mode damage indicator with the first mode is used for when damage is expected to be localized on a single story.

Finally, Figure 5.32 shows the results obtained, using the multi-mode damage indicator with the first three modes and the single mode damage indicator with the first mode, for some of the scenarios encompassing damage on multiple floors. The results show a slightly better performance for the multi-mode indicator, especially when damage occurs near the top end. Once again, the recommendations previously stated prevail, and overall it is recommended that both the multi mode damage indicator and the single mode damage indicator with the first mode are employed simultaneously by the analyst to further increase confidence and reliability.

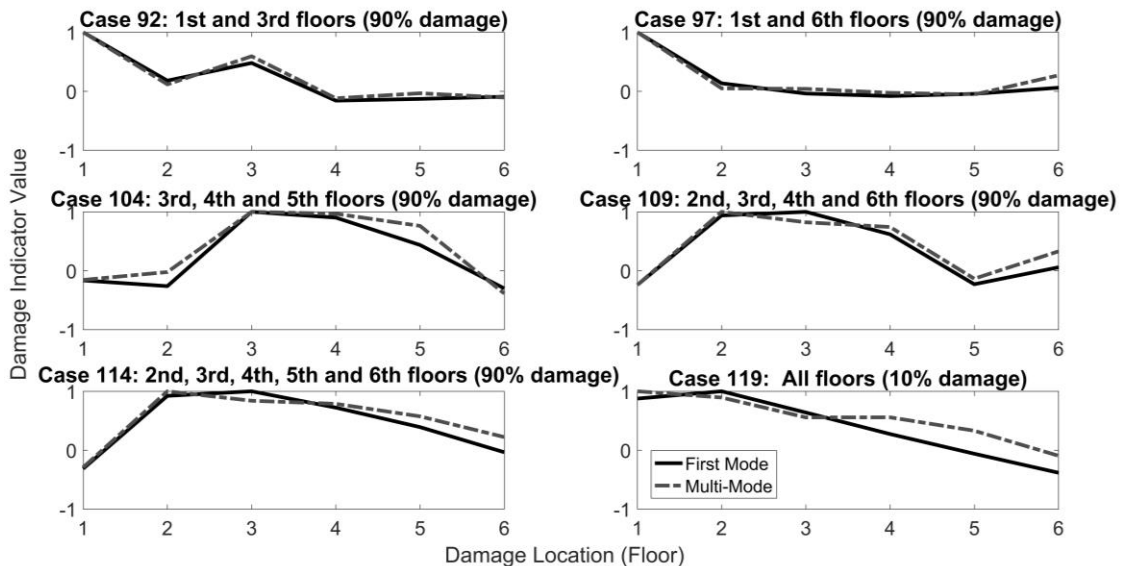


Figure 5.32. Damage detection for scenarios in which all columns are damaged on multiple floors via the multi-mode damage indicator using the first three modes.

6. ESTIMATION OF MODAL PARAMETERS FROM REAL DATA

The purpose of the chapter is to investigate the performance of the count plot methodology on real data measured on a reinforced concrete structure. In this context, data recorded as part of a project is used. Accelerometers are installed on a five story reinforced concrete structure (See Figure 6.1), and ambient vibration data is collected at different stages of demolishing. The accelerometer records used in this section are taken from two different states of the building. Eight recordings are from the undamaged building, and eight others are taken after some damage is induced. The measurements are taken from four corners on each floor for 20-25 minutes.

The accelerometers are placed as shown on the plan view of Figure 6.2. For the Undamaged State, the reference accelerometer is placed at position “A” on the fifth floor, and for the Damaged State, the reference accelerometer is placed on position “B”. Other accelerometers are travelling in the sense that data is taken from a given floor for a sufficient duration and the accelerometers are then moved to another floor while keeping the reference sensor unmoved. For the analyses reported in this section, only the measurements for the accelerometers placed on position “A” at each floor are considered for the Undamaged State, and similarly for the Damaged State only the measurements collected on position “B” at every floor are used.

The damage in this particular case pertains to demolition of three columns of the first story and one beam connecting two of the demolished columns, as shown in Figure 6.1. Columns and beams were destroyed by the JCB Hydraulic Rock Breaker device. The project is about the damage scenarios as follows:



Figure 6.1. The reinforced concrete building investigated and the structural elements removed to induce damage.

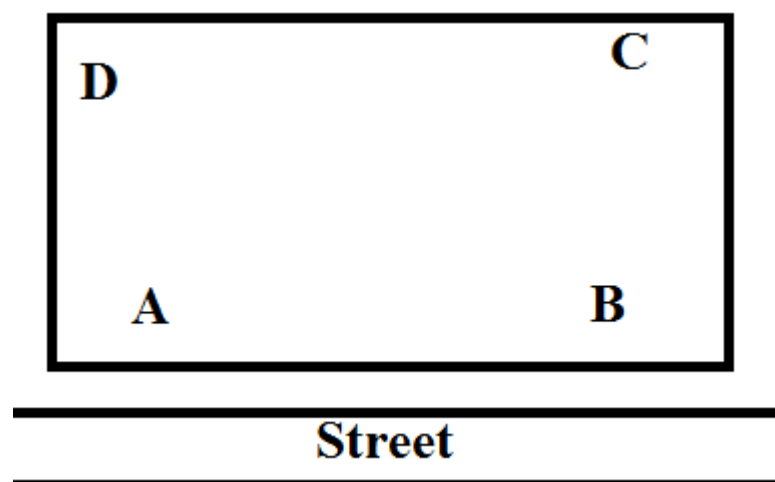


Figure 6.2. Accelerometer locations on a floor, plan view.

1. One column is severely damaged
2. Three columns are severely damaged
3. Three columns are damaged severely and a beam is demolished
4. One column and beam are demolished, two columns severely damaged.
5. Three columns and beam are demolished.

Since damage cannot be retrieved back, the damage scenarios are cumulative. In this study, the undamaged and damage scenario five is considered in order to evaluate the natural frequency changes due to damage by utilizing count plots. For ease of reference, the initial state will be simply referred to as the Undamaged State, and the post damage state will be referred to as the Damaged State.

The initial step undertaken is to conduct a preliminary investigation regarding the quality of the data. No trend is observed in the signal. However some impact type effects and some environmental effect based noise are observed in the data. Since data with five minute duration is proper for the identification step, for 20-25 minute records only five minute continuous measurements which does not contain impact type effects are selected. For the data especially for the first and third story post damage measurements, the environmental noise is serious which result in selection of two minutes and lower continuous measurements from 20-25 minute records. For the 1st story measurements, 0.8, 1.2, 1.6, 2.5 minute durations are used, and for the third story measurements, 1.1, 1.2 and 1.5 minute durations are used. The power spectral density estimates for the measurements used in the analyses are displayed in Figures 6.3 and 6.4. Two close peaks and one distinct peak are observed.

The first two steps described above provide preliminary information about the data and the system. In the third step, first-order dynamic models are established with the O3KID/ERA methodology. The number of observers is set to 800 in the O3KID analysis. Every acceleration measurement is analyzed separately with its corresponding 'reference' measurement. The data is divided into 25.35 seconds long, overlapping segments. For records of 3 minutes, overlap is set to 2.5 seconds, whereas for records of 5 minutes, overlap is set to 2.5 seconds. For each data segment, a total of 390 frequencies between 0-100 Hz

calculated via the identified state space models and the modal plot is constructed. To observe any variations dependent on the tolerance limit, ± 0.01 and ± 0.04 are set as tolerance limits for the modal variables, the counts for each estimate are calculated, and the count plots shown in Figures 6.5 to 6.8 are obtained.

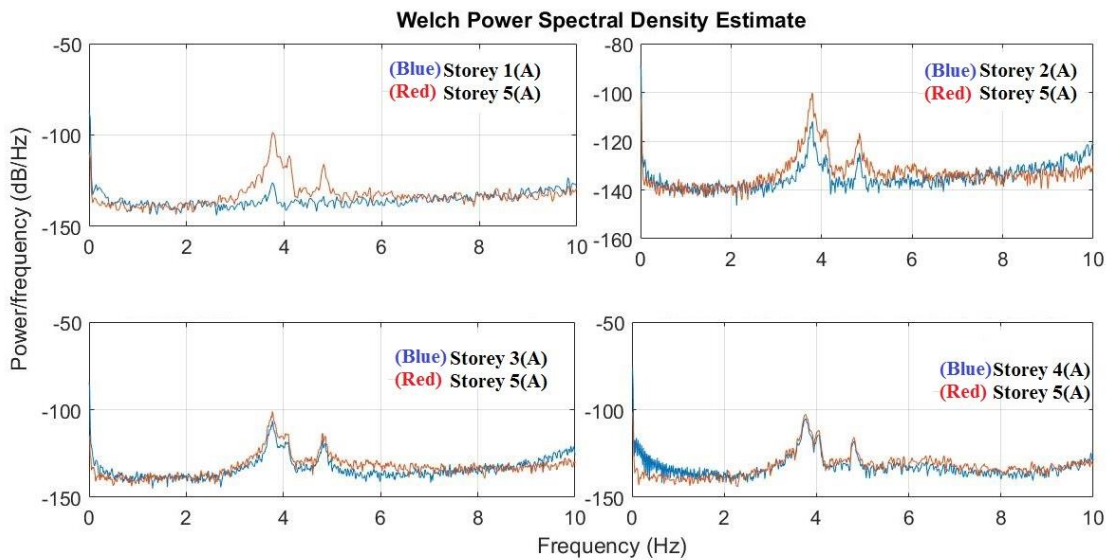


Figure 6.3. PSD estimates for the eight data sets obtained from acceleration data measured during the Undamaged State.

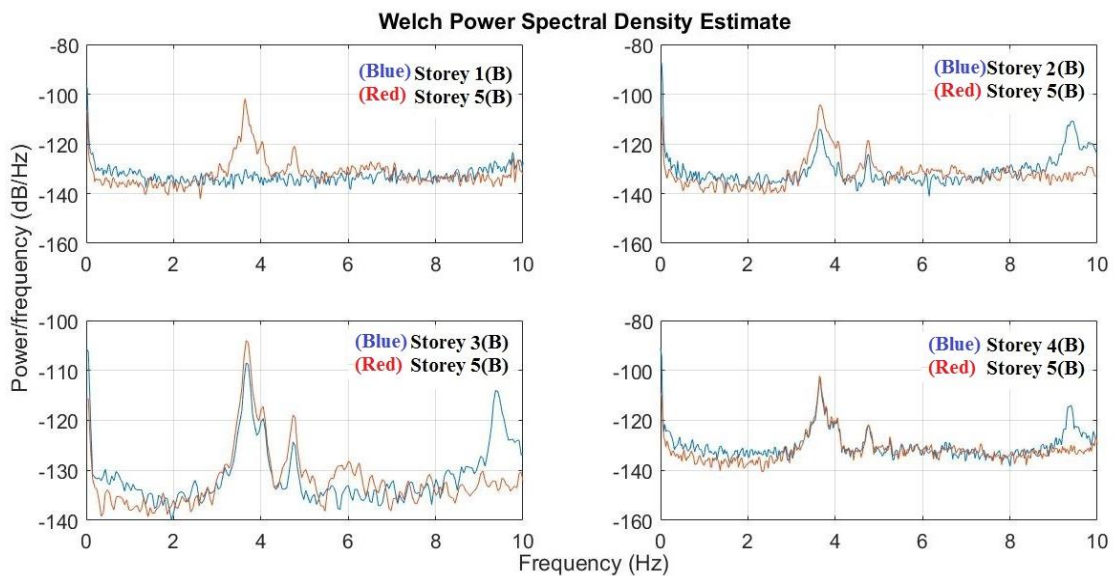


Figure 6.4. PSD estimates for the eight data sets obtained from acceleration data measured during the Damaged State.

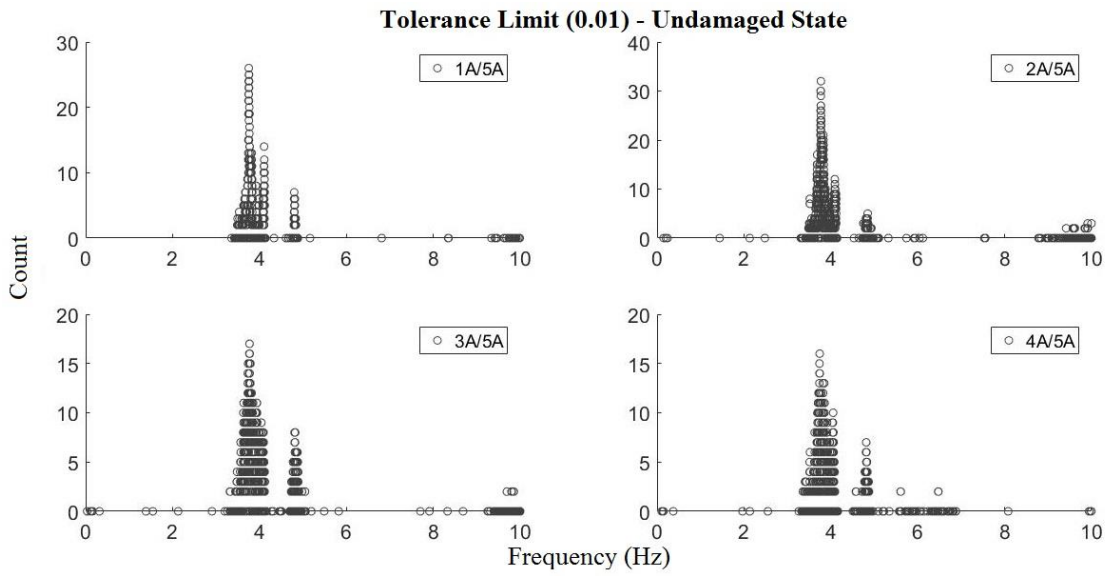


Figure 6.5. Count plot estimates for the eight data sets obtained from acceleration data measured during the Undamaged State using a tolerance limit of ± 0.01 .

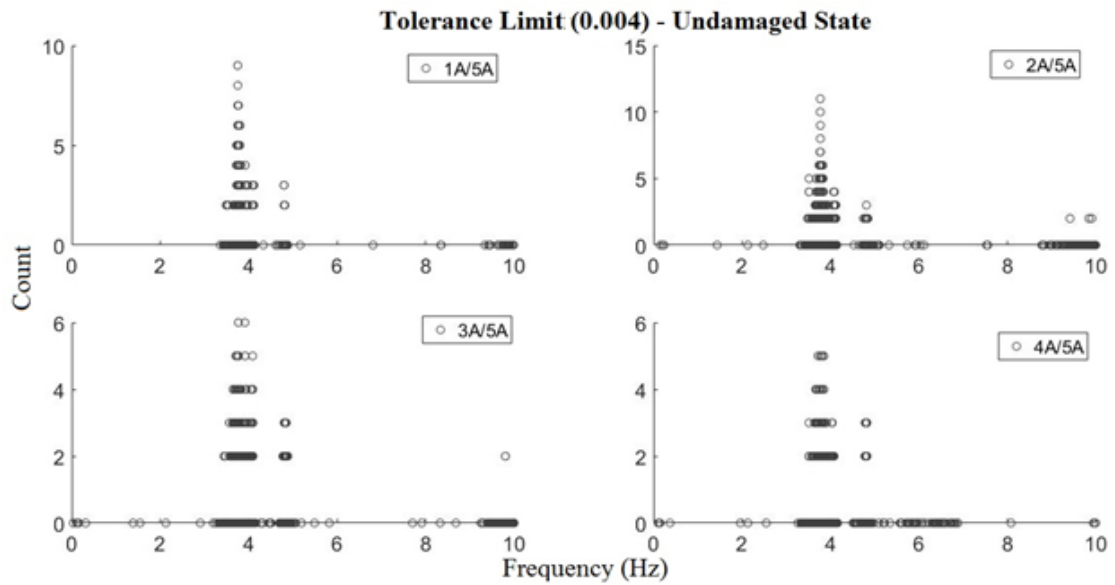


Figure 6.6. Count plot estimates for the eight data sets obtained from acceleration data measured during the Undamaged State using a tolerance limit of ± 0.004 .

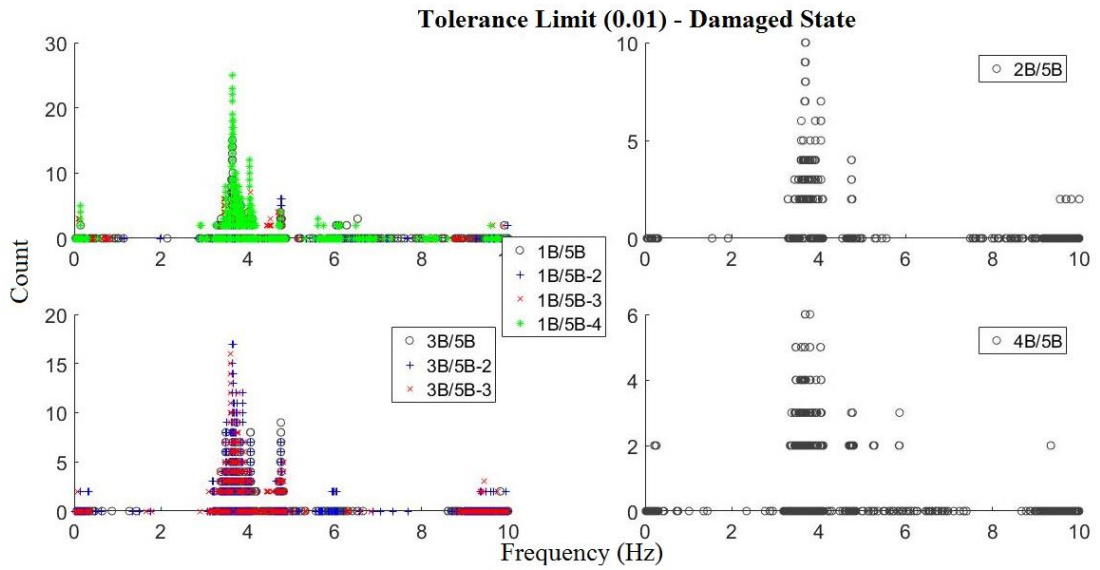


Figure 6.7. Count plot estimates for the eight data sets obtained from acceleration data measured during the Damaged State using a tolerance limit of ± 0.01 .

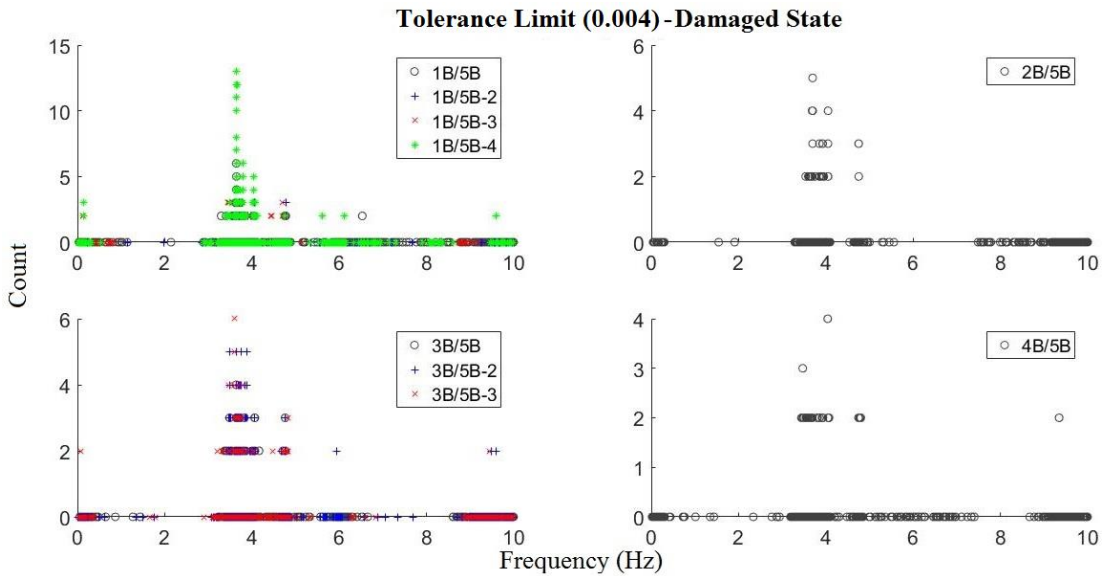


Figure 6.8. Count plot estimates for the eight data sets obtained from acceleration data measured during the Damaged State using a tolerance limit of ± 0.004 .

When the results are examined in detail, it is seen that the first two modes which are close to each other on the PSD graph can be detected more accurately for the tolerance limit 0.01. Damage-induced natural frequency changes appear to be 2%, 1% and 1% respectively for

the first three modes. For the first three modes, the frequency shifts are observed and tabulated in Tables 6.1-6.3.

Table 6.1. Estimated natural frequency for the first mode:

Stories	Undamaged	Damaged State	Difference (%)
1 and 5	3.754	3.649	2.80
2 and 5	3.77	3.695	1.99
3 and 5	3.771	3.654	3.10
4 and 5	3.743	3.687	1.50
Average	3.759	3.671	2.34

Table 6.2. Estimated natural frequency for the second mode:

Stories	Undamaged	Damaged State	Difference (%)
1 and 5	4.107	4.035	1.75
2 and 5	4.089	4.05	0.95
3 and 5	4.085	4.06	0.61
4 and 5	4.053	4.042	0.27
Average	4.084	4.047	0.91

Table 6.3. Estimated natural frequency for the third mode:

Stories	Undamaged	Damaged State	Difference (%)
1 and 5	4.8	4.77	0.63
2 and 5	4.847	4.752	1.96
3 and 5	4.81	4.76	1.04
4 and 5	4.813	4.765	1.00
Average	4.818	4.761	1.18

7. CONCLUSIONS

In this thesis, system identification and damage detection problems are considered. Original novel procedures are proposed and the performances of the proposed methods are discussed through numerical and experimental data sets.

One of the major aims of this thesis work has been to establish an indicator that can be used reliably to detect damage in beam-like structures, and this issue is addressed in Chapter 2. To this end, significant modifications and improvements are performed on a parameter initially introduced by Yuen (1985), such that the method is generalized to include both single and multiple modes, and the restriction to the fundamental mass-normalized mode is eliminated. However, as a drawback of this generalization, “saddle points” are introduced. The proposed method has been successfully used to locate the damage in a number of different damage scenarios, including those with multiple damage locations, through extensive numerical simulations.

Chapter 3 is focused on system identification, stabilization diagrams, modal plots and count plots. The modal plot procedure is introduced, its conversion to the count plot in order to estimate the natural frequency and mode shape amplitude is developed. The count plots indicate that the largest clustering is at the natural frequencies of the system such that these plots, which are constructed via direct application of time domain techniques, may pose an alternative to the PSD Estimation method conducted in the frequency domain. These issues and applications regarding the joint use of count plots with the previously developed damage indicator are further developed in Chapter 4 through extensive simulations. The issue of the saddle points is addressed in the context of sensor deployment strategies. In an experimental study, it is observed that the existence of damage can be directly inferred by the variations in the modal zones.

In Chapter 5, the applicability of the proposed damage detection approach to realistic civil engineering structures is addressed via the numerical model of a six story building. One hundred and nineteen damage scenarios, out of which ninety correspond to instances of

single damage locations, are considered. The efficiency of the damage indicator, using both single modes and multiple modes as proposed in Chapter 2, is demonstrated through these damage scenarios.

In Chapter 6, data from a five story real structure is investigated and the count plot is used to investigate the natural frequency changes between the undamaged state and a damage state of the structure. The instrumentation, data collection and data analysis stages, in all of which the present author actively participated, provide a complete real life case study which lends further support to the applicability of the proposed methods to real structures.

Immediate further work related to the proposals contained in this thesis would be expected to focus on further experimental validations and also structured investigations to identify the significance of the variations of modal zones for different damage types.

REFERENCES

- Abdeljaber, O., O. Avci, S. Kiranyaz, M. Gabbouj, D. J. Inman, "Real-time vibration-based structural damage detection using one-dimensional convolutional neural networks", *Journal of Sound and Vibration*, 388, 154-170, 2017.
- Abé, M., Y. Fujino. "Monitoring of long-span bridges in Japan", In *Proceedings of the Institution of Civil Engineers-Civil Engineering*, vol. 170, no. 3, pp. 135-144. Thomas Telford Ltd, 2017.
- Ahlborn, T. M., R. Shuchman, L. L. Sutter, C. N. Brooks, D. K. Harris, J. W. Burns, K. A. Endsley, D. C. Evans, K. Vaghefi and R. C. Oats, "The state-of-the-practice of modern structural health monitoring for bridges: a comprehensive review", *Michigan Tech*, June, 2010.
- Akaike, H., "A new look at the statistical model identification", *IEEE transactions on automatic control*, 19(6), 716-723, 1974.
- Aktan, A. E., D. N. Farhey, D. L. Brown, V. Dalal, A. J. Helmicki, V. J. Hunt and S. J. Shelley, "Condition assessment for bridge management", *Journal of Infrastructure Systems*, 2(3), 108-117, 1996.
- Aktan, A. Emin, Daniel N. Farhey, Arthur J. Helmicki, David L. Brown, Victor J. Hunt, Kuo-Liang Lee, and Alper Levi. "Structural identification for condition assessment: experimental arts." *Journal of Structural Engineering*, 123(12), 1674-1684, 1997.
- Alampalli, S., M. M. Ettouney, A. K. Agrawal. "Structural health monitoring for bridge maintenance." *Bridge Structures* 1(3), 345-354, 2005.
- Allemang, R. J., "The modal assurance criterion—twenty years of use and abuse", *Sound and vibration*, 37(8), 14-23, 2003.

- An, Y., B. F. Spencer and J. Ou, "A test method for damage diagnosis of suspension bridge suspender cables", *Computer-Aided Civil and Infrastructure Engineering*, 30(10), 771-784, 2015.
- Armstrong, D. M., A. Sibbald, C. A. Fairfield and M. C. Forde, "Modal analysis for masonry arch bridge spandrell wall separation identification", *NDT & E International*, 28(6), 377-386, 1995.
- Astroza R., H. Ebrahimian, J. P. Conte, J. I. Restrepo and T. C. Hutchinson, "Influence of the construction process and nonstructural components on the modal properties of a five-story building", *Earthquake Engineering & Structural Dynamics*, 45(7):1063-84, 2016.
- Ayres, J. W., F. Lalande, Z. Chaudhry and C. A. Rogers, "Qualitative impedance-based health monitoring of civil infrastructures", *Smart Materials and Structures*, 7(5), 599, 1998.
- Barthorpe, R. J. and K. Worden, "Sensor Placement Optimization", *Encyclopedia of Structural Health Monitoring*, West Sussex: John Wiley & Sons, Ltd., 2009.
- Basseville, M., A. Benveniste, M. Goursat, L. Hermans, L. Mevel and H. Van der Auweraer, "Output-only subspace-based structural identification: from theory to industrial testing practice", *Journal of Dynamic Systems, Measurement, and Control*, 123(4), 668-676, 2001.
- Çaktı, E., E. Şafak, "Structural Health Monitoring: Lessons Learned", In *Seismic Isolation, Structural Health Monitoring, and Performance Based Seismic Design in Earthquake Engineering*, 145-164. Springer, Cham, 2019.
- Cauberghe, B., P. Guillaume, P. Verboven, E. Parloo, S. Vanlanduit, "A combined experimental-operational modal analysis approach in the frequency domain", In *Proceedings of the 21st International Modal Analysis Conference (IMAC XXI)*, Kissimmee, Florida, USA, 2003.

- Cawley, P. and R. D. Adams, "The location of defects in structures from measurements of natural frequencies", *The Journal of Strain Analysis for Engineering Design*, 14(2), 49-57, 1979.
- Chan, T. H., L. Yu, H. Y. Tam, Y. Q. Ni, S. Y. Liu, W. H. Chung, L. K. Cheng, "Fiber Bragg grating sensors for structural health monitoring of Tsing Ma bridge: Background and experimental observation", *Engineering structures*, 28(5), 648-659, 2006.
- Chan, T.H. and D. P. Thambiratnam, "Structural health monitoring in Australia", *Nova Science Publishers*, Hauppauge NY, 2011.
- Chandrashekar, M., and R. Ganguli, "Structural damage detection using modal curvature and fuzzy logic", *Structural Health Monitoring*, 8(4), 267-282, 2009.
- Chen, G.-W., P. Omenzetter, S. Beskhyroun. "Operational modal analysis of an eleven-span concrete bridge subjected to weak ambient excitations", *Engineering Structures*, 151, 839-860, 2017.
- Compán, V., P. Pachón, M. Cámara, P. B. Lourenço, A. Sáez, "Structural safety assessment of geometrically complex masonry vaults by non-linear analysis. The Chapel of the Würzburg Residence (Germany)", *Engineering Structures* 140, 1-13, 2017.
- Creffield, J.W., Wood destroying insects: wood borers and termites. CSIRO Publishing, 1996.
- Cross, E. J., K. Y. Koo, J. M. W. Brownjohn and K. Worden, "Long-term monitoring and data analysis of the Tamar Bridge", *Mechanical Systems and Signal Processing*, 35(1), 16-34, 2013.
- Darbani, B. M. and A. Hammad, "Critical review of new directions in bridge management systems", *Computing in Civil Engineering*, 330-337, 2007

- De Roeck, G., B. Peeters and W. X. Ren, "Benchmark study on system identification through ambient vibration measurements", *Proceedings of IMAC-XVIII, the 18th International Modal Analysis Conference*, 1106-1112, 2000.
- Derriso, M. M., E. E. Olson, M. P. DeSimio, "Military Aircraft", In *Encyclopedia of Structural Health Monitoring*, Wiley, Blackwell, Hoboken, NJ, USA, 1, 2009.
- Doebbling, S. W., C. R. Farrar, M. B. Prime and D. W. Shevitz, "Damage identification and health monitoring of structural and mechanical systems from changes in their vibration characteristics: a literature review (No. LA-13070-MS)", *Los Alamos National Lab.*, NM (United States), 1996.
- Dong, C., P. Q. Zhang, W. Q. Feng, and T. C. Huang, "The sensitivity study of the modal parameters of a cracked beam", *Proceedings of the 12th International Modal Analysis*, 2251, 98, 1994.
- Fassois, S. D. and J. S. Sakellariou, "Statistical time series methods for SHM", In *Encyclopedia of structural health monitoring*, 2009.
- Feng, D., M. Q. Feng, "Experimental validation of cost-effective vision-based structural health monitoring", *Mechanical Systems and Signal Processing*, 88, 199-211, 2017.
- Fu, Z., and J. He. "Overview of modal analysis", J. He, Z. Fu, *Modal analysis*, Butterworth-Heinemann, Elsevier, 1-11, 2001.
- Fujino, Y. and D. Siringoringo, "Strategies for structural health monitoring of bridges: Japan's experience and practice", *American Environmentalism: Philosophy, History, and Public Policy*, 15, 2013.
- Gandomi, A.H., M. G. Sahab, A. Rahaei and M.S. Gorji, "Development in mode shape-based structural fault identification technique", *World Applied Sciences Journal*, 5(1), pp.29-38, 2008.

- Gladwell, G. M., *Inverse problems in vibration*, Second Edition, Kluwer Academic Publishers, London, 2004.
- Gozzer, G., "Interdisciplinarity: a concept still unclear", *Prospects* 12(3), 281-292, 1982.
- Grimmelsman, Kirk A., Qin Pan, and A. Emin Aktan. "Analysis of data quality for ambient vibration testing of the Henry Hudson Bridge." *Journal of Intelligent Material Systems and Structures*, 18(8), 765-775, 2007.
- Hearn, G. and B. R. Testa, "Modal Analysis for Damage Detection in Structures", *J. Structural Engrg.*, 117-10, 1991.
- Hester, J., S. Prabhu, S. Atamturktur, J. Sorber. "Remote and wireless long-term vibration monitoring of historic monuments." *Procedia engineering* 199, 3302-3307, 2017.
- Heylen W., S. Lammens and P. Sas, *Modal analysis theory and testing*, Department of Mechanical Engineering, Katholieke Universiteit Leuven, Leuven, Belgium, 1997.
- Jiménez-Roa, L. A., J. Marulanda-Casas and A. Cruz-Escobar, "Real-time structural monitoring of Building 350 at Del Valle University", *Structural Control and Health Monitoring*, 24(8), 1959, 2016.
- Juang, J. N. and R. S. Pappa, "An eigensystem realization algorithm for modal parameter identification and model reduction", *Journal of guidance, control, and dynamics*, 8(5), 620-627, 1985.
- Juang, J. N., *Applied System Identification*, New Jersey: Prentice Hall, 1994.
- Juang, J. N., M. Phan, L. G. Horta and R. W. Longman, "Identification of observer/Kalman filter Markov parameters-Theory and experiments", *Journal of Guidance, Control, and Dynamics*, 16(2), 320-329, 1993.
- Juul, M., O. Balling, R. Brincker, "Operational Modal Analysis on Wind Turbine Hub", In *Topics in Modal Analysis & Testing, Volume 9*, pp. 69-77. Springer, Cham, 2019.

- Karbhari, V.M. and Ansari, F., Structural health monitoring of civil infrastructure systems. Elsevier, 2009.
- Kim, C., D. Jung, N. Kim, S. Kwon and M. Feng, "Effect of vehicle weight on natural frequencies of bridges measured from traffic-induced vibration", *Earthquake Eng. & Eng. Vib.*, 2(1), 109–115, 2003.
- Kirschneck, M., D. J. Rixen, Henk Polinder, and Ron van Ostayen, "In-Situ Experimental Modal Analysis of a Direct-Drive Wind Turbine Generator", In *Experimental Techniques, Rotating Machinery, and Acoustics, Volume 8*, pp. 157-165. Springer, Cham, 2015.
- Lam, H. F., K. V. Yuen and J. L. Beck, "Structural health monitoring via measured Ritz vectors utilizing artificial neural networks", *Computer-Aided Civil and Infrastructure Engineering*, 21(4), 232-241, 2006.
- Langone, R., E. Reynders, S. Mehrkanoon, J. A. Suykens, "Automated structural health monitoring based on adaptive kernel spectral clustering." *Mechanical Systems and Signal Processing*, 90, 64-78, 2017.
- Li, H, J. Ou, X. Zhang, M. Pei, N. Li, "Research and practice of health monitoring for long-span bridges in the mainland of China", *Smart Structures and Systems* 15(3), 555-576, 2015.
- Lorenzo, G. W. Fernández, D. Mercerat, M. P. S. d'Avila, E. Bertrand, A. Deschamps, "Operational Modal Analysis of a high rise RC building and modelling", In *IOMAC'15-The 6th International Operational Modal Analysis Conference*. 2015.
- Luş, H., R. Betti and R. W. Longman, "Identification of linear structural systems using earthquake-induced vibration data", *Earthquake Engineering & Structural Dynamics*, 28(11), 1449-1467, 1999.

- Luş, H., R. Betti and R. W. Longman, "Obtaining refined first-order predictive models of linear structural systems", *Earthquake engineering & structural dynamics*, 31(7), 1413-1440, 2002.
- Magalhães, F., A. Cunha, E. Caetano, "Vibration based structural health monitoring of an arch bridge: from automated OMA to damage detection." *Mechanical Systems and Signal Processing*, 28, 212-228, 2012.
- Malekjafarian, A., P. J. McGetrick, and E. J. OBrien, "A review of indirect bridge monitoring using passing vehicles", *Shock and vibration*, 2015, 286139, 1-16 2015.
- McNeill, D. K., "Data management and signal processing for structural health monitoring of civil infrastructure systems", *Structural Health Monitoring of Civil Infrastructure Systems*, Great Abington: Woodhead Publishing Limited, 2009.
- Meehan, R. E., "*Technology and application of structural health monitoring in bridges*", M. Sc. Thesis, Massachusetts Institute of Technology, 2011
- Moaveni, B., and I. Behmanesh, "Effects of changing ambient temperature on finite element model updating of the Dowling Hall Footbridge", *Engineering Structures*, 43, 58-68, 2012.
- Nagayama, T., M. Abe, Y. Fujino and K. Ikeda, "Structural identification of a nonproportionally damped system and its application to a full-scale suspension bridge", *Journal of Structural Engineering (ASCE)*, 131(10), 1536-45, 2005.
- Nord, T. S., K. A. Kvåle, Ø. W. Petersen, M. Bjerås, E. M. Lourens, "Operational modal analysis on a lighthouse structure subjected to ice actions", *Procedia engineering*, 199, 1014-1019, 2017.
- Pandey, A. K., M. Biswas and M. M. Samman, "Damage detection from changes in curvature mode shapes", *Journal of sound and vibration*, 145(2), 321-332, 1991.

- Peeters, B. and G. De Roeck, “Stochastic system identification for operational modal analysis: a review”, *Journal of Dynamic Systems, Measurement, and Control*, 123(4), 659-667, 2001a.
- Peeters, B., and G. De Roeck, “One-year monitoring of the Z 24-Bridge: environmental effects versus damage events”, *Earthquake engineering & structural dynamics*, 30, 149–171, 2001b.
- Peeters, B., *System identification and damage detection in civil engineering*, PhD Thesis, Katholieke Universiteit Leuven, 2000.
- Pereira, João Tiago Martins Neves. "*Applicability of the statistical pattern recognition paradigm for structural health monitoring of bridges*", M. Sc. Thesis, Universidade Católica Portuguesa, 2012.
- Prendergast L. J., D. Hester, K. O. Gavin and J. J. Sullivan, “An investigation of the changes in the natural frequency of a pile affected by scour”, *Journal of Sound and Vibration*, 332(25), 6685e702, 2013.
- Prendergast, L. J., and K. Gavin, “A review of bridge scour monitoring techniques” *Journal of Rock Mechanics and Geotechnical Engineering*, 6(2), 138-149, 2014.
- Ren, W. X. and Z. H. Zong, “Output-only modal parameter identification of civil engineering structures”, *Structural Engineering and Mechanics*, 17(3-4), 429-444, 2004.
- Reynders, E., *System identification and modal Analysis in structural mechanics*, PhD Thesis, Katholieke Universiteit Leuven, 2009.
- Reynders, Edwin, Daan Degrauwe, G. D. Roeck, F. Magalhães, E. Caetano, "Combined experimental-operational modal testing of footbridges", *Journal of Engineering Mechanics* 136(6), 687-696, 2010.
- Rytter, A., *Vibrational based inspection of civil engineering structures*, Ph.D. Thesis, Aalborg University, 1993.

- Satake, N., K. I. Suda, T. Arakawa, A. Sasaki and Y. Tamura, "Damping evaluation using full-scale data of buildings in Japan", *Journal of structural engineering*, 129(4), 470-477, 2003.
- Schoukens, J., R. Pintelon and Y. Rolain, "Time domain identification, frequency domain identification. Equivalencies! Differences?", *American Control Conference, 2004. Proceedings of the 2004*, 1, 661-666, 2004.
- Schwarz, G., "Estimating the dimension of a model", *The annals of statistics*, 6(2), 461-464, 1978.
- Shepherd, R. and J. D. Frost, "*Failures in civil engineering: structural, foundation and geoenvironmental case studies*", ASCE, 1995.
- Siringoringo, D. and Y. Fujino, "System identification of suspension bridge from ambient vibration response", *Eng. Struct.*, 30 (2), 462-477, 2008.
- Soyoz, S., U. Dikmen, N. Apaydin, K. Kaynardag, E. Aytulun, O. Senkardesler, N. Catbas, H. Lus, E. Safak, and M. Erdik, "System identification of Bogazici suspension bridge during hanger replacement", *Procedia engineering*, 199, 1026-1031, 2017.
- Steinmann, F., K. I. Voigt, T. Schaeffler, U. Loewen, "Investigation of the diversity of engineering disciplines." In *Proceedings of PICMET'14 Conference: Portland International Center for Management of Engineering and Technology; Infrastructure and Service Integration*, 3131-3137, 2014.
- Sumitro, S., Y. Matsui, M. Kono, T. Okamoto and K. Fujii, "Long span bridge health monitoring system in Japan", *Health monitoring and management of civil infrastructure systems*, 4337, 517-525, 2001.
- Sumitro, S. and M. L. Wang, "*Structural Health Monitoring System Applications in Japan*", In *Sensing Issues in Civil Structural Health Monitoring*, Springer, Dordrecht, 2005.

- Taha, M. R. and J. Lucero, "Damage identification for structural health monitoring using fuzzy pattern recognition", *Engineering Structures*, 27(12), 1774-1783, 2005.
- Tcherniak, D., C. E. Carcangiu, and M. Rossetti. "Application of OMA to operational wind turbine: methods for cleaning up the Campbell diagram." In *Proc. Int. Conference on Noise and Vibration Engineering (ISMA)*. 2012.
- Teughels, A., J. Maeck and G. De Roeck, "Damage assessment by FE model updating using damage functions", *Computers and Structures*, 80, 1869–1879, 2002.
- Toksoy, T., and A. E. Aktan. "Bridge-condition assessment by modal flexibility." *Experimental Mechanics* 34(3), 271-278, 1994.
- Tufan, T., S. Akalp, "Modal plot—System identification and fault detection", *Structural Control and Health Monitoring*, e2347, 2019.
- Verboven, P., *Frequency-domain system identification for modal analysis*, Ph.D. Thesis, Vrije Universiteit Brussel, Brussels, 2002.
- Vicario, F., M. Q. Phan, R. Betti and R. W. Longman, "Output-only observer/Kalman filter identification (O3KID)", *Structural Control and Health Monitoring*, 22(5), 847-872, 2015.
- Wahab, M. M. A. and G. De Roeck, "Damage detection in bridges using modal curvatures: applications to a real damage scenario", *Journal of Sound and Vibration*, 226(2), 217–235, 1999.
- Wang, Jian-Yi, Jan Ming Ko, and Yi-Qing Ni. "Modal sensitivity analysis of Tsing Ma Bridge for structural damage detection." In *Nondestructive Evaluation of Highways, Utilities, and Pipelines IV*, 3995, 300-312, 2000.
- Wang, L. and T. H. Chan, "Review of vibration-based damage detection and condition assessment of bridge structures using structural health monitoring." *QUT Conference Proceedings*, 2009.

- Wong, K. Y., W. Y. K. Chan, K. L. Man, W. L. N. Mak and C. K. Lau, "Structural health monitoring results on Tsing Ma, Kap Shui Mun, and Ting Kau Bridges", *Nondestructive Evaluation of Highways, Utilities, and Pipelines IV*, 3995, 288-300, 2000.
- Yang, J. N., "Application of optimal control theory to civil engineering structures", *Journal of the engineering Mechanics Division*, 101(6), 819-838, 1975.
- Yazdanpanah, O. and S. M. Seyedpoor, "A new damage detection indicator for beams based on mode shape data", *Structural Engineering and Mechanics*, 53(4), pp.725-744, 2015.
- Yuen, M.M.F., "A Numerical Study of the Eigenparameters of a Damaged Cantilever", *Journal of Sound and Vibration*, 103, 301–310, 1985.
- Zhang, L., Y. Yao and M. Lu, "An improved time domain polyreference method for modal identification", *Mechanical Systems and Signal Processing*, 1(4), 399-413, 1987.
- Zhang, L., T. Wang and Y. Tamura, "A frequency–spatial domain decomposition (FSDD) method for operational modal analysis", *Mechanical systems and signal processing*, 24(5), 1227-1239, 2010.
- Zhang, Y., M. Kurata and J. P. Lynch, "Long-Term Modal Analysis of Wireless Structural Monitoring Data from a Suspension Bridge under Varying Environmental and Operational Conditions: System Design and Automated Modal Analysis", *Journal of Engineering Mechanics*, 143(4), 2016.
- Zhang, Z., and A. E. Aktan. "Application of modal flexibility and its derivatives in structural identification", *Journal of Research in Nondestructive Evaluation* 10(1), 43-61, 1998.